Norwegian University of Life Sciences
Faculty of Science and Technology

Philosophiae Doctor (PhD)
Thesis 2024:12

# Computational discovery and design of organic molecular ferroelectrics

## Beregningsbasert oppdagelse og design av organisk molekylære ferroelektriske materialer

Seyedmojtaba Seyedraoufi

# Computational discovery and design of organic molecular ferroelectrics

## Beregningsbasert oppdagelse og design av organisk molekylære ferroelektriske materialer

Philosophiae Doctor (PhD) Thesis

Seyedmojtaba Seyedraoufi

Norwegian University of Life Sciences
Faculty of Science and Technology

Ås , 2024

Thesis number 2024:12
ISSN 1894-6402
ISBN 978-82-575-2130-1

# Abstract

In the early stages, discovered ferroelectrics were unsuitable for industrial applications, but following the discovery of ceramic ferroelectrics, they gained widespread usage in capacitors, actuators, and piezoelectric transducers. Over time, these applications were extended to include thin-film capacitors and memories. However, inorganic ferroelectrics still contain rare or even heavy elements and require a high-temperature fabrication process. Organic molecular ferroelectrics (OPTFes) could provide solutions to both these challenges, and they furthermore exhibit other favorable properties such as low weight and low-cost fabrication. This thesis focuses on the computational discovery and design of novel organic molecular ferroelectrics.

"Discovery" part is devoted to computationally screening of molecules in the Cambridge Structural Database to identify new organic proton-transfer ferroelectrics and ferroelectric plastic crystals. The screening process was based on the structural characteristics of these materials, such as pseudo-inversion symmetry in OPTFes, and molecular geometries and hydrogen-bonding patterns suitable for molecular rotation in plastic crystals. The results revealed seven new OPTFe candidates, with five of them being tautomeric salts, and 54 candidates for plastic ferroelectrics. To model the crystals, density functional theory was employed, and for some identified crystals the calculations indicate high spontaneous polarization exceeding 20 $\mu C/cm^2$.

In the subsequent "design" phase, we took advantage of a group of acid-base OPTFe structures incorporating two distinct molecules, one acid and one base. This is useful for rational design, allowing the combination of different acid-base molecules and tracking trends and improvements in ferroelectric properties. One design goal, for example, was to increase the density of molecular dipoles and, consequently, spontaneous polarization by incorporating smaller molecules. Substituting the acid or the base molecules will, however, often alter the crystal packing, and we employed the crystal structure prediction (CSP) method to predict these packings. The CSP results, combined with density functional calculations, predicted that three out of 30 combinations exhibited ferroelectric packing with enhanced spontaneous polarizations compared to the reported acid-base OPTFes. Additionally, two anti-ferroelectric candidates were identified.

Findings from both the discovery and design parts provide insight that can be used for the systematic development of novel organic molecular ferroelectrics for a wide range of applications.

# Sammendrag

Da ferroelektriske materialer først ble oppdaget, var de lite egnet for industrielle anvendelser, men etter oppdagelsen av keramer med ferroelektriske egenskaper, ble de brukt blant annet i aktuatorer og piezoelektriske trandusere. Over tid har bruksområdet utvidet seg til å inkludere tynnfilmkondensatorer og dataminne. Dagens materialer inneholder imidlertid sjeldne og/eller giftige grunnstoffer, og produksjonen krever høy temperatur. Organiske molekylære ferroelektriske materialer (OPTFer) kan være et bærekraftig alternativ som løser begge disse utfordringene, og de har i tillegg andre gunstige egenskaper som lav vekt og lave produksjonskostnader. Denne avhandlingen fokuserer på oppdagelse og design av slike materialer ved hjelp av beregningsbaserte metoder.

"Oppdagelse"-delen av avhandlingen er viet til beregningsbasert screening av molekyler i Cambridge Structural Database for å identifisere nye OPTFer og ferroelektriske plastiske krystaller. For førstnevnte krevde screeningen pseudo-inversjonssymmetri, mens det for de plastiske krystallene ble satt krav til molekylenes geometri og at hydrogenbindings-mønstrene kunne tillate molekylær rotasjon. Totalt sett avdekket screeningen syv nye OPTFer-kandidater, hvorav fem var tautomere salter, og 54 kandidater for plastiske ferroelektriske materialer. Alle materialene ble modellert med tetthetsfunksjonalteori, og for noen av dem viser beregningene spontan polarisering større enn 20 $\mu$C/cm$^2$.

I den påfølgende "design"-delen utnyttet vi en gruppe OPTFer som inneholder to ulike molekyler, én syre og én base. Begge disse komponentene kan varieres, og en fremgangsmåte der utvalgt kombinasjoner testes ut på en systematisk måte kan brukes til både å designe nye materialer med forbedrede egenskaper og til å utforske trender og forbedringer for ønskede egenskaper. Et erklært design-mål var å øke tettheten av molekylære dipoler og dermed øke den spontane polariseringen ved å bruke små molekyler. Når størrelsen på en komponent i en krystallstruktur modifiseres, vil imidlertid ofte også pakkingen av molekyler endres. Derfor ble krystallstruktur-prediksjon (CSP) metoder benyttet for å forutsi pakkingen til de nye systemer. Resultatene fra CSP ble kombinert med beregninger basert på tetthetsfunksjonsteori og predikerte tre syre-base kombinasjoner med ferroelektrisk pakning og forbedret spontan polarisering sammenlignet med rapporterte syre-base-OPTFer. Det ble også funnet to strukturer som kan gi anti-ferroelektriske egenskaper.

Resultatene fra både "oppdagelse"- og "design"-delen gir innsikt som kan brukes til systematisk utvikling av nye organiske molekylære ferroelektriske materialer for et vidt felt av applikasjoner.

# Acknowledgements

I want to thank my main supervisor, Kristian Berland, for all the guidance. I learned a lot from him during the past three years. Given his interest in long-range effects, I believe he will continue to inspire me even after my time here at NMBU.

I would like to thank my co-supervisor, Carl Henrik Görbitz, for his valuable insights and guidance throughout these three years.

I also take this opportunity to thank Ola Nilsen and Manjunath Balagopalan for their feedback during our collaboration on the FOX project.

During my Ph.D., I had the privilege of working with amazing group members (Elin, Prutha, Rasmus, Øven, and Dario) who made this journey more delightful. I express my gratitude to all of them. A special thank to Elin Dypvik Sødahl for her feedback and patience during our collaboration on the FOX project.

Finally, I want to thank my mother, Parvin, and my siblings, Mitra and Saeid, for their unwavering support during these three years.

# List of Papers

## Paper I

S. Seyedraoufi and K. Berland. "Improved proton-transfer barriers with van der Waals density functionals: Role of repulsive non-local correlation". In: *The Journal of Chemical Physics*. Vol. 156, issue. 24 (2022), pp. 106–110. DOI: https://doi.org/10.1063/5.0095128.

## Paper II

S. Seyedraoufi, E. D. Sødahl, C. H. Görbitz and K. Berland. "Database mining and first-principles assessment of organic proton-transfer ferroelectrics". *Submitted for publication.*

## Paper III

E. D. Sødahl, S. Seyedraoufi, C. H. Görbitz and K. Berland. "Ferroelectric crystals of globular molecules: Cambridge Structural Database mining and computational assessment". In: *Crystal Growth & Design*. (2023), DOI: https://doi.org/10.1021/acs.cgd.3c00713.

## Paper IV

S. Seyedraoufi, G. M. Day, and K. Berland. "Engineering new organic proton-transfer acid-base (anti-)ferroelectric salts using crystal structure prediction". *Manuscript.*

# Additional Scientific Work

## Oral presentaions

E. D. Sødahl, S. Seyedraoufi, C. H. Görbitz and K. Berland. "Molecular ferroelectric crystals: discovering new sustainable ferroelectrics". Invited talk at: *The Structure Physics section at the University of Oslo*, Oslo, Norway, 2022.

S. Seyedraoufi, E. D. Sødahl, C. H. Görbitz and K. Berland. "Database mining and first-principles assessment of organic proton-transfer ferroelectrics". Presented at: *The University of Southampton, Computational Systems Chemistry*, Southampton, UK, 2023.

E. D. Sødahl, J. Walker, S. Seyedraoufi and K. Berland. "Ferroelectric Molecular Crystals – Discovering and Modeling of Unknown Properties in Known Materials". Invited talk at: *the 10th NKS-FUM meeting*, Trondheim, Norway, 2023.

S. Seyedraoufi, E. D. Sødahl, C. H. Görbitz and K. Berland. "Database mining and first-principles assessment of organic proton-transfer ferroelectrics". Invited talk: *User Webinar: The Cambridge Structural Database in Electronics Research*, 2024.

## Poster presentaions

S. Seyedraoufi, E.D. Sødahl, C.H. Görbitz and K. Berland. "Database mining and first-principles assessment of organic proton-transfer ferroelectrics". Presented at: *The 33rd edition of the European Crystallography Conference (ECM33)*, Versailles, France, 2022.

S. Seyedraoufi, G.M. Day and K. Berland. "Engineering new organic proton-transfer acid-base (anti-)ferroelectric salts using crystal structure prediction". Presented at: *European Conference on Computational & Theoretical Chemistry (EuChemS CompChem 2023)*, Thessaloniki, Greece, 2023.

# Contents

# Chapter 1

# Introduction

## 1.1 Motivation and background

The distinctive property of ferroelectric materials is their spontaneous polarization ($\boldsymbol{P}_\mathrm{s}$), which is a measurable vector quantity pointing in the direction of the separation of charges in a crystal. In the context of molecular crystals, a non-zero $\boldsymbol{P}_\mathrm{s}$ occurs whenever molecules with a permanent dipole are packed so that their dipole moments do not cancel out. Having a measurable $\boldsymbol{P}_\mathrm{s}$ is, however, not sufficient to make a crystal "ferroelectric"; it must also be possible to switch the polarization in the opposite direction in response to an external electric field. Ferroelectrics are a subclass of pyroelectric and piezoelectric materials, indicating that their polarization changes as a function of temperature and mechanical stress, respectively[1].

The properties of the first ferroelectric, Rochelle salt [2], were unsuitable for industrial applications as its crystals are brittle and dissolve in water. The same applies to similar materials discovered in the following years. It was not until the discovery of barium titanate ($BaTiO_3$)[3] that ferroelectrics gained properties suitable for industrial applications, such as capacitors and transducers[4]. $BaTiO_3$ capacitors are still being produced on a large scale.

Thin-film ferroelectrics were introduced in 1984, marking the onset of a period with a focus on developing thin layers of single crystals tailored for applications in small-scale electronics, including capacitors and memories[4, 5]. In 1994, six million ferroelectric microchip capacitors were used daily in the mobile industry in Japan[4].

The discovery of thiourea[6] in 1956 introduced a promising class of ferroelectrics called organic molecular ferroelectrics. These materials exhibit properties that hold the potential to overcome the limitations associated with inorganic materials. These advantages include suitability for lightweight applications, the capacity to tune properties through structural manipulations, cost-effective fabrication, and adaptability for integration into flexible substrates[7, 8]. Furthermore, they are typically free of heavy and/or rare elements[7, 8].

Organic Proton-Transfer Ferroelectric (OPTFe) materials and ferroelectric plastic crystals represent examples of organic molecular ferroelectrics. OPTFe systems include hydrogen-bonded single-component molecular substances as well as acid-base salts. Ferroelectric plastic crystals typically consist of tetrahedral anions combined with nitrogen- and/or oxygen-containing cations with an almost globular shape. The number of identified systems in each category, around 20 materials, is very small compared to approximately 370,000 structures of organic molecules deposited in the Cambridge Structure Database (CSD). From this, we inferred that the database likely includes structures of ferroelectrics that were

not initially recognized as such by the original authors. This was the motivation for paper II and paper III, where we screened the CSD for potential OPTFe and ferroelectric plastic crystals, respectively. To model materials and calculate properties, such as proton-transfer barriers in OPTFes and lattice parameters, we employed density functional theory (DFT), based on our benchmarking studies presented in paper I and paper II.

In acid-base OPTFes, the presence of two molecular types in the structure provides an opportunity to explore the correlation between various molecular combinations and ferroelectric properties. In solid-state chemistry, the correlation between crystal structure, such as packing and inter-molecular connection patterns (synthons), and properties like mechanical properties (elasticity, plasticity, bending, and brittleness)[9, 10], as well as melting point[11], have been studied. This is also a common procedure in industries dealing with organic molecules, for example, the pharmaceutical industry, to tune the desired properties of the compounds[12]. This was the motivation for paper IV, in which we replaced acid and base molecules in acid-base OPTFe salts with different small one-ring acid and base molecules. As the substitution of molecules has the potential to modify the hydrogen-bond network and crystal packing, we employed the crystal structure prediction method to predict the packing in various molecular combinations.

## 1.2 Outline

In Chapter 2, we introduce organic molecular crystals and CSD. A concise explanation of the methodology used for calculating $\boldsymbol{P}_{\mathrm{s}}$ is provided, and the chapter concludes by introducing a procedure to mine CSD. Chapter 3 describes van der Waals density functional theory, which was central in most of our density functional theory calculations. Finally, Chapter 4 outlines the crystal structure prediction method.

# Chapter 2

# Organic molecular ferroelectrics

This chapter provides the theory and concepts of ferroelectricity, along with the method used to calculate $\boldsymbol{P}_{\mathrm{s}}$ in ferroelectrics. In Sec.2.2, a brief description of CSD is provided, and subsequently, in Sec.2.3 and Sec. 2.4, OPTFes and ferroelectric plastic crystals are introduced.

## 2.1 Ferroelectricity

A distinctive characteristic of ferroelectrics is the presence of $\boldsymbol{P}_{\mathrm{s}}$ over a defined temperature range, even in the absence of an external electric field. The definition of $\boldsymbol{P}_{\mathrm{s}}$ and how it will be calculated in a molecular crystal will be explained later. However, for simplicity, we can gain intuition from $\boldsymbol{P}_{\mathrm{s}}$ as a vector in the direction of permanent charge separation in the material. In the case of molecular crystals, it is the sum of all molecular permanent dipole moments in the unit cell.

Fig. 2.1 illustrates the polarization-electric field (PE) plots for ferroelectric, anti-ferroelectric, and paraelectric materials. In ferroelectric materials (a), the PE curve displays a hysteresis loop, indicating that the system's state depends on its previous history or state [13]. This characteristic forms the foundation for ferroelectrics applications in memory devices, such as in Ferroelectric Random-Access Memory[14]. The loop has a non-zero polarization value at zero electric field, known as the remnant polarization. In this state, crystal domains may form with varying polarization strength and direction, separated by domain walls. As the electric field increases, the polarization reaches its maximum value, referred to as the saturation polarization. In this state, the domain walls have moved to expand the domains with polarization aligned to the electric field. Unlike uniaxial ferroelectrics, where domains can only be aligned in one direction, certain ferroelectric materials exhibit multiaxial ferroelectricity, allowing dipoles to be aligned in several directions.

The ferroelectrics have two energetically equivalent states with opposite $\boldsymbol{P}_{\mathrm{s}}$ directions, referred to as bistability. The minimum electric field required to switch the sign of $\boldsymbol{P}_{\mathrm{s}}$ is called the coercive field ($E_{\mathrm{c}}$), as depicted in Fig.2.1. $E_{\mathrm{c}}$ is an important property of ferroelectric materials that can define the field of applications. For instance, in small-scale electronics requiring the integration of a thin layer (approximately 100 nm in thickness) of ferroelectric material, an $E_{\mathrm{c}}$ of around 100 kV/cm is needed to achieve a switching voltage of about 2 V[15].

Anti-ferroelectric materials exhibit $\boldsymbol{P}_{\mathrm{s}} = 0$ at zero electric field, with domains formed in an antiparallel orientation that cancels out the net polarization; however, they display a hysteresis loop when an electric field is applied, as depicted in panel (b). On the other hand, paraelectric materials have zero $\boldsymbol{P}_{\mathrm{s}}$ and do not exhibit any PE hysteresis features, as shown in panel (c).

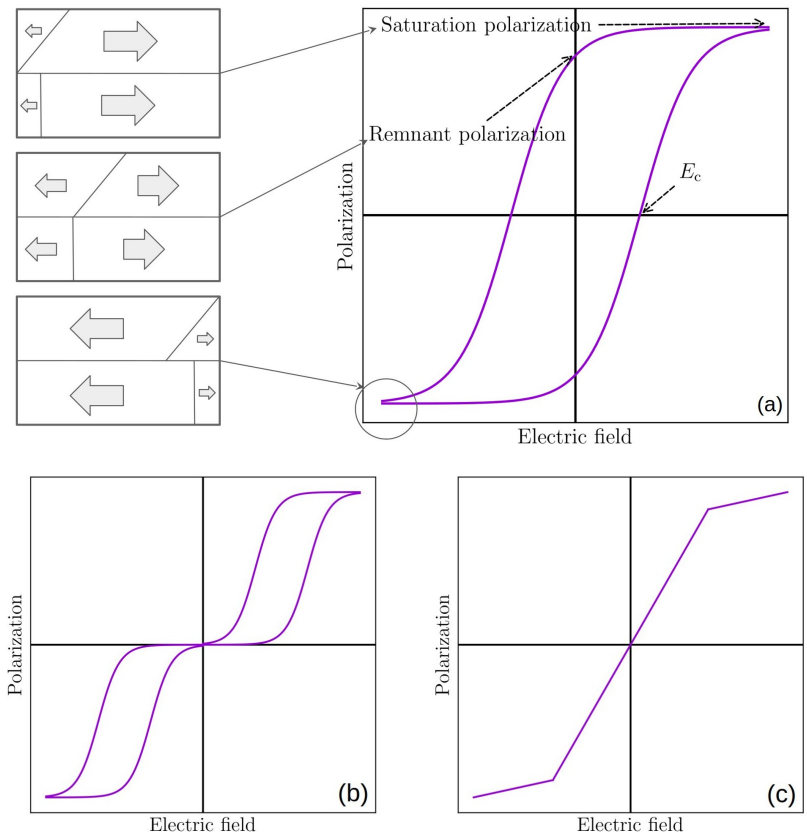


Figure 2.1: The polarization as a function of the electric field is plotted for (a) ferroelectric (b) anti-ferroelectric and (c) paraelectric materials. In the upper panel, the remnant polarization, saturation polarization, and coercive field ($E_c$) are marked on the plot, and the corresponding uniaxial ferroelectric domains are schematically depicted. Grey thick arrows represent the net polarization inside the domains.

In contrast to dielectric materials, which lack permanent dipoles but can be polarized under an electric field, paraelectrics have permanent dipoles that cancel each other out at zero electric field but can be aligned when an electric field is applied.

Beyond a critical temperature known as the Curie point ($T_C$), ferroelectric materials lose their $\boldsymbol{P}_s$[16]. Moving beyond $T_C$ is marked by a transition from a lower-symmetry ferroelectric phase to a higher-symmetry paraelectric phase.

The ferroelectric phase adopts one of the 68 polar space groups, characterized by the loss of symmetry elements present in the paraelectric phase, including the center of inversion[17]. However, the transition from the paraelectric to the

ferroelectric phase can result from minor structural changes, where the center of inversion is not completely lost and remains as a pseudo-center of inversion. One such example is OPTFe materials [18], where the breaking of the inversion symmetry is mainly attributed to the protons. This means that if we remove the protons, we can to a large extent restore the symmetry. This distinctive feature has been used in this thesis to screen OPTFes materials and is further explained in Sec. 2.2.

Ferroelectricity in molecular crystals can arise through different mechanisms. Ferroelectric materials are typically categorized into two groups based on their switching behavior. One category, termed "order-disorder," involves the reorientation of static dipoles. Alternatively, "displacive" category is characterized by the displacement of atomic species[19]. For instance, in molecular plastic crystals, the change in polarization direction occurs through the rotational reorientation of molecular species[20].

## 2.2 Cambridge Structural Database

CSD is a repository for crystal structures of organic and metal-organic compounds[21]. This database was established in 1965 and has since hosted structural information on more than 1.25 million compounds obtained from X-ray and neutron diffraction analyses. Additionally, the database serves as a source for validation and curation of structural data and, for a fraction of entries, provides measured experimental properties of crystals.

CSD has assigned an identifier, known as the CSD refcode, to each of the entries. This identifier makes the structure accessible through other software that has an interface with CSD, such as MERCURY[22] and ConQuest[23]. The refcodes can also be used to access the entries through the Python Application Programming Interface (API). CSD uses the Crystallographic Information File (CIF) format to store the structural data, and all CIF files are freely accessible through the CSD Access Structure service.

## 2.3 Organic Proton-Transfer Ferroelectrics

In OPTFes, the dominant switching mechanism of $\boldsymbol{P}_\mathrm{s}$ depends on inter- and/or intra-molecular proton transfer (PT) through a connected PT path, which may be combined with the displacement of molecules. OPTFes can be mainly divided into two categories: single-component compounds where proton movements are associated with the rearrangement of $\pi$ orbitals—a phenomenon known as proton tautomerism—and acid-base salts.

Panel (c) of Fig. 2.2 illustrates the switching mechanism of 5,6-dichloro-2-methyl-1H-benzimidazole (CSD refcode: REZBOP), a tautomeric OPTFe. In paper II, we demonstrated that PT in these compounds likely exhibits a collective nature, implying that more than one proton transfer simultaneously to adjacent molecules.

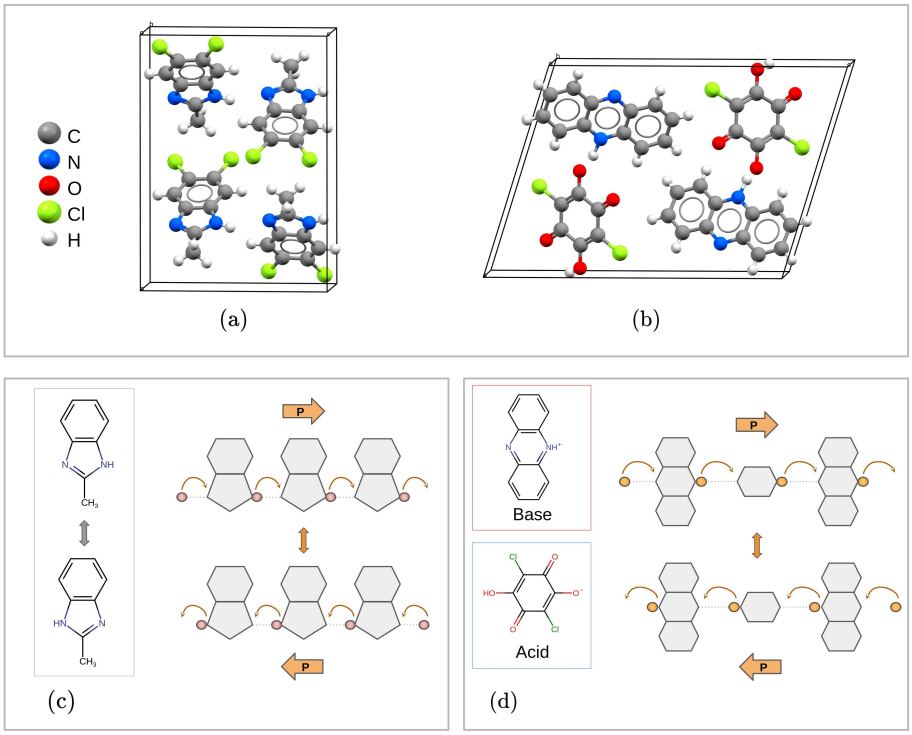


Figure 2.2: The crystal structures of (a) 5,6-dichloro-2-methyl-1H-benzimidazole (REZBOP), a tautomeric OPTFe, and (b) phenazinium chloranilate (MAMPUM03), an acid-base OPTFe are shown. The corresponding switching mechanisms are schematically depicted in (c) and (d) respectively. The curved arrows indicate the connected PT path.

The second category is acid-base salts [1, 24–26], where the inversion of $\boldsymbol{P}_\mathrm{s}$ is achieved by transferring protons between molecules containing acidic and basic functional groups. This process is illustrated in the panel (d). The example system is phenazinium chloranilate (CSD refcode: MAMPUM03), an acid-base OPTFe. Our findings, detailed in paper II, support a single PT mechanism for these compounds. In contrast to tautomeric compounds, one key distinction is that these compounds are salts with two different molecules in the unit cell. This indicates that different acid and base molecules can be combined to design new OPTFe materials.

Apart from these two groups, amphoteric compounds containing both acidic and basic functional groups on one molecule can also exhibit ferroelectricity. In anthranilic acid, an OPTFe material, a one-dimensional hydrogen-bonded network between zwitterionic and neutral anthranilic acid molecules enables ferroelectric switching through PT.[27].

As evident from Fig. 2.3, the $\boldsymbol{P}_\mathrm{s}$ values for most OPTFe systems are

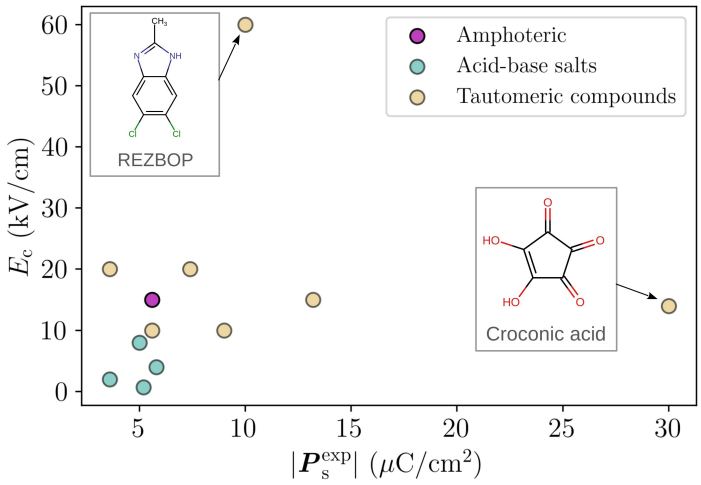


Figure 2.3: The experimental $|\boldsymbol{P}_s|$ versus $E_c$ for reported OPTFes. The structures with the largest $|\boldsymbol{P}_s|$ and $E_c$ are marked on the plot.

below 10 $\mu$C/cm$^2$. The exceptions are cyclobut-1-ene-1,2-dicarboxylic acid (CBUDCX04) with a value of around 13 $\mu$C/cm$^2$ and croconic acid (GUMMUW11) with a value of around 30 $\mu$C/cm$^2$. Additionally, the $E_c$ values are mostly below 20 kV/cm, which is one of the reasons OPTFes have not found applications in the small-scale electronics industry. The highest reported $E_c$ belongs to REZBOP with a value of 60 kV/cm.

One promising feature of OPTFes, particularly the tautomeric ones, is their $T_C$, which is typically in the range of 350–500 K. This characteristic is crucial for applications operating at room temperature but limits their usage in high-temperature fields, such as high-energy capacitors in the electric vehicle industry[28, 29].

## 2.4 Ferroelectric plastic crystals

Ferroelectric plastic crystals are another interesting class of organic molecular ferroelectrics. The plastic phase is a mesophase in which the material maintains its crystalline structure while exhibiting a higher degree of orientational disorder among rotatable molecular dipoles, which can be favorably aligned by applying an electric field, multiaxial ferroelectricity[30].

The mesophase can occur simultaneously with the ferroelectric-paraelectric phase transition or precede. Generally, the existence of the mesophase tends to elevate the material's melting point and enhance its mechanical deformability. The high melting point is related to the large entropy gain during the transition to the mesophase[31]. Overall, the deformability and multiaxial properties of plastic crystals render them attractive for a wide range of applications[32].

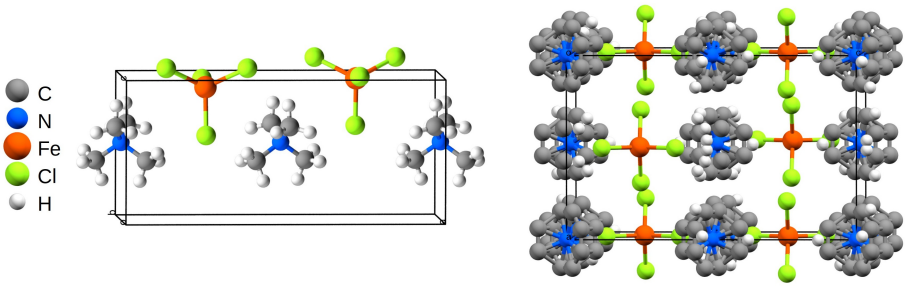


(a) Ferroelectric phase (b) Paraelectric phase

Figure 2.4: Tetramethylammonium tetrachloro-iron(III), a ferroelectric plastic crystal, is depicted in its (a) ferroelectric ordered phase, and (b) the paraelectric phase where the molecules are free to rotate.

Similar to acid-base OPTFes, having more than one molecular type in the unit cell provides an opportunity to design new materials with tuned properties.

Fig. 2.4 illustrates the ferroelectric and paraelectric phases of tetramethylammonium tetrachloro-iron(III), a known molecular plastic ferroelectric crystal[33]. In Panel (b), the plastic paraelectric phase is depicted, wherein crystals typically exhibit a higher symmetry, and molecules are free to rotate.

## 2.5 Calculating the spontaneous polarization

The theoretical definition of $\boldsymbol{P}_{\mathrm{s}}$ in a periodic solid and its subsequent implementation in electronic-structure programs are important for modeling ferroelectric materials. As the first attempt, $\boldsymbol{P}_{\mathrm{s}}$ can be defined as the electric dipole moment per unit cell volume,

$$\boldsymbol{P}_{\mathrm{cell}} = \frac{1}{V_{\mathrm{cell}}} \int_{\mathrm{cell}} d\mathbf{r}\mathbf{r}\rho(\mathbf{r}), \tag{2.1}$$

where the integral is over all positions in the unit cell, $V_{\mathrm{cell}}$ is the volume of the unit cell, and $\rho(\mathbf{r})$ is the charge density.

The problem with this definition is due to its dependence on the specification of the unit cell [34]. For example, consider a one-dimensional centrosymmetric unit cell with a cell vector of "$a$," containing positive and negative point charges as depicted in Fig. 2.5. For a collection of point charges the electric dipole moment per unit cell volume can be defined as

$$\boldsymbol{P}_{\mathrm{cell}} = \frac{1}{V_{\mathrm{cell}}} \sum_i q_i \mathbf{r}_i. \tag{2.2}$$

For this system, $\boldsymbol{P}_{\mathrm{cell}} = 1/a(-1 \times a/4 + 1 \times 3a/4) = 1/2\ |e|$. Now, by defining a new unit cell with a shift of half the cell vector (unit cell with the red dashed

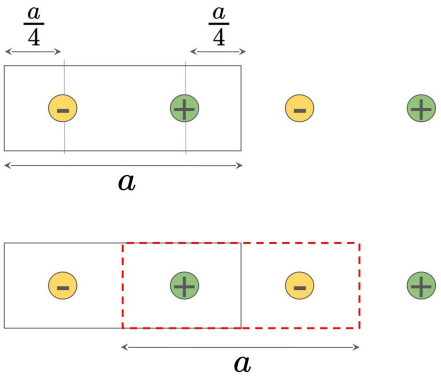


Figure 2.5: The upper schematic depicts a one-dimensional periodic chain of positive and negative point charges. The lower illustrates the displacement of the unit cell (red dashed box) in the same system, where $a$ represents the length of the unit cell.

line in the lower panel), $\boldsymbol{P}_{\text{cell}} = -1/2\ |e|$. We obtain two distinct non-zero values for our non-polar system. This becomes more complicated if we translate one of the point charges by a translation vector $\boldsymbol{T} = \sum_i m_i \boldsymbol{R}_i$ ($m_i$ is an integer and $\boldsymbol{R}_i$ is a cell vector). In this situation, Eq. 2.2 yields different values depending on the selected $\boldsymbol{T}$. Although point charges will be placed outside the unit cell, the underlying physics of the system remains unchanged due to the periodic boundary condition [34, 35]. For instance, in Fig. 2.5, translating the positive charge by a unit cell vector ($\boldsymbol{T} = a$) can increase the system's dipole moment to $3/2\ |e|$. If we keep translating point charges, we will get equidistant values that are centered around zero, referred to as the "quantum of polarization" and are defined as $e\boldsymbol{R}/\Omega$. Here $\boldsymbol{R} = \sum_i (m_i + 0.5)\boldsymbol{R}_i$ where $m_i$ is an integer, and $\Omega$ is the unit cell volume. For our one-dimensional system, the values are $\sum_i (m_i + 0.5)a/a = \cdots - 3/2, -1/2, 0, 1/2, 3/2, \ldots$ in $|e|$ unit.

According to the Berry-phase (modern) theory of polarization [36–38], the polarization of a periodic solid in its ground state is a multivalued quantity modulo $e\boldsymbol{R}/\Omega$, denoted here as $\boldsymbol{P}^m$. However, the difference between $\boldsymbol{P}^m$ of a given polar phase and its hypothetical paraelectric phase is constant if we find polarization quanta that smoothly connect the ferroelectric to paraelectric phase by gradually distorting the crystal structure.[34, 35]. This can be expressed as

$$\Delta \boldsymbol{P}^m = \int_0^1 d\lambda \frac{d\boldsymbol{P}^m}{d\lambda}. \tag{2.3}$$

$\Delta \boldsymbol{P}^m$ is equal to $\boldsymbol{P}_{\text{s}}$ and is defined as

$$\Delta \boldsymbol{P}^m = \boldsymbol{P}^m_{\lambda=1} - \boldsymbol{P}^m_{\lambda=0} + \frac{e\boldsymbol{R}}{\Omega}, \tag{2.4}$$

where $\boldsymbol{P}^m_{\lambda=1}$ is the polarization of the polar phase crystal, $\boldsymbol{P}^m_{\lambda=0}$ is the corresponding paraelectric centrosymmetric phase. $e\boldsymbol{R}/\Omega$ is the polarization quanta added to ensure the smoothness of the transition.

In a practical context, it is valuable to provide an overview of the methodology for calculating the $\boldsymbol{P}_\mathrm{s}$ of OPTFe crystals.

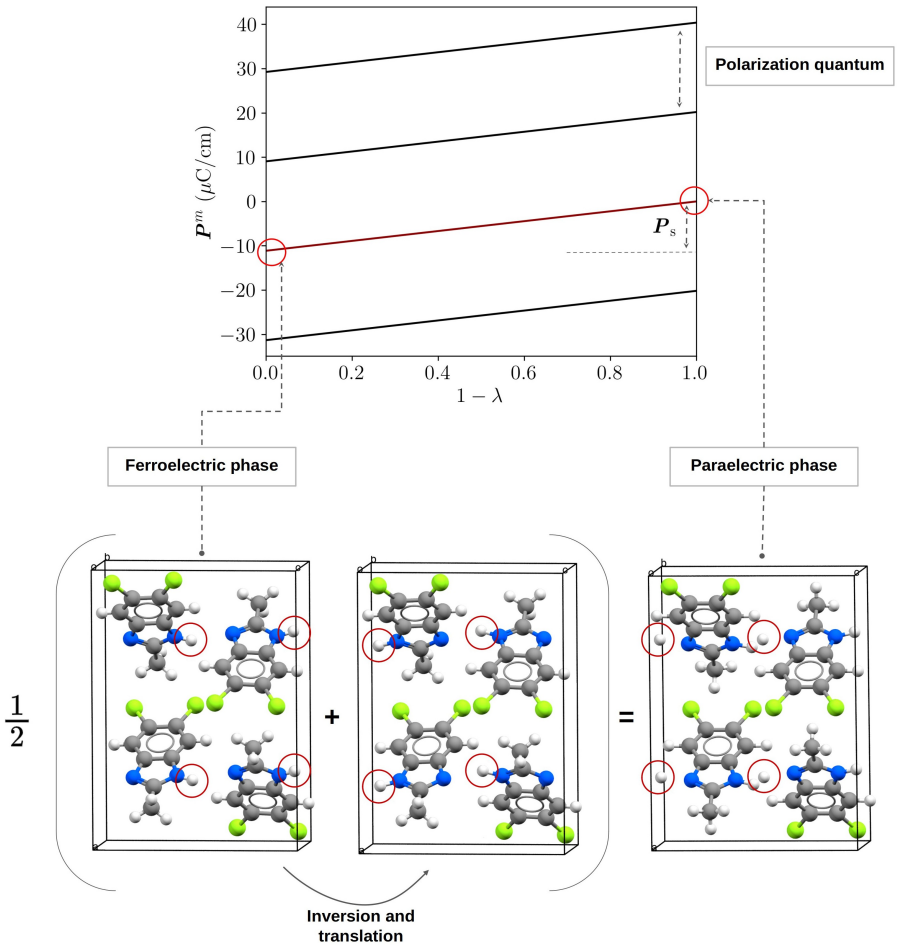


Figure 2.6: The schematic illustrates the calculation of $\boldsymbol{P}_\mathrm{s}$ for 5,6-dichloro-2-methyl-1H-benzimidazole (REZBOP) using the Berry-phase method. In the upper panel, $\boldsymbol{P}^m$ values for different interpolated images are selected in a manner to facilitate a smooth transition from the ferroelectric to the centrosymmetric phase. The parameter $\lambda$ represents the degree of interpolation. The lower panel illustrates the procedure for generating the paraelectric phase using the pseudo-center of symmetry.

In the case of OPTFe systems, the primary factor responsible for breaking the symmetry of the centrosymmetric phase is the displacement of protons, with minimal distortion of the other components of the molecular structures. This implies that OPTFes possess a detectable pseudo-center of inversion, and inverting the crystal through this center will result in a structure where the most significant observable change is the inter- and/or intra-molecular transfer of protons. In Fig. 2.6, this is illustrated using REZBOP as an example. Applying an inversion operation and subsequently aligning the crystal structures by minimizing interatomic distances, an inverted phase in which protons are transferred to adjacent molecules is achieved with a switched polarization direction. The hypothetical centrosymmetric phase is now defined by carefully averaging atomic positions pairwise while taking into consideration periodic boundary condition.

For our example system, we have defined a grid of 10 values for $\lambda$ (Eq. 2.3), which represents the degree of interpolation between the ferroelectric and paraelectric structures. The upper panel of Fig. 2.6 displays the branches connecting the ferroelectric polar phases to the paraelectric phases, separated by the polarization quanta. The difference between $\boldsymbol{P}^m_{\lambda=1}$ and $\boldsymbol{P}^m_{\lambda=10}$ is equal to $\boldsymbol{P}_\mathrm{s}$ with a size of around 11 $\mu$C/cm.

## 2.6 Mining the Cambridge Structural Database

Mining CSD involves defining both general and specific structural criteria to reduce the vast size of the database to a manageable set of structures. These structures can then be further evaluated using methods with higher computational costs, such as density functional theory. The application of general criteria, such as ensuring that entries contain atomic coordinates and lack disorder or polymeric structures prepares the database for more specialized analysis. Special criteria can be derived from the structural characteristics of reported organic ferroelectric materials.

As an example, Fig. 2.7 shows how different steps in screening OPTFe candidates reduce the number of structures (detailed in paper II). The first filter ensures that structures have polar space groups and excludes almost 88 % of the CSD entries. The other filter asks for organic structures that are not polymeric, have no disorder, and ensures that structures are deposited with readable atomic coordinates. This step excludes almost half of the structures. The last filter looks for a pseudo-center of inversion, as described in Sec. 2.5. This filter is quite strict, allowing only 3 % of structures to survive. Furthermore, only 1 % of these structures exhibit properties of OPTFe materials, such as connected hydrogen-bonded paths facilitating PT.

Another example is mining CSD for potential ferroelectric plastic crystals, as detailed in paper III. Special criteria are defined based on the structure of molecular plastic crystals, including roughly globular molecules with a limited number of hydrogen bonds capable of rotating, which is the polarization-switching mechanism in these materials. The molecules should also contain electronegative

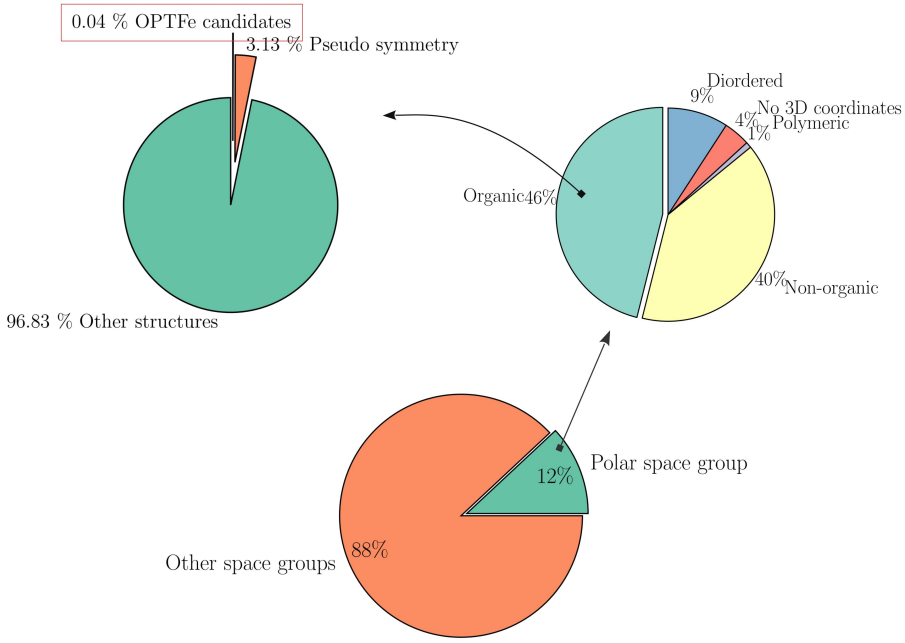


Figure 2.7: The distribution of CSD structures based on criteria defined for screening OPTFe materials.

atoms in their chemical formula to generate molecular dipole moments. Applying these criteria has reduced the pool of polar structures with around 86,000 entries to 75 potential ferroelectric plastic crystals.

Chapter 3

# Van der Waals density functional theory

Van der Waals (vdW) interactions emerge from the coupling of instantaneous dipoles results from electron density fluctuations within atoms and molecules. Although weaker compared to covalent or ionic bonds, vdW interactions are essential for understanding and predicting the behavior and properties of various materials and systems, such as the binding energy of layered systems or the energy and structures of molecular crystals.

Given the importance of van der Waals interactions, capturing their effects accurately in computational modeling is essential. Several methods for including dispersion forces in DFT have been developed, but most of these use "dispersion correction" scheme in which van der Waals forces are reintroduced with atomistic force-field correction[39–43]. Another popular approach is to incorporate dispersion energies as a functional of electronic density ($n(\mathbf{r})$), enabling a self-consistent treatment.

## 3.1 Density functional theory

In DFT, the ground-state energy and subsequent properties of a given many-electron system are defined as a functional of $n(\mathbf{r})$. Hohenberg-Kohn theorem states that these properties are uniquely defined by $n(\mathbf{r})$ and, in principle, an exact density functional can provide an exact description of the system. However, the exact form of the density functional to express the energy is unknown. Kohn-Sham approach or Kohn-Sham DFT gives a practical form to the Hohenberg-Kohn theorem. The total wavefunction is constructed from non-interacting single-particle (Kohn-Sham) wavefunctions $\psi_i^{\mathrm{KS}}(\mathbf{r})$, where the density can be defined as

$$n(\mathbf{r}) = \sum_i |\psi_i^{\mathrm{KS}}(\mathbf{r})|^2 \,. \tag{3.1}$$

Within Kohn-Sham theory, the total energy is given by

$$E[n] = T_{\mathrm{s}}[n] + U_{\mathrm{s}}[n] + U_{\mathrm{en}}[n] + E_{\mathrm{xc}}[n] \,, \tag{3.2}$$

where $T_s$ and $U_s$ are the non-interacting kinetic, and electrostatic energy respectively, and are given by

$$\begin{aligned} T_{\mathrm{s}}[n] &= \sum_i \int \psi_i^{\mathrm{KS}} \frac{-\hbar^2\nabla^2}{2m} \psi_i^{\mathrm{KS}^*} \, d\mathbf{r} \,, \\ U_{\mathrm{s}}[n] &= \frac{1}{2} \iint q^2 \frac{n(\mathbf{r})n(\mathbf{r}')}{|\mathbf{r}-\mathbf{r}'|} d\mathbf{r} d\mathbf{r}' \,, \end{aligned} \tag{3.3}$$

where $m$ and $q$ are the mass and charge of an electron. $U_{\text{en}}[n] = \int V_{\text{en}}(\mathbf{r})n(\mathbf{r})d\mathbf{r}$ is the electron-nucleus interaction where $V_{\text{en}}$ is called the external potential and is the potential that electrons feel from the nuclei. The other interacting many-body electron effects are separated as exchange-correlation energy term $E_{xc}[n] = (T[n] - T_s[n]) + (U_{ee}[n] - U_s[n])$. Here, $T[n]$ is the kinetic energy of the many-electron system and $U_{ee}[n]$ is the many-electron interaction energy.

DFT, similar to the Hartree-Fock method, employs a "trial wavefunction," implying that the ground state energy can be determined by minimizing the energy with respect to the parameters used to construct one-electron wavefunctions. This is known as the variational principle. By taking the partial derivative of the energy with respect to the wavefunctions while maintaining the constraint that the wavefunctions are orthonormal (omitting the derivation process), the Kohn-Sham ground state energy is defined as follows,

$$E[n] = \sum_i \epsilon_i^{\text{KS}} - \frac{1}{2}\iint q^2 \frac{n(\mathbf{r})n(\mathbf{r}')}{|\mathbf{r}-\mathbf{r}'|}d\mathbf{r}d\mathbf{r}' + E_{\text{xc}}[n] - \int V_{\text{xc}}(\mathbf{r})n(\mathbf{r})d\mathbf{r}\,, \quad (3.4)$$

where $\epsilon_i^{\text{KS}}$ are the eigenvalues of the Kohn-Sham single-electron equation and $V_{\text{xc}}$ is the exchange-correlation potential and is given by

$$V_{\text{xc}}(\mathbf{r}) = \frac{\partial E_{\text{xc}}(\mathbf{r})}{\partial n(\mathbf{r})}\,. \quad (3.5)$$

The Kohn-Sham ground state energy equation should be solved self-consistently. Because $\epsilon_i^{\text{KS}}$ depends on the single-electron wavefunctions, the self-consistent loop should involve the wavefunctions.

Because the exact form of $E_{\text{xc}}$ is unknown, finding its analytical expressions has led to many approximations. The simplest one is the local density approximation (LDA) where the many-body effects are approximated solely as a function of the electron density. An improvement over LDA is the semi-local generalized gradient approximation (GGA), which incorporates not only the electron density but also the density gradient $|\nabla n(\mathbf{r})|$. This addition enhances the short-range nature of the functional and allows for a better description of systems with inhomogeneous electron density, such as molecules. While GGA represents an improvement over LDA in capturing the local variations in electron density, its accuracy is still insufficient for certain materials with regions separated by low-electron densities. Examples of such materials include layered materials and molecular crystals. In other words, GGA has no information about distant electron densities, leading to the lack of long-range correlation between separated electrons in GGA energies.

## 3.2 The Chalmers-Rutgers van der Waals density functional

The Chalmers-Rutgers van der Waals density functional (vdW-DF) is an example of a functional that incorporates a non-local treatment of correlation to account for van der Waals interactions[44–46]. In general, vdW-DF functional takes the

following form,

$$E_{\rm xc}[n] = E_{\rm x}^{\rm GGA}[n] + E_{\rm c}^{\rm LDA}[n] + E_{\rm c}^{\rm nl}[n]\,, \tag{3.6}$$

which mixes the exchange energy at GGA level ($E_{\rm x}^{\rm GGA}[n]$) with the LDA correlation ($E_{\rm c}^{\rm LDA}[n]$) and vdW-DF non-local correlation. The non-local correlation energy is defined as

$$E_{\rm c}^{\rm nl}[n] = \frac{1}{2}\int d^3\mathbf{r}_1 \int d^3\mathbf{r}_2\, n(\mathbf{r}_1)\,\phi(\mathbf{r}_1,\mathbf{r}_2)\,n(\mathbf{r}_2)\,, \tag{3.7}$$

where a kernel function $\phi(\mathbf{r}_1,\mathbf{r}_2)$ connects two density regions $n(\mathbf{r}_1)$ and $n(\mathbf{r}_2)$. The interaction between the density regions is governed by two dimensionless parameters $D$ and $\delta$, i.e., $\phi(\mathbf{r}_1,\mathbf{r}_2) = \phi(D,\delta)$. The effective scale $D$ determines the range of the interaction and is defined as

$$D = \frac{1}{2}\left(q_0(\mathbf{r}_1) + q_0(\mathbf{r}_2)\right)|\mathbf{r}_1 - \mathbf{r}_2|\,, \tag{3.8}$$

where $q_0(\mathbf{r})$ is the local responsivity and is a function of the local density and the gradient of density ($s(\mathbf{r})$) and is given by

$$q_0(\mathbf{r}) = \left(\frac{\epsilon_c^{\rm LDA}}{\epsilon_x^{\rm LDA}} + 1 - \frac{\rm Z_{ab}}{9}s(\mathbf{r})^2\right)k_{\rm F}(\mathbf{r})\,, \tag{3.9}$$

where $k_{\rm F}(\mathbf{r})$ represents the local Fermi vector, while $\epsilon_x^{\rm LDA}$ and $\epsilon_c^{\rm LDA}$ denote the energy per particle of LDA exchange and correlation, respectively. $\rm Z_{ab}$ is equal to $-0.849$ for the first generation of vdW-DF (vdW-DF1). The other parameter $\delta$ is the relative difference in $q_0(\mathbf{r})$ and is given by

$$\delta = \frac{|q_0(\mathbf{r}_1) - q_0(\mathbf{r}_2)|}{q_0(\mathbf{r}_1) + q_0(\mathbf{r}_2)}\,. \tag{3.10}$$

Fig. 3.1 depicts the vdW-DF kernel. In the homogenous electron density limit where $\delta = 0$, the repulsive and attractive part of the kernel cancels out each other, and the non-local correlation contribution to the energy vanishes seamlessly. In addition, the shape of the kernel with respect to $D$ determines the range of the interaction between two density regions. For instance, for an average value of $q_0 \approx 2$ Bohr$^{-1}$, the major contributing interaction range is confined to a sphere with a radius of approximately 2.11 Å, as further explained in Sec. 3.4.

The GGA exchange energy improves upon the LDA exchange by incorporating additional information about the electron density gradient and is defined as

$$E_x^{\rm GGA}[n] = \int d^3r\, n(\mathbf{r})\,\epsilon_x^{\rm LDA}(n(\mathbf{r}))\,F_x(s)\,, \tag{3.11}$$

where $F_x(s)$ is the exchange enhancement factor and is a function of reduced density gradient $s(\mathbf{r}) = |\nabla n(\mathbf{r})|/2(3\pi^2)^{1/3}n(\mathbf{r})^{4/3}$. It is evident that the shape of the enhancement factor can significantly affect the bonding in vdW-DF. [46, 47]. Fig. 3.2 shows the enhancement factors employed in different generations of vdW-DF functionals.

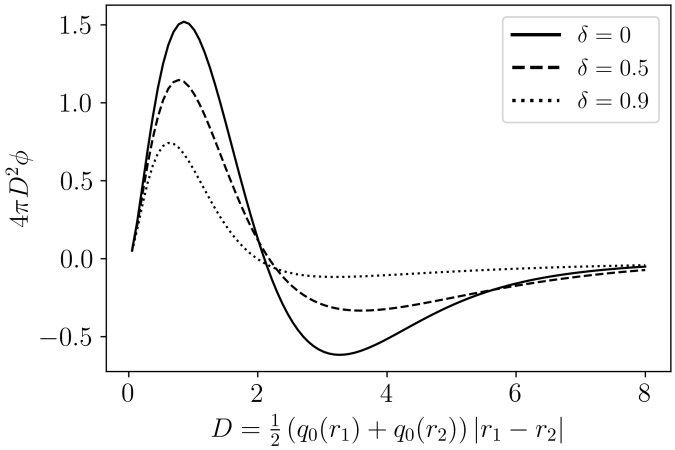


Figure 3.1: The universal vdW-DF kernel as a function of $D$ and $\delta$.

vdW-DF1[44] employs revised Perdew-Burke-Ernzerhof (revPBE)[48] exchange that demonstrates a more rapid increase in the low s-value regions ($s = 0.5 - 2$) compared to PBE[49] exchange. This has improved the underbinding problem previously observed with PBE in systems where dispersion energy contributes significantly to the total energy.[47, 50]. However, both revPBE and PBE become flat in the large $s$-region. This is shown to be related to the overestimation of binding separations in vdW-DF1. To overcome this, the second generation of the vdW-DF functional (vdW-DF2)[51] uses the revised Perdew-Wang (PW86r)[52] exchange with a monotonically increased shape in the large $s$-region that is proportional to $s^{5/2}$. As a result, vdW-DF2 has demonstrated improved accuracy in predicting lattice constants in molecular crystals. However, it tends to worsen the overestimation of layered and absorption systems. This observation can be attributed to the high slope of the $F_x(s)$ curve in the small $s$-region[46]. To address this issue, newer generations of vdW functionals, like consistent exchange vdW-DF (vdW-DF-cx)[53], have been developed, aiming to mitigate the problem. This improvement is evident in the lower panel of Fig 3.2 where CX and B86R[54] enhancement factors have a lower slope in $s$-region between 0.2 to 0.8.

## 3.3 Reduced density gradient analysis

Considering the importance of the enhancement factor in the performance of vdW-DF functionals, an analysis correlating the contributing $s$-regions in different classes of systems with the shape of the enhancement factor, and vice versa, can provide valuable insights into understanding vdW-DF and designing novel vdW-DF, as well as other types of DFT functionals. To only focus on the gradient component of the exchange energy, it is useful to subtract the LDA part

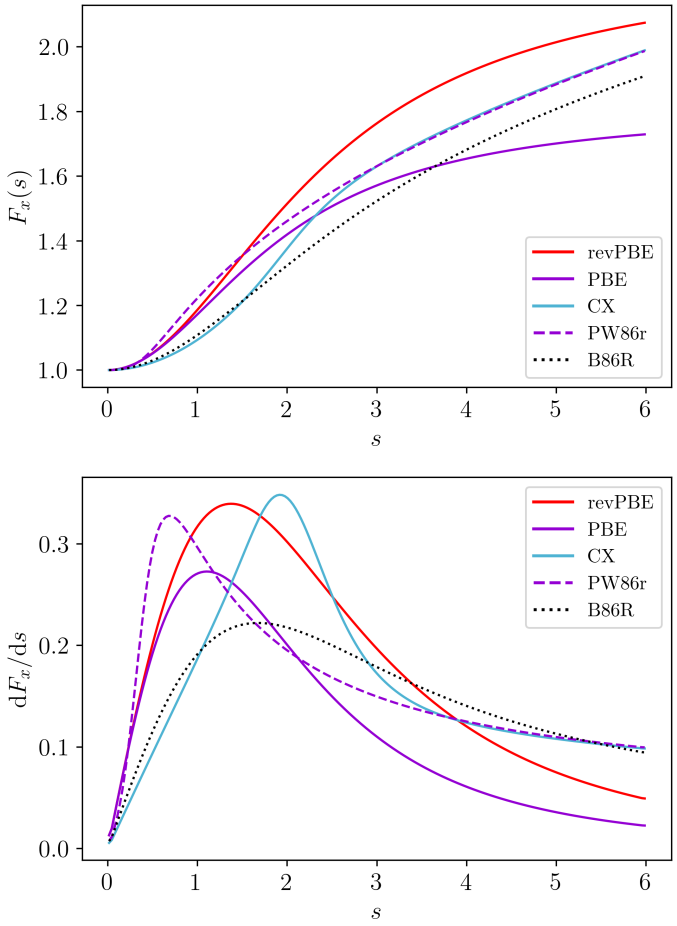


Figure 3.2: Exchange enhancement factors $F_x(s)$ (upper panel) and their derivatives (lower panel) used in different vdW-DF functionals.

from the $F_x(s)$ by defining the s-resolved gradient component exchange energy as

$$e_x(s) = \int d^3r\, n(\mathbf{r})\, \epsilon_x^{\mathrm{LDA}}(n(\mathbf{r}))\, [F_x(s) - 1]\, \delta(s - s(\mathbf{r}))\,, \tag{3.12}$$

$e_x(s)$ is a useful term that allows for a step-by-step integration of $s$ values, facilitating the investigation of contributions from $s$ regions with the same value (isosurfaces) to the exchange energy. The $s$-integrated exchange energy is then defined as follows,

$$E_x(s) = \int_0^s e_x(s')\, ds'\,. \tag{3.13}$$

In Fig. 3.3, we have plotted the $s$-integrated and $s$-resolved gradient component exchange energy barrier of double PT in a formic acid dimer. By comparing the

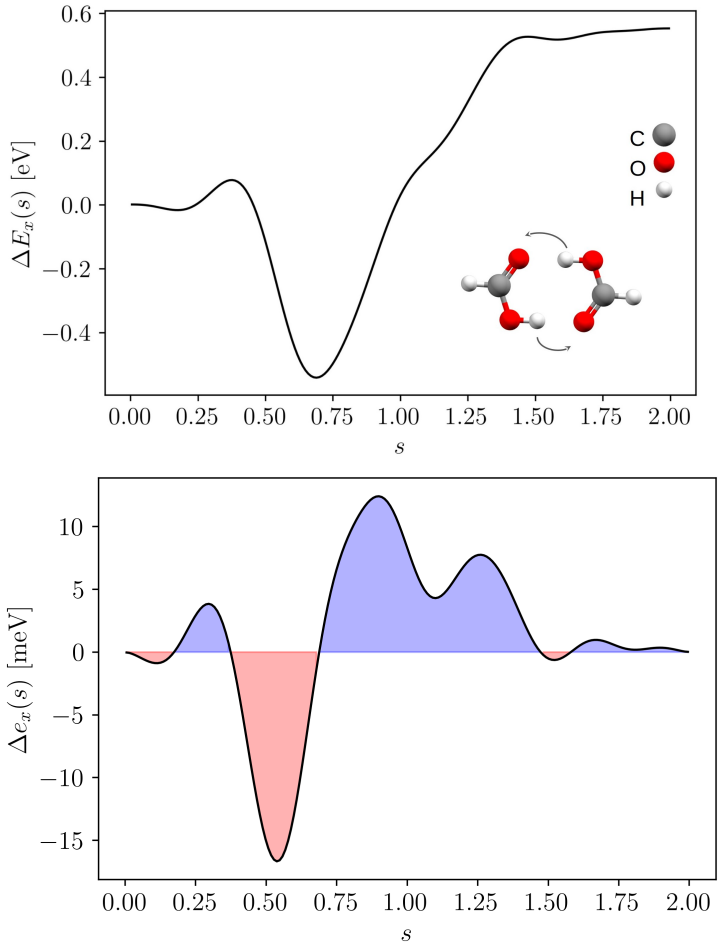


Figure 3.3: In the upper panel, the $s$-integrated exchange proton-transfer barrier ($\Delta E_x(s)$) is depicted, and in the lower panel, the $s$-resolved gradient component exchange barrier ($\Delta e_x(s)$) of the formic acid dimer is plotted for vdW-DF2 (PW86r). The positively and negatively contributing $s$ regions are colored in blue and red, respectively.

contribution of different $s$ regions with the shape of $F_x(s)$ as plotted in Fig 3.2, one can pinpoint important $s$ regions for a specific system. For instance, regions associated with $0.4 < s < 0.75$ contribute negatively and reduce the barrier $\Delta E_x(s)$ and $s > 0.75$ increase the barrier. It is evident that PW86r attains higher exchange energy towards the end compared to the CX and revPBE exchanges. This can be attributed to the higher slope and values of $F_x(s)$ for PW86r in the

increasing $s$ regions. In paper I, we showed that the higher exchange energy contribution of PW86r is important for the accurate PT barrier prediction of vdW-DF2.

Previously, $s$-analysis has been successfully used to explain and analyze the performance of different DFT exchanges in predicting the interaction energies of isolated molecules[50]. In paper I, we used it to analyze and explain the performance of various exchange functionals within the framework of vdW-DF theory.

## 3.4 Non-local correlation analysis of vdW-DF

In a manner analogous to the reduced density gradient approach used for analyzing the exchange energy, we can follow a similar strategy to project the non-local correlation energy onto the local responsivity parameter $q_0$. The rationale behind this choice lies in the crucial role played by $q_0$ in determining the range and subsequently, the nature of the non-local interaction through the non-local correlation kernel as is evident from Eq. 3.8. As a result, the

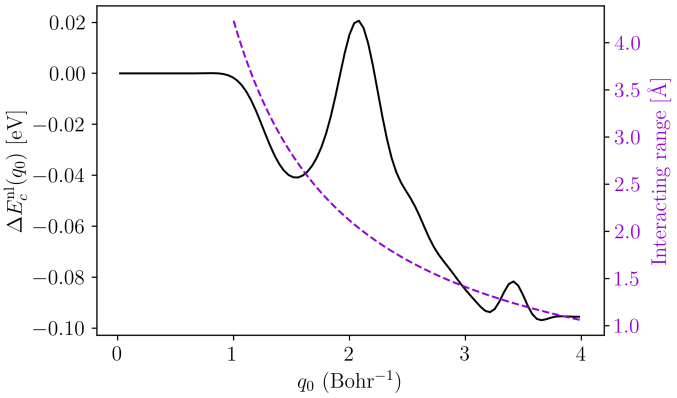


Figure 3.4: $q_0$-integrated non-local correlation proton-transfer barrier of formic acid dimer is plotted for vdW-DF functional. The dashed line plots the interaction range of the non-local correlation kernel for different $q_0$ values.

$q_0$-resolved non-local correlation is given by

$$e_c^{\mathrm{nl}}(q_0) = \int d^3r\, e_c^{\mathrm{nl}}(\mathbf{r})\, \delta(q_0 - q_0(\mathbf{r}))\,, \tag{3.14}$$

where $e_c^{\mathrm{nl}}(\mathbf{r})$ is the spatial non-local correlation density and is defined as

$$e_c^{\mathrm{nl}}(\mathbf{r}) = \frac{n(\mathbf{r})}{2} \int d^3\mathbf{r}'\, n(\mathbf{r}')\, \phi(\mathbf{r}, \mathbf{r}')\,. \tag{3.15}$$

Similar to the Eq. 3.13, the $q_0$-integrated non-local correlation energy is

$$E_c^{\mathrm{nl}}(q_0) = \int_0^{q_0} e_c^{\mathrm{nl}}(q_0')\, dq_0' \,. \tag{3.16}$$

Fig. 3.4 shows the $q_0$-integrated non-local correlation for the formic acid dimer. Similar to $s$-integrated energy curves, the $q_0$ curve also contains important information about the regions in the space that contribute to the energy. Here, for example, the contributing range is $1 < q_0 < 4$, and from $q_0 > 2.2$, the associated regions are contributing negatively to the non-local correlation energy. Comparing this curve with the vdW-DF kernel (Fig. 3.1), we can define the range of interaction associated with $q_0$ isosurfaces as $d = |\mathbf{r}_1 - \mathbf{r}_2| = \frac{8\times0.53}{q_0}$, where 8 is the value where the kernel flattens out—regions with $D > 8$ does not contribute much to the energy.

Chapter 4

# Crystal structure prediction

Crystal structure prediction (CSP) involves predicting the three-dimensional arrangement of molecules/atoms in their solid-state form using only limited information, such as a chemical diagram or the type of atoms involved [55]. In molecular crystals, the methodology is based on generating many crystal structures from the molecules and ranking them by their computed lattice energies [56]. Often, the output of a CSP method is demonstrated as a plot of lattice energy versus crystal density. A reliable CSP method would rank "true" crystal structures or polymorphs—in the case of polymorphism—of a given substance in the proximity of the global minimum on the CSP energy landscape.

In practice, the method provides valuable data that can be used for different purposes. One application is in the field of material design and discovery, where new materials with specific properties are designed by predicting their crystal structures before they are synthesized. This can help to accelerate the discovery of new materials for various applications, including energy storage, catalysis, and electronics[57]. CSP has also been widely used by the pharmaceutical industry to minimize the probability of the appearance of unforeseen polymorphs. One example is the case of ritonavir, an antiviral medication, that proved to have an unforeseen, more stable polymorph with less water solubility. The medications on the market gradually transformed to a more stable phase and became pharmacologically ineffective. The huge financial and medical consequences of the ritonavir case, made CSP an important screening step for detecting possible polymorphs of medications [58]. Furthermore, CSP can be complemented by other experimental methods to determine crystal structures more effectively. Methods such as X-ray diffraction patterns and solid-state nuclear magnetic resonance spectroscopy can work in synergy with CSP, helping to narrow down the search space and reduce computational costs. Alternatively, the landscape produced by CSP can assist in crystal structure determination by matching experimental data with low-energy CSP structures[59].

## 4.1 CSP methodology

An ideal CSP method tries to define and minimize the Gibbs free energy at a given pressure and temperature with respect to all atomic, molecular, and unit cell degrees of freedom. In a more simplified manner, the problem can be defined as the minimization of the internal energy by neglecting temperature and pressure effects [60]. Now, the problem can be divided into two tasks: search through multidimensional configurational space using an efficient sampling method to include all local minima corresponding to each possible metastable packing, and finding a definition for the internal energy for a given crystal structure.

Combining these two steps at the end gives us a potential energy surface with discrete levels of energy corresponding to each of the local minima, referred to as the CSP landscape [60, 61]. The internal energy can be estimated at different levels of theories, from *ab initio* to semi-empirical atomistic potentials. However, one rational approach is to increase the accuracy of methods while moving toward the global minimum and apply the most accurate method on a limited region close to the global minimum. Fig. 4.1 shows the workflow

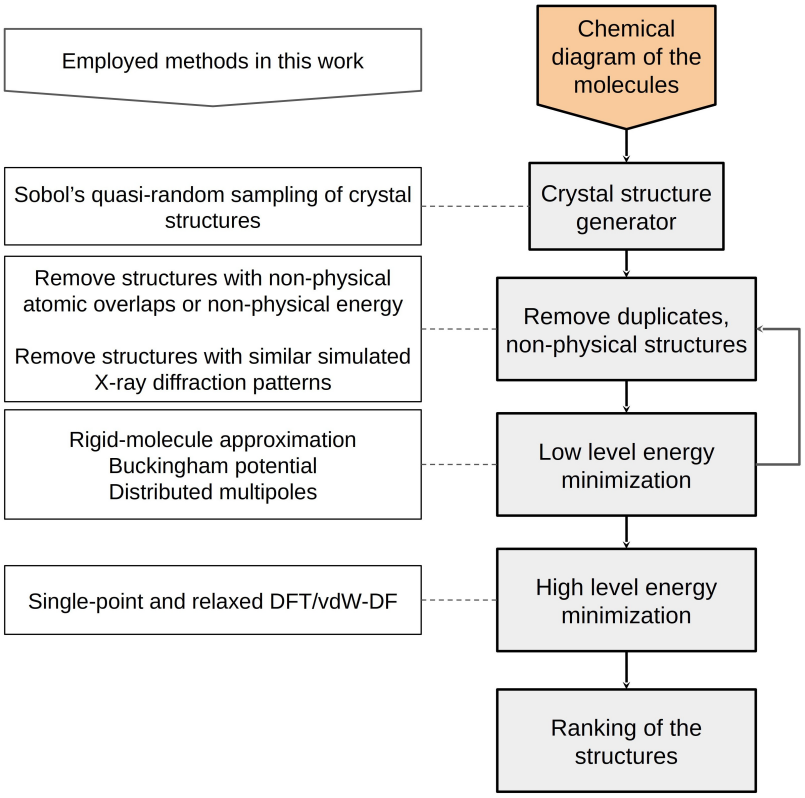


Figure 4.1: A common CSP workflow for molecular crystals.

of a typical CSP procedure. In the first step, crystal structures should be generated to cover different structural packing. One commonly used method is quasi-random sequences, which can produce a homogeneous sampling of crystal structure parameters. More detailed information regarding the selection of crystal structure parameters will be provided shortly.

In the next step, duplicate structures and structures with non-physical packing should be removed. Simulating X-ray diffraction patterns can be used to remove duplicate structures. This stage can be synchronized with the energy minimization step, where a computationally feasible method, balancing

accuracy and computational cost, is employed to provide a preliminary ranking of the generated structures. Simultaneously, this step identifies and eliminates structures exhibiting unphysically high energies and/or structures that the method cannot minimize the energy after a defined number of iteration steps. Finally, higher-level energy minimization methods, such as DFT with a suitable functional, can be applied. In the context of molecular crystals, functionals that include van der Waals dispersion energies, such as PBE-D3[42], are more commonly used. Depending on the complexity of the landscape, vibrational and configurational free energies can be used for the final ranking of the structures.

### 4.1.1 Search methods

An optimum searching method should visit all possible local minima in the configurational space of crystal packing, prioritizing denser sampling in regions with lower energy. Additionally, it should also be computationally feasible. Several methods have been proposed to achieve these goals. One straightforward approach involves conducting a comprehensive grid search based on parameters that define a crystal structure[55]. However, this method is computationally expensive and spends equal time sampling unnecessary high-energy minima as it does to sample more interesting low-energy minima.[56]. Another approach is

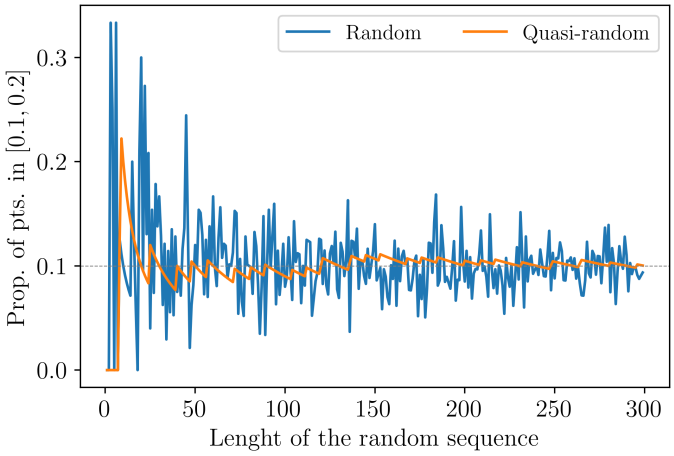


Figure 4.2: The proportion of the points within $[0.1, 0.2]$ is plotted against the length of the random sequences generated by pseudo-random and quasi-random methods.

to randomly search the space using pseudo-random or, for a more homogenous sampling, quasi-random selection of crystal structure parameters. Quasi-random sequences guarantee a uniform distribution of sampling points across an interval by imposing a low discrepancy constraint. This constraint ensures that the proportion of points falling within a sub-interval is as close as possible to the

probability of measuring that sub-interval, resulting in a more homogeneous distribution of points throughout the entire interval. Fig. 4.2 compares sampling of the $[0.1, 0.2]$ interval by pseudo- and quasi-random methods. For generating low-discrepancy quasi-random sequences, we used Sobol's sequence [62]. By increasing the sampling points—the length of the random sequence—we can see that the quasi-random sequence converges more quickly to 0.1. This value is the probability of measuring the length of the interval divided by the whole range of sampling. In the realm of CSP, many groups have implemented quasi-random sampling to search the configurational space of crystal structures.

In our CSP calculations, we employed the methodology developed by Case et al., as detailed in their work [61]. This methodology has been effectively implemented within the GLEE program[63], which is suitable for molecular crystals. In this approach, the molecular geometries are fixed to their gas-phase optimized geometry, usually relaxed at the B3LYP[64] level of theory. In the next step, as illustrated in Fig.4.3, molecular positions and orientations, in combination with lattice parameters, are sampled using the Sobol method [62]. Applying the symmetry operation to the asymmetric unit within a space group yields the positions and orientations of molecules inside the unit cell. The volume of the unit cell is constrained by a parameter, which is defined as the sum of all boxes that encompass the molecules in the unit cell. In the case of many nonphysical overlapping molecules in the unit cell, this parameter can be increased.

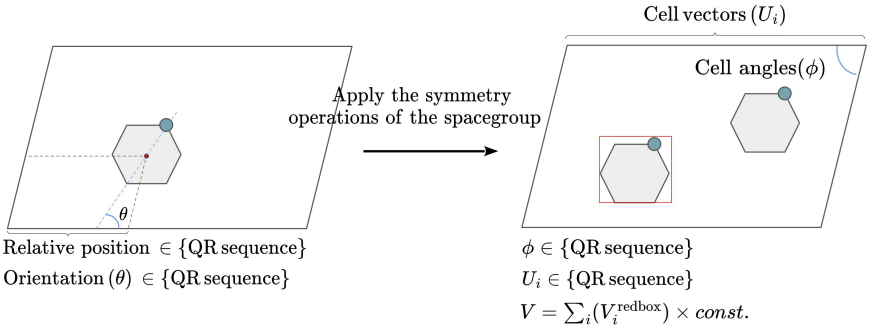


Figure 4.3: Schematic illustration of generating a quasi-random (QR) molecular crystal structure. (Left) Relative positions and orientations of the molecules in the asymmetric unit are sampled using QR sequences. (Right) Symmetry operations are applied to make the unit cell. Cell vectors and cell angles are sampled using a QR sequence with the constraint that the cell volume ($V$) is fixed to the sum of volumes of the red boxes ($V^{\text{redbox}}$) surrounding the molecules, multiplied by a constant.

The sampling procedure can also be combined with the energy evaluation of generated crystal structures. In this approach, each geometry-optimized generated structure is associated with one of the local minima, and the

completeness of sampling can be assessed by comparing the number of visited local minima to the total number of generated structures[56].

Yang et al.[65] have proposed a method that combines quasi-random sampling and Monte Carlo moves. In this approach, the CSP landscape is first properly sampled using a quasi-random sequence, and then Monte Carlo moves are performed on each of the generated structures through structural perturbations. The acceptance probability is defined as,

$$P_{a\to b}^{\mathrm{acc}} = \min[e^{-(E_b - E_a)/kT}, 1]\,, \tag{4.1}$$

where $E_{\mathrm{a}}$ and $E_{\mathrm{b}}$ are (lattice) energy of the initial and perturbed structures respectively and $T$ is the temperature. It has been shown that this method maintains the advantages of quasi-random sampling while also offering better sampling of low-energy structures and more efficient locating of the global minimum.

A possible drawback is that the Monte Carlo moves can be trapped in the local minima. One approach to resolving this problem is to use the Monte Carlo simulated annealing method. This involves carrying out Monte Carlo moves at various temperatures to ensure that the landscape has been extensively sampled.

### 4.1.2 Energy minimization of structures

As previously mentioned, the choice of energy minimization methods can vary in terms of accuracy and computational cost, depending on the proximity to the CSP global minimum. Particularly, when dealing with the generation of thousands of random crystal structures, the chosen method should offer an appropriate balance between accuracy and computational feasibility. The GLEE program has an interface with DMACRYS software [66] that employs the anisotropic Buckingham-type atomistic potential, which includes dispersion and repulsion terms and has the form

$$E_{MN} = \sum_{i\in M, j\in N} A^{IJ}\exp(-B^{IJ}r_{ij}) - C^{IJ}r_{ij}^{-6} + E_{ij}^{\mathrm{DMA}}\,, \tag{4.2}$$

Where $i$ and $j$ are indices corresponding to atoms of type $I$ and $J$ which belong to the molecules $M$ and $N$ respectively. The parameters $A^{IJ}$, $B^{IJ}$, and $C^{IJ}$ are obtained by fitting to the experimental data of azahydrocarbon[67] and oxohydrocarbon[68] organic crystals, denoted here as FIT potential [69]. The potential incorporates electrostatic interactions $E_{ij}^{\mathrm{DMA}}$, taking into account atom-centered multipoles up to rank 4. The multipoles are generated using a distributed multipole analysis method [70] applied to the charge density. GLEE generates and utilizes these multipoles through the GDMA[70] program, which currently interfaces with GAUSSIAN, PSI4[71], and NWChem[72] programs. The method treats the molecules as a rigid body based on their gas-phase geometry-optimized structures. In the case of a flexible molecule, the possible conformers should be identified and used in a separate CSP study and the results integrated to find the global minimum and possible polymorphs.

### 4.1.3 Validation of the CSP method for OPTFes

In the case of OPTFe materials, the FIT potential[73] proved effective in generating an initial CSP landscape with experimental structures falling within the low-energy range. We have assessed the efficacy of the FIT potential

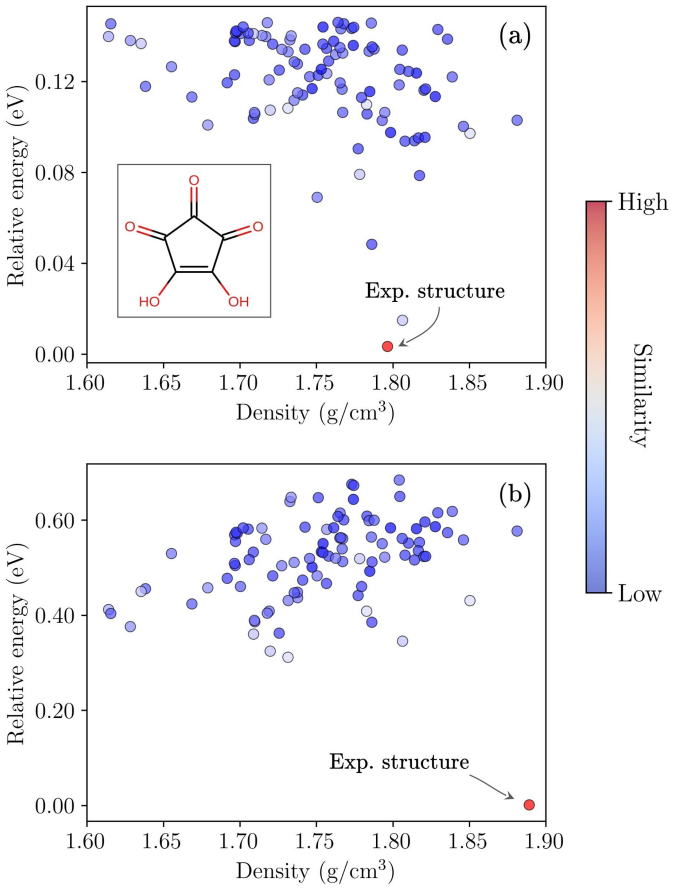


Figure 4.4: Relative energy per molecule versus density of croconic acid (GUMMUW11) structures is plotted employing (a) FIT energies, and (b) single-point DFT energies using vdW-DF2 functional. The structures are colored based on their similarity to the experimental structure. The degree of similarity is defined using the COMPACK algorithm [74], with "low" indicating zero alignment and "high" indicating complete alignment between the compared structures.

combined with GLEE for quasi-random sampling of structures to predict the crystal structure of croconic acid. This structure involves the transfer of four protons through a three-dimensional hydrogen-bonded network.

Panel (a) in Fig. 4.4 illustrates the ranking of structures from the CSP landscape generated by the FIT potential energies. The experimental structure is identified as the global minimum. Further analysis through single-point energies confirms that the experimental structure occupies the global minimum, exhibiting a large energy gap of 0.3 eV compared to the closest alternative structure.

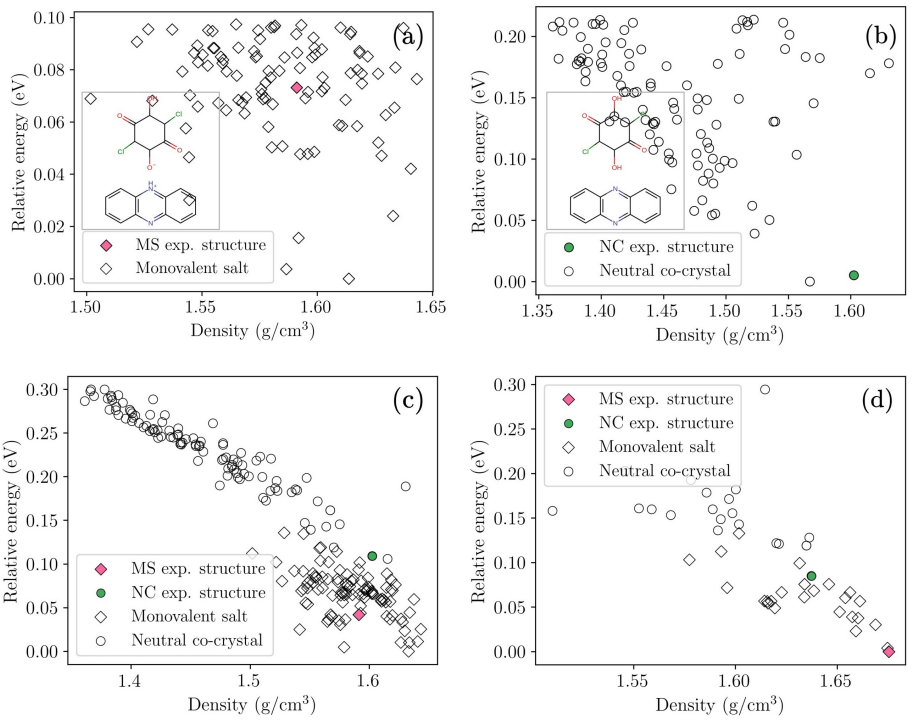


Figure 4.5: Relative energy per molecule pairs versus density for monovalent salt (MS) and neutral co-crystalline (NC) forms of phenazinium chloranilate is plotted at three levels of accuracy: (a) and (b) FIT energies, (c) single-point DFT energies, and (d) fully relaxed DFT energies using vdW-DF2.

The other example is phenazinium chloranilate which is a known acid-base OPTFe salt. This compound exhibits two protonation states: a low-temperature ferroelectric phase (MAMPUM03), characterized as a monovalent salt (MS), and a high-temperature paraelectric phase (MAMPUM04), which has a neutral co-crystalline (NC) form. In Panel (a) of Fig. 4.5, MS structures are ranked based on the CSP landscape obtained using the FIT potential. The experimental structure, colored in red, is currently ranked 42nd out of more than 100,000 randomly generated structures. In panel (b), the CSP landscape for the NCs is presented, where the FIT potential demonstrates improved performance, with the experimental NC now ranked second. Moving to panel (c), we combined

the MS and NC structures and optimized them using the single-point vdW-DF2 functional. In this case, the MS experimental structure is ranked 20th, while the NC retains its second-place ranking among neutral structures. Finally, in panel (d), we have plotted the 20 lowest structures selected from the single-point DFT landscape that are fully relaxed using the vdW-DF2 functional. Given that DFT calculations are conducted at absolute zero temperature, the low-temperature MS now occupies the global minimum, while the higher-temperature NC is ranked 20th. The concluding example is QUWZIS, which is a NC of 2,3,5,6-

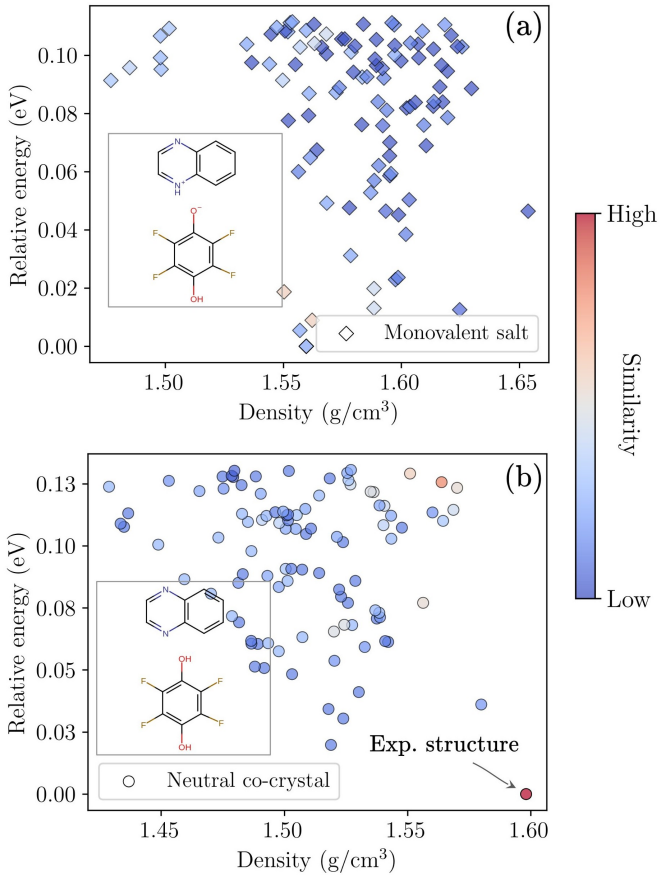


Figure 4.6: Relative energy per molecule pairs versus density for 2,3,5,6-tetrafluorobenzene-1,4-diol and quinoxaline (QUWZIS) is plotted for (a) monovalent salts (b) neutral co-crystals using FIT energies. The structures are colored based on their similarity to the experimental structure. The degree of similarity is defined using the COMPACK algorithm, with "low" indicating zero alignment and "high" indicating complete alignment between the compared structures.

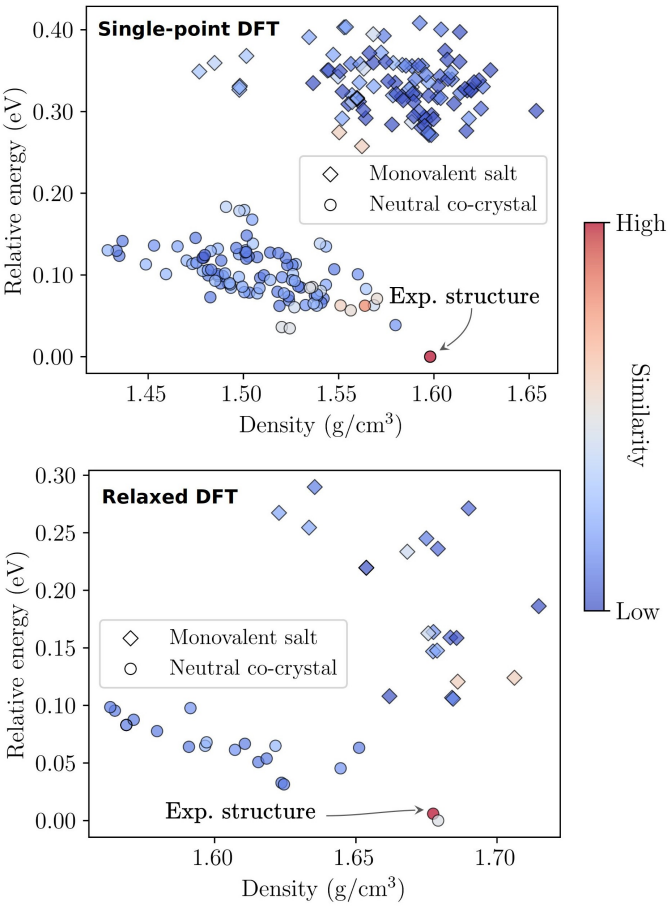


Figure 4.7: Relative energy per molecule pairs versus density for QUWZIS is plotted at two levels of accuracy: single-point DFT energies, and fully relaxed DFT energies using vdW-DF2. The structures are colored based on their similarity to the experimental structure. The degree of similarity is defined using the COMPACK algorithm, with "low" indicating zero alignment and "high" indicating complete alignment between the compared structures.

Tetrafluorobenzene-1,4-diol and quinoxaline. This can be a different test for the FIT potential and the vdW-DF2, given that the stable co-crystal has a neutral form. Fig. 4.6 shows the CSP landscape, including both MS and NC structures. Following the same procedure as MAMPUM03, the landscape is first generated with the FIT potential. The experimental structure is already in the global minimum of the NC (Panel (b)). The upper panel of Fig. 4.7 shows re-ranked and combined structures using single-point DFT energies. We observe that NCs

have aggregated in the low-energy region, with the experimental structure in the global minimum. In the lower panel, fully relaxed structures from low-energy regions of MS and NC are plotted. The global minimum is occupied by the experimental structure and another NC with high similarity to the experimental structure. In a situation where the energy difference between structures in the proximity of the global minimum is very small, methods with higher accuracy, such as DFT with hybrid functionals and free energies, including vibrational entropy, can help to identify the stable structure.

These results demonstrate that the combination of the semi-empirical FIT potential with the more accurate single-point and fully relaxed DFT calculations at the vdW-DF level of theory can effectively identify potential polymorphs in hydrogen-bonded molecular crystals, such as OPTFe systems.

### 4.1.4 Clustering

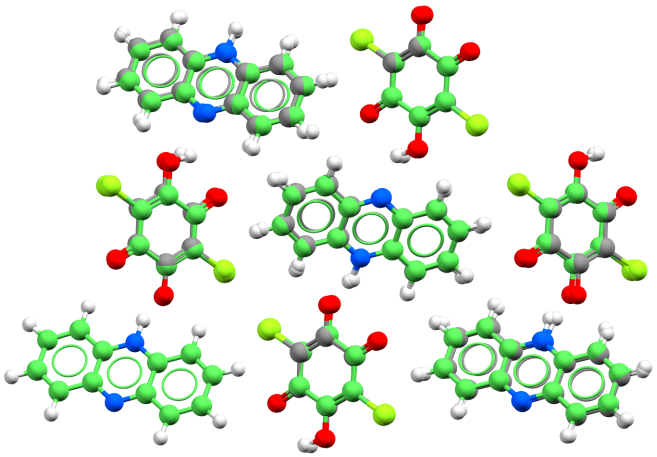

Figure 4.8: The comparison of the predicted crystal structure of phenazinium chloranilate co-crystal generated from the GLEE program (FIT potential) with MAMPUM03. The COMPACK algorithm, employing a 30% distance and 30°angle tolerance, successfully superimposed all 30 molecules of the cluster with RMSD of 0.17. The predicted structure is depicted in green for visual reference.

During the random structure generation and subsequent DMACRYS energy minimization, many duplicates with a high degree of similarity may be produced. A clustering method at this stage can help remove duplicate structures and provide a better overview of the convergence of the maximum number of unique structures that can be produced within each space group [61]. One widely employed technique involves comparing the simulated X-ray powder diffraction patterns of newly generated and optimized structures against a reference dataset

of previously generated structures. Alternatively, crystal structures can be compared. One example is the COMPACK algorithm[74]. This algorithm assesses the interatomic distances within predefined molecular clusters, seeking matching patterns, and subsequently superimposing structures with consideration for specified distance and angle tolerances. The evaluation of structural similarity is quantified using the Root Mean Square Deviation (RMSD) and the count of matched molecules. Clustering methods can also be used as a post-processing tool to group similar structures within the CSP landscape.

Fig. 4.8 shows the performance of the COMPACK algorithm on the predicted structure resulting from the CSP calculation of the phenazinium chloranilate co-crystal as illustrated in Fig. 4.5. The predicted monovalent salt structure is superimposed on the experimental MAMPUM03 structure. Using the COMPACK algorithm with a 30% distance and 30° angle tolerance, we find that the predicted structure closely resembles the experimental structure, matching all 30 molecules in the cluster with an RMSD of 0.17.

# Chapter 5

# Conclusion and outlook

## 5.1 Summary of papers

**Paper I** focuses on benchmarking various exchange-correlation functionals, which includes different variants of vdW-DF functionals and dispersion-corrected functionals. The aim is to evaluate their accuracy in predicting PT barriers in small organic molecules. The results highlight the significance of both non-local vdW-DF correlation and choice of appropriate exchange in improving the underestimation of barriers observed with GGA functionals. In our analysis of exchange energies using the reduced density gradient, we found that the exchange variants of vdW-DF1 and vdW-DF2 exhibit a more favorable $F_x(s)$ shape with a higher slope in the contributing $s$ regions. This characteristic leads to a higher exchange barrier, effectively improving the previously observed underestimation. Incorporating hybrid exchange also improved the barriers. vdW-DF-cx0 and vdW-DF2-B86R0, the hybrid versions of two of the employed vdW-DFs, showed a good performance, though B3LYP was slightly more accurate. Furthermore, our local responsivity ($q_0$) analysis reveals that the vdW-DF non-local correlation contribution to the barrier has a repulsive nature and plays a crucial role in improving the underestimation of GGA correlation energy.

**Paper II** provides a procedure for mining CSD in search of potential OPTFe materials. The methodology primarily relies on the identification of polar organic crystals with pseudo-inversion symmetry. As illustrated in Fig. 2.7, among over a million structures, only 7 new candidates exhibited promising ferroelectric properties. Additionally, we presented a benchmark set comprising 14 OPTFe structures, by which we assessed several exchange-correlation functionals in predicting lattice parameters compared to experimental structures. Interestingly, similar to predicting PT barriers, vdW-DF2 exhibits a good performance in predicting lattice parameters. This enabled us to employ a consistent method for calculating barriers and properties, such as spontaneous polarization.

**Paper III** demonstrates a mining procedure to identify potential ferroelectric plastic crystals. Drawing inspiration from previously reported plastic crystal structures, a set of criteria, including globularity and a limited number of hydrogen bonds, was defined to screen the CSD. Out of more than a million structures, 75 crystals exhibited ferroelectric properties. Spontaneous polarizations were also calculated using the vdw-DF-cx functional, based on a previous benchmarking study[32].

**Paper IV** describes the design of novel acid-base OPTFe salts. These salts comprise two molecular types in their structure, offering the opportunity to explore various acid-base combinations and correlate them with the properties of the designed crystal. Replacing acid and/or base molecules can change the packing of the designed crystal. To predict the packing, we employed the CSP method. The optimum ferroelectric packing should have a polar space group, a connected PT network, and a monovalent salt protonation state. The molecules were inherently rigid, which was suitable for our rigid-body CSP approach. However, different protonation states needed to be included in our CSP calculations, which increased the computational cost. To reduce the cost, we examined different protonation states of all our molecular combinations in a template packing. In the first step, we excluded molecular combinations where the MS were not dynamically stable. The remaining combinations were assessed using the CSP method. In the CSP calculations, the energy landscape was first generated using the FIT potential. Subsequently, structures in the low-energy region were re-ranked based on single-point DFT and relaxed DFT energies. The results showed three molecular combinations with ferroelectric packing and two with anti-ferroelectric packing. The calculated spontaneous polarizations for the ferroelectric structures enhanced significantly compared to the previously reported acid-base OPTFes.

## 5.2 Outlook

### 5.2.1 Discovery

Our approach to discovering organic molecular ferroelectrics was based on defining quantitative models based on already identified material structures. These computationally inexpensive models were well-suited for application to extensive databases, such as the CSD. For OPTFe materials, the pseudosymmetry method showed its effectiveness by identifying almost all OPTFe entries in the CSD. However, the method could miss structures when ferroelectric switching significantly distorts the structures. This can be improved by replacing the pseudosymmetry method with a less strict method, for example, a method that can directly identify connected hydrogen-bonded paths. This can be integrated with the defined criteria for identifying plastic ferroelectrics with mixed mechanisms, such as PT-triggered rotational ferroelectrics. Moreover, by using this method, we can expand the search to the centrosymmetric space group, aiming for potential anti-ferroelectrics and/or ferroelectrics with only the paraelectric phase deposited in the CSD.

Another approach, which can also be combined with the pseudosymmetry method, involves using more advanced machine learning (ML) models trained on the structural features of previously identified compounds to discover new organic ferroelectrics. However, these models are not applicable here as they require training on large datasets, whereas the number of previously reported organic

ferroelectric compounds is limited; for example, OPTFes are restricted to around 20 compounds. Nevertheless, general ML methods developed for computing the properties of crystals can be incorporated into the search algorithms. For example, a model that can effectively predict the spontaneous polarization of crystals can be applied to identify polar materials with a defined high polarization.

### 5.2.2 Design

Our approach to designing novel acid-base OPTFe salts employed a CSP methodology to predict the packing of the designed structures. This methodology was based on rigid molecules in generating and energy minimization of the structures at the force-field level. This implies that the number of CSP calculations is dependent on the number of conformers of the molecules, and for highly flexible molecules, this can be computationally expensive. Moreover, in our method, conformers defined in the gas phase may differ from those within the crystal environment. This implies that the ranking of the structures can change significantly after the geometry optimization of the structure with *ab initio* methods. Additionally, energy minimization was carried out by a semi-empirical force field (FIT) fitted on experimental data of compounds with a limited set of chemical elements, and intermolecular coefficients were not available for any desired element.

One solution to the mentioned problem is replacing the FIT potential with a ML potential. These potentials can be trained on DFT-generated data of similar compounds, making them more accurate than conventional force fields. Additionally, conformers can be generated on-the-fly inside the crystal environment while (quasi-)randomly generating structures. As discussed in Sec. 4.1.1, this step can be integrated with Monte Carlo moves, resulting in the sampling of the configurational space limited to the low-energy region of the CSP landscape. As a result, employing this improved method can enable us to expand the chemical space in our design and, consequently, have a better description of structure-property relationships of organic molecular ferroelectrics. However, one important step in understanding these relationships is finding a method that can accurately predict the properties of the designed ferroelectric materials. The calculation of the spontaneous polarization can be straightforward if we can find a smooth path toward the hypothetical paraelectric phase and subsequently employ the Berry-phase method. However, calculating the coercive field and Curie temperature can be challenging since they depend on the understanding and modeling of the switching mechanism.

Molecular dynamics (MD) and/or Monte Carlo simulations can be used to model the switching of systems where the switching involves the movement and reorientation of molecules, such as in plastic crystals. However, for systems in which the switching involves the transfer of protons, quantum effects can contribute to the dynamics of the system, and more advanced MD simulations, such as path integral MD, may be required. In any case, it is essential to consider that the simulation cost for calculating ferroelectric properties should be significantly less than the cost of experimentally realizing the designed crystals.

Another approach with a much lower computational cost is to relate certain structural features and/or properties of the crystal, which can be calculated at a feasible cost, to the more expensive properties, such as the coercive field, of the designed crystal. In paper II, we related the PT barriers to the coercive fields of the previously reported OPTFes to obtain an estimation of the coercive fields of the crystals we found through our screening. With an efficient CSP method that allows the incorporation of desired molecules and accurately predicts the crystal packing, along with an efficient method to predict the desired properties of the crystal, we can aspire to design ferroelectric systems with optimal properties tailored for specialized applications.

# Bibliography


1. Horiuchi, S., Ishibashi, S., Kobayashi, K. & Kumai, R. Coexistence of normal and inverse deuterium isotope effects in a phase-transition sequence of organic ferroelectrics. *RSC Adv.* vol. 9, 39662–39673 (68 2019).
2. Valasek, J. Piezo-electric and allied phenomena in Rochelle salt. *Phys. Rev.* vol. 17, 475–481 (4 1921).
3. Von Hippel, A., Breckenridge, R. G., Chesley, F. G. & Tisza, L. High dielectric constant ceramics. *Ind. Eng. Chem.* vol. 38, 1097–1109 (1946).
4. Scott, J. F. Applications of modern ferroelectrics. *Science* vol. 315, 954–959 (2007).
5. Scott, J. F. & de Araujo, C. A. P. Ferroelectric memories. *Science* vol. 246, 1400–1405 (1989).
6. Solomon, A. L. Thiourea, a new ferroelectric. *Phys. Rev.* vol. 104, 1191–1192 (1956).
7. Horiuchi, S. *et al.* Above-room-temperature ferroelectricity and antiferroelectricity in benzimidazoles. *Nat. Commun.* vol. 3, 1308 (2012).
8. Krishna, G. R., Devarapalli, R., Lal, G. & Reddy, C. M. Mechanically flexible organic crystals achieved by introducing weak interactions in structure: supramolecular shape synthons. *J. Am. Chem. Soc.* vol. 138, 13561–13567 (2016).
9. Dong, K., Peng, X. & Wang, Z. L. Fiber/fabric-based piezoelectric and triboelectric nanogenerators for flexible/stretchable and wearable electronics and artificial intelligence. *Advanced Materials* vol. 32, 1902549 (2020).
10. Reddy, C. M., Padmanabhan, K. A. & Desiraju, G. R. Structure–property correlations in bending and brittle organic crystals. *Cryst. Growth Des.* vol. 6, 2720–2731 (2006).
11. Katritzky, A. R. *et al.* Perspective on the relationship between melting points and chemical structure. *Cryst. Growth Des.* vol. 1, 261–265 (2001).
12. Grover, M., Singh, B., Bakshi, M. & Singh, S. Quantitative structure–property relationships in pharmaceutical research – Part 1. *Pharm. sci. technol. today* vol. 3, 28–35 (2000).
13. Damjanovic, D. in *The Science of Hysteresis* (eds Bertotti, G. & Mayergoyz, I. D.) 337–465 (Academic Press, Oxford, 2006).
14. Ishiwara, H. Ferroelectric random access memories. *J. Nanosci. Nanotechnol.* vol. 12, 7619–7627 (2012).

15. Choi, H. S. *et al.* Tailoring the coercive field in ferroelectric metal-free perovskites by hydrogen bonding. *Nat. Commun.* vol. 13 (2022).

16. Webb, J. F. On the physics of ferroelectrics. *Sci. Prog.* vol. 86, 203–234 (2003).

17. Shi, P.-P. *et al.* Symmetry breaking in molecular ferroelectrics. *Chem. Soc. Rev.* vol. 45, 3811–3827 (14 2016).

18. Seyedraoufi, S. & Berland, K. Improved proton-transfer barriers with van der Waals density functionals: Role of repulsive non-local correlation. *J. Chem. Phys.* vol. 156, 244106 (2022).

19. Horiuchi, S., Ishibashi, S. & Tokura, Y. in *Organic ferroelectric materials and applications* (ed Asadi, K.) 47–84 (Woodhead Publishing, 2022).

20. Dypvik Sødahl, E., Seyedraoufi, S., Görbitz, C. H. & Berland, K. Ferroelectric crystals of globular molecules: cambridge structural database mining and computational assessment. *Cryst. Growth Des.* (2023).

21. Groom, C. R., Bruno, I. J., Lightfoot, M. P. & Ward, S. C. The Cambridge Structural Database. *Acta. Crystallogr. B.* vol. 72, 171–179 (2016).

22. Macrae, C. F. *et al. Mercury* 4.0: from visualization to analysis, design and prediction. *J. Appl. Crystallogr.* vol. 53, 226–235 (2020).

23. Bruno, I. J. *et al.* New software for searching the Cambridge Structural Database and visualizing crystal structures. *Acta Crystallogr., Sect. B* vol. 58, 389–397 (2002).

24. Kumai, R. *et al.* Structural assignment of polarization in hydrogen-bonded supramolecular ferroelectrics. *J. Am. Chem. Soc.* vol. 129, 12920–12921 (2007).

25. Horiuchi, S., Kumai, R. & Tokura, Y. A Supramolecular ferroelectric realized by collective proton transfer. *Angew. Chem. Int. Ed.* vol. 46, 3497–3501 (2007).

26. Horiuchi, S., Kumai, R. & Tokura, Y. High-temperature and pressure-induced ferroelectricity in hydrogen-bonded supramolecular crystals of anilic acids and 2,3-di(2-pyridinyl)pyrazine. *J. Am. Chem. Soc.* vol. 135, 4492–4500 (2013).

27. Horiuchi, S., Noda, Y., Hasegawa, T., Kagawa, F. & Ishibashi, S. Correlated proton transfer and ferroelectricity along alternating zwitterionic and nonzwitterionic anthranilic acid molecules. *Chem. Mater.* vol. 27, 6193–6197 (2015).

28. Wang, G. *et al.* Electroceramics for high-energy density capacitors: current status and future perspectives. *Chem. Rev.* vol. 121, 6124–6172 (2021).

29. Fang, B.-J., Ding, C.-L., Liu, W., Li, L.-Q. & Tang, L. Preparation and electrical properties of high-Curie temperature ferroelectrics. *Eur. Phys. J. Appl. Phys.* vol. 45, 20302 (2009).

30. Harada, J. *et al.* Plastic/ferroelectric crystals with easily switchable polarization: low-voltage operation, unprecedentedly high pyroelectric performance, and large piezoelectric effect in polycrystalline forms. *J. Am. Chem. Soc.* vol. 141, 9349–9357 (2019).

31. Harada, J. *et al.* Directionally tunable and mechanically deformable ferroelectric crystals from rotating polar globular ionic molecules. *Nat. Chem.* vol. 8, 946–952 (2016).

32. Sødahl, E. D., Walker, J. & Berland, K. Piezoelectric response of plastic ionic molecular crystals: role of molecular rotation. *Cryst. Growth Des.* vol. 23, 729–740 (2023).

33. Wyrzykowski, D., Kruszyński, R., Kłak, J., Mroziński, J. & Warnke, Z. Structural and magnetic characteristics of tetramethylammonium tetrahalogenoferrates (III). *Inorganica Chim. Acta* vol. 361, 262–268 (2008).

34. Resta, R. & Vanderbilt, D. in *Physics of Ferroelectrics: A Modern Perspective* 31–68 (Springer Berlin Heidelberg, Berlin, Heidelberg, 2007).

35. Spaldin, N. A. A beginner's guide to the modern theory of polarization. *J. Solid State Chem.* vol. 195. Polar inorganic materials: design strategies and functional properties, 2–10 (2012).

36. King-Smith, R. D. & Vanderbilt, D. Theory of polarization of crystalline solids. *Phys. Rev. B* vol. 47, 1651–1654 (1993).

37. Resta, R. Theory of the electric polarization in crystals. *Ferroelectr.* vol. 136, 51–55 (1992).

38. Resta, R. Macroscopic polarization in crystalline dielectrics: the geometric phase approach. *Rev. Mod. Phys.* vol. 66, 899–915 (1994).

39. Tkatchenko, A. & Scheffler, M. Accurate molecular van der Waals interactions from sround-state electron density and free-atom reference data. *Phys. Rev. Lett.* vol. 102, 073005 (7 2009).

40. Grimme, S. Accurate description of van der Waals complexes by density functional theory including empirical corrections. *J. Comput. Chem.* vol. 25, 1463–1473 (2004).

41. Grimme, S. Semiempirical GGA-type density functional constructed with a long-range dispersion correction. *J. Comput. Chem.* vol. 27, 1787–1799 (2006).

42. Grimme, S., Antony, J., Ehrlich, S. & Krieg, H. A consistent and accurate ab initio parametrization of density functional dispersion correction (DFT-D) for the 94 elements H-Pu. *J. Chem. Phys.* vol. 132, 154104 (2010).

43. Grimme, S. Density functional theory with London dispersion corrections. *WIREs Comput. Mol. Sci.* vol. 1, 211–228 (2011).

44. Dion, M., Rydberg, H., Schröder, E., Langreth, D. C. & Lundqvist, B. I. Van der Waals Density Functional for General Geometries. *Phys. Rev. Lett.* vol. 92, 246401 (24 2004).

45. Thonhauser, T. *et al.* Van der Waals density functional: Self-consistent potential and the nature of the van der Waals bond. *Phys. Rev. B* vol. 76 (2007).

46. Berland, K. *et al.* Van der Waals forces in density functional theory: a review of the vdW-DF method. *Rep. Prog. Phys.* vol. 78, 066501 (2015).

47. Chakraborty, D., Berland, K. & Thonhauser, T. Next-generation nonlocal van der Waals density functional. *J. Chem. Theory Comput.* vol. 16. PMID: 32786912, 5893–5911 (2020).

48. Zhang, Y. & Yang, W. Comment on 'Generalized Gradient Approximation made simple'. *Phys. Rev. Lett.* vol. 80, 890–890 (4 1998).

49. Perdew, J. P., Burke, K. & Ernzerhof, M. Generalized Gradient Approximation made simple. *Phys. Rev. Lett.* vol. 77, 3865–3868 (18 1996).

50. Murray, É. D., Lee, K. & Langreth, D. C. Investigation of exchange energy density functional accuracy for interacting molecules. *J. Chem. Theory Comput.* vol. 5, 2754–2762 (2009).

51. Lee, K., Murray, É. D., Kong, L., Lundqvist, B. I. & Langreth, D. C. Higher-accuracy van der Waals density functional. *Phys. Rev. B* vol. 82, 081101 (8 2010).

52. Perdew, J. P. & Yue, W. Accurate and simple density functional for the electronic exchange energy: Generalized gradient approximation. *Phys. Rev. B* vol. 33, 8800–8802 (12 June 1986).

53. Berland, K. & Hyldgaard, P. Exchange functional that tests the robustness of the plasmon description of the van der Waals density functional. *Phys. Rev. B* vol. 89, 035412 (3 Jan. 2014).

54. Hamada, I. Van der Waals density functional made accurate. *Phys. Rev. B* vol. 89, 121103 (12 Mar. 2014).

55. Reilly, A. M. *et al.* Report on the sixth blind test of organic crystal structure prediction methods. *Acta Crystallographica Section B* vol. 72, 439–459 (2016).

56. Day, G. M. in *Supramolecular Chemistry* (John Wiley & Sons, Ltd, 2012).

57. Oganov, A. R., Pickard, C. J., Zhu, Q. & Needs, R. J. Structure prediction drives materials discovery. *Nature Reviews Materials* vol. 4, 331–348 (2019).

58. Bauer, J. *et al. Pharmaceutical Research* vol. 18, 859–866 (2001).

59. Baias, M. *et al.* De novo determination of the crystal structure of a large drug molecule by crystal structure prediction-based powder NMR crystallography. *J. Am. Chem. Soc.* vol. 135, 17501–17507 (2013).

60. Wang, Y., Lv, J., Gao, P. & Ma, Y. Crystal structure prediction via efficient sampling of the potential energy surface. *Accounts of Chemical Research* vol. 55. PMID: 35853142, 2068–2076 (2022).

61. Case, D. H., Campbell, J. E., Bygrave, P. J. & Day, G. M. Convergence properties of crystal structure prediction by quasi-random sampling. *J. Chem. Theory Comput.* vol. 12, 910–924 (2016).

62. Sobol', I. On the distribution of points in a cube and the approximate evaluation of integrals. *USSR Comput. Math. Math. Phys.* vol. 7, 86–112 (1967).

63. Case, D. H., Campbell, J. E., Bygrave, P. J. & Day, G. M. Convergence properties of crystal structure prediction by quasi-random sampling. *J. Chem. Theory Comput.* vol. 12, 910–924 (2016).

64. Becke, A. D. Density-functional thermochemistry. III. The role of exact exchange. *J. Chem. Phys.* vol. 98, 5648–5652 (1993).

65. Yang, S. & Day, G. M. Exploration and optimization in crystal structure prediction: combining basin hopping with quasi-random sampling. *J. Chem. Theory Comput.* vol. 17, 1988–1999 (2021).

66. Price, S. L. *et al.* Modelling organic crystal structures using distributed multipole and polarizability-based model intermolecular potentials. *Phys. Chem. Chem. Phys.* vol. 12, 8478–8490 (30 2010).

67. Williams, D. E. & Cox, S. R. Nonbonded potentials for azahydrocarbons: the importance of the Coulombic interaction. *Acta Crystallogr., Sect. B* vol. 40, 404–417 (1984).

68. Cox, S. R., Hsu, L.-Y. & Williams, D. E. Nonbonded potential function models for crystalline oxohydrocarbons. *Acta Crystallogr., Sect. A* vol. 37, 293–301 (1981).

69. Coombes, D. S., Price, S. L., Willock, D. J. & Leslie, M. Role of electrostatic interactions in determining the crystal structures of polar organic molecules. A distributed multipole study. *The Journal of Physical Chemistry* vol. 100, 7352–7360 (1996).

70. Stone, A. J. Distributed multipole analysis: stability for large basis sets. *Journal of Chemical Theory and Computation* vol. 1, 1128–1132 (2005).

71. Smith, D. G. A. *et al.* PSI4 1.4: Open-source software for high-throughput quantum chemistry. *The Journal of Chemical Physics* vol. 152, 184108 (2020).

72. Valiev, M. *et al.* NWChem: A comprehensive and scalable open-source solution for large scale molecular simulations. *Comput. Phys. Commun.* vol. 181, 1477–1489 (2010).

73. Coombes, D. S., Price, S. L., Willock, D. J. & Leslie, M. Role of electrostatic interactions in determining the crystal structures of polar organic molecules. A distributed multipole study. *J. Phys. Chem.* vol. 100, 7352–7360 (1996).

74. Chisholm, J. A. & Motherwell, S. *COMPACK*: a program for identifying crystal structure similarity using distances. *J. Appl. Crystallogr.* vol. 38, 228–231 (2005).

# Papers

Paper I

# Improved proton-transfer barriers with van der Waals density functionals: Role of repulsive non-local correlation

**Seyedmojtaba Seyedraoufi, Kristian Berland**

Published in *The Journal of Chemical Physics*, 22 June 2022. DOI: 10.1063/5.0095128 and reproduced here with the permission of AIP Publishing.

The Journal of Chemical Physics

# Improved proton-transfer barriers with van der Waals density functionals: Role of repulsive non-local correlation

Cite as: J. Chem. Phys. **156**, 244106 (2022); https://doi.org/10.1063/5.0095128
Submitted: 08 April 2022 • Accepted: 05 June 2022 • Accepted Manuscript Online: 07 June 2022 • Published Online: 22 June 2022

S. Seyedraoufi and Kristian Berland

The Journal of Chemical Physics ARTICLE scitation.org/journal/jcp

# Improved proton-transfer barriers with van der Waals density functionals: Role of repulsive non-local correlation

Cite as: J. Chem. Phys. **156**, 244106 (2022); doi: 10.1063/5.0095128
Submitted: 8 April 2022 • Accepted: 5 June 2022 •
Published Online: 22 June 2022



S. Seyedraoufi and Kristian Berland[a)]

AFFILIATIONS

Department of Mechanical Engineering and Technology Management, Norwegian University of Life Sciences, Ås, Norway

[a)]Author to whom correspondence should be addressed: kristian.berland@nmbu.no

ABSTRACT

Proton-transfer (PT) between organic complexes is a common and important biochemical process. Unfortunately, PT energy barriers are difficult to accurately predict using density functional theory (DFT); in particular, using the generalized gradient approximation (GGA) tends to underestimate PT barriers. Moreover, PT typically occurs in environments where dispersion forces contribute to the cohesion of the system; thus, a suitable exchange-correlation functional should accurately describe both dispersion forces and PT barriers. This paper provides benchmark results for the PT barriers of several density functionals, including several variants of the van der Waals density functional (vdW-DF). The benchmark set comprises small organic molecules with inter- and intra-molecular PT. The results show that replacing GGA correlation with a fully non-local vdW-DF correlation increases the PT barriers, making it closer to the quantum chemical reference values. In contrast, including non-local correlations with the Vydrov-Voorhis method or dispersion-corrections at the DFT-D3 or the Tkatchenko–Scheffler level has barely any impact on the PT barriers. Hybrid functionals also increase and improve the energies, resulting in an excellent performance of hybrid versions of vdW-DF-cx and vdW-DF2-B86R. For the formic acid dimer PT system, we analyzed the GGA exchange and non-local correlation contributions. The analysis shows that the repulsive part of the non-local correlation kernel plays a key role in the PT energy barriers predicted with vdW-DF.



## I. INTRODUCTION

Proton transfer (PT) is a ubiquitous chemical reaction, and many biochemical reactions involve PT. For instance, proton-coupled charge transfer is an established mechanism in enzymology[1] and collective proton transfer in DNA base pairs can give rise to rare tautomers that may lead to mutations.[2] In organic solid-state systems, PT can change the nature of the bonding and, consequently, the properties of a crystal.[3] PT is also one mechanism for electric polarization switching in the organic ferroelectrics.[4–6]

High level quantum chemical methods, in particular, coupled-cluster with single and double and perturbative triple excitations [CCSD(T)] can provide accurate reference data for PT energy barriers, but its high computational cost makes it ill-suited for complex PT systems. The organic complexes in which PT occurs are often held together by van der Waals forces, making it important to assess the accuracy of predicted PT barriers with functionals that include dispersion forces.

Earlier benchmark studies have found that density functional theory (DFT) in the local density approximation (LDA)[7] and generalized-gradient approximation (GGA)[8,9] tend to underestimate PT barriers.[10,11] Hybrid functionals, which mix in a fraction of Fock exchange,[12–15] improve performance[10] which, in part, can be linked to reduced self-interaction error.[16] Patchkovskii and Ziegler[17] found that Perdew–Zunger self-interaction corrected DFT improves reaction and activation energy barriers for 11 selected "difficult" reactions compared to LDA and GGA. Although self-interaction is one source of the PT barrier underestimation, lack of non-local correlation effects has also been suggested as a possible source of inaccuracy.[18]

Several methods, including dispersion forces in DFT, have been developed, but most of these use "dispersion correction" scheme in

which van der Waals forces are reintroduced with atomistic force-field correction.[19–24] One class of functionals[25–34] with a non-local account of the correlation is the Chalmers–Rutgers van der Waals (vdW-DF) density functional,[25,33,35] which is a popular method to describe materials bonded by dispersion forces. vdW-DF is derived from exact criteria using a plasmon-model of the response properties of the electron-gas.[25,29,34–37] In the theory, the non-local correlation energy takes the form

$$E_c^{\mathrm{nl}}[n] = \frac{1}{2}\int d^3\mathbf{r}_1 \int d^3\mathbf{r}_2\, n(\mathbf{r}_1)\,\phi(\mathbf{r}_1,\mathbf{r}_2)\,n(\mathbf{r}_2) \qquad (1)$$

in which a kernel function $\phi(\mathbf{r}_1,\mathbf{r}_2)$ connects two density regions $n(\mathbf{r}_1)$ and $n(\mathbf{r}_2)$. Unlike other dispersion-correction methods, the vdW-DF non-local correlation is designed so that $E_c^{\mathrm{nl}}$ vanishes seamlessly in the homogeneous electron gas limit; moreover, it does rely on explicit short-range cutoff mechanisms. Therefore, vdW-DF does not include gradient components of the GGA correlation in the total exchange-correlation energy, i.e., $E_{xc}[n] = E_x^{\mathrm{GGA}}[n] + E_c^{\mathrm{LDA}}[n] + E_c^{\mathrm{nl}}[n]$. Over the years, several variants of vdW-DF[25–27,29–32,38] have been developed including hybrid variants.[39,40] vdW-DF has also inspired other non-local correlation functionals; in particular, the Vydrov-Voorhis (VV10)[41] functional and its revision for plane wave codes (rVV10).[42] While vdW-DF is foremost developed for describing dispersion-bonded systems, its explicit non-local correlation has also been found to improve various material properties[27,29,36,43] including image plane states on graphene.[44]

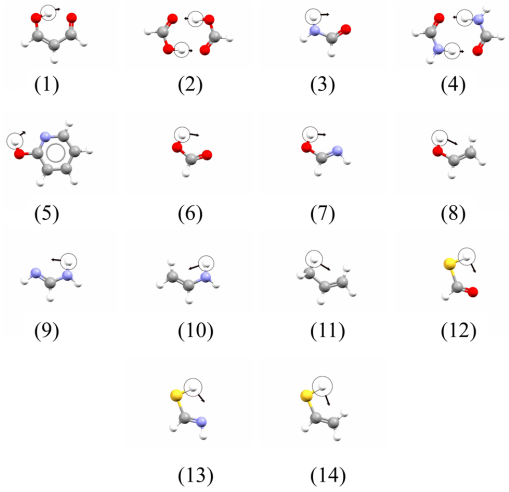


**FIG. 1.** Structures of the PT14 benchmark set. Arrows indicate the direction of proton transfers. Reaction systems comprise (1) malonaldehyde, (2) formic acid dimer, (3) formamide, (4) formamide dimer, (5) pyridine, and nine tautomerization reactions, including [(6)–(8)] carbonyls, [(9) and (10)] imines, (11) propene, and [(12) and (14)] thiocarbonyls. Color scheme: O (red), C (gray), H (white), N (blue), S (yellow).

This paper provides benchmark results for 22 functionals including several vdW-DFs. We based the benchmark set labeled PT14 on the 9 charge-neutral intra-molecular PT systems by Karton *et al.*[45] and 5 inter- and intra-molecular PT systems by Mangiatordi *et al.*[10] computed with coupled-cluster method at the CCSD(T) level of theory. The set of systems is displayed in Fig. 1. We also tested several GGAs,[46,47] two standard hybrid functionals,[14,15] and the strongly constrained and appropriately normed (SCAN) meta-GGA functional.[48] In addition to vdW-DF, we also tested the rVV10[41,42] and the SCAN-rVV10 functional.[49] Moreover, we investigated the effect of adding force-field dispersion corrections at the D3[22] and Tkatchenko–Scheffler (TS)[19] level of theory to some GGAs and the B3LYP[15] hybrid functional.

We found that vdW-DF tends to increase PT barriers compared to GGA and, therefore, reduce the deviation with the reference data. The results are detailed in Sec. III. This trend is caused by the reduction in the negative correlation contribution to the PT barriers. To gain better understanding of this result, we performed an in-depth analysis of the formic acid dimer system (system 2 in Fig. 1), as detailed in Sec. IV. The non-local correlation contribution was found to be dominated by repulsive short-range non-local correlation effects. This effect is similar to that of GGA-type correlation but with the local geometry-sensitivity inherited to vdW-DF.

## II. METHODS

The benchmark calculations were carried out with the VASP software package,[50–52] except for the vdW-DF3-opt1, vdW-DF3-opt2,[32] and B3LYP(-D3)[15] calculations for which QUANTUM ESPRESSO[53] was used, as these functionals have not been implemented in VASP. The geometries were fixed to the ones from Mangiatordi *et al.*[10] and Karton *et al.*[45] that were obtained at CCSD and B3LYP level of theories, respectively. In the supercells, 15 Å vacuum padding was used to isolate the molecular systems employing the dipole correction scheme of Neugebauer and Scheffler.[54] The electronic self-consistency criteria was set to $10^{-6}$ eV. Based on our pseudopotential choices and convergence study, as detailed in Sec. II A, the plane wave energy cutoffs were set to 1000 eV. The VASP calculations used hard projected augmented waves (PAW) pseudopotentials (PPs), while the QUANTUM ESPRESSO used the SG15 optimized norm-conserving Vanderbilt (SG15 ONCV).[55–57] For the exchange and correlation analysis, we obtained the input data from the PPACF post-processing tool[58] that is distributed with the QUANTUM ESPRESSO software package.

### A. Pseudopotential choice and convergence

In the energy cutoff convergence study and PP selection, we compared the ultra-soft Rappe–Rabe–Kaxiras–Joannopoulos (RRKJUS) pseudopotential[59] obtained from the PSlibrary project database,[60] with the hard norm-conserving PP Hartwigsen–Goedecker–Hutter (HGH),[61] and the SG15 ONCV as well as the standard and hard PAW PP[62,63] as implemented in VASP.

Figure 2 displays the results for the case of PT barriers of the formic acid dimer. It shows that while ONCV, HGH, and hard PAW converge to a similar value of 0.12 eV, this value differs from the converged value of the ultrasoft RRKJUS and standard PAW, by 0.07 and 0.03 eV, respectively. In comparison, the literature

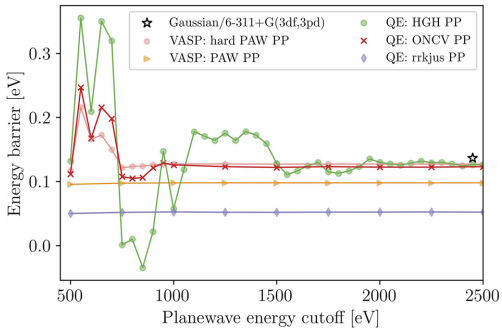


**FIG. 2.** PT energy barrier sensitivity of the formic acid dimer to plane wave energy cutoff for different PPs. The black star indicates the energy barrier of Mangiatordi *et al.*[10] study using a 6-311+G(3df, 3pd) orbital basis.

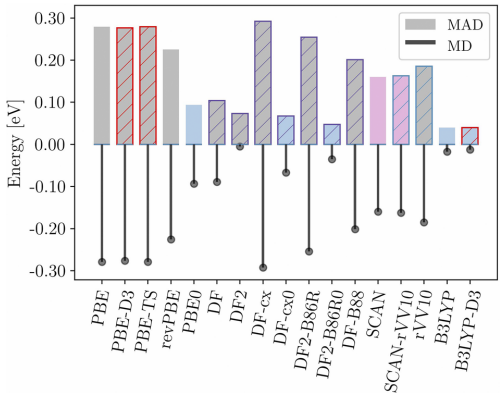


**FIG. 3.** Mean (absolute) deviation [M(A)D] of PT energy barriers for the PT14 benchmarking set. The reference values are provided at CCSD(T) level.[10] The bar colors indicate the nature of the respective exchange functionals, with GGAs indicated in gray, hybrids in blue, and meta-GGAs in pink. Stripes indicate the inclusion of dispersion forces, either with a dispersion correction (red stripes), or using full non-local correlation within vdW-DF (indigo) or at the rVV10 (light blue) level. "vdW-" prefix dropped for simplicity in functional names.

value obtained with 6-311+G(3df, 3pd) orbital basis set using the GAUSSIAN program package[64] is 0.13 eV.[10] The similarity of the ONCV, HGH, and hard PAW results demonstrates the reliability of these PPs. Our results are in line with the fact that ONCV has been shown to perform well compared to all-electron results for a selected set of solids, including covalent, ionic, and metallic bonding.[55] In contrast to ONCV and hard PW, which converge smoothly to within 1 meV at 1000 eV, the PT barriers obtained with HGH fluctuates significantly with the cutoff until the energy differences fall within 1 meV at an energy cutoff of 2800 eV.[65]

## III. RESULTS

Figure 3 displays computed statistical data for PT energy barriers for the PT14 set for a subset of the benchmarked functionals. The full set of results are provided in Table I. It shows that the two pure GGAs, revPBE[47] and PBE,[46] (indicated by plain gray bars) significantly underestimate the PT barriers. For systems with low PT barriers, results can be qualitatively incorrect. For instance, in the case of the malonaldehyde (system 1 in Fig. 1), PBE predicts 8 meV, which is far less than the reference value of 168 meV. PBE0, which mixes in 25% Fock exchange with the PBE exchange,[14] improves the PT barriers. The meta-GGA SCAN is overall more accurate than PBE, but less accurate than PBE0. Despite that dispersion forces contribute to hydrogen bonding, adding dispersion corrections at the DFT-D3[22] or at the TS[19] level has barely any impact on the predicted PT barrier. Interestingly, a similar insensitivity is also exhibited when adding rVV10 non-local correlation corrections to SCAN.[49] In contrast, several vdW-DFs, in particular, vdW-DF[25] and vdW-DF2[26] have significantly smaller deviations from the reference than the GGAs. The most accurate non-hybrid functional is vdW-DF2 with a mean absolute deviation (MAD) of 0.073 eV, a mere quarter of the PBE MAD of 0.279 eV. In comparison, the MAD of PBE0 is 0.094 eV. The reduced deviation of vdW-DF can be traced to the GGA gradient correlations having a larger negative contribution to the barrier than the fully non-local vdW-DF correlation. For instance, in going from revPBE to vdW-DF, which keeps the exchange fixed, the MAD drops from 0.226 to 0.104 eV. The hybrid variant of vdW-DF-cx and vdW-DF2-B86R that mix 25% Fock exchange to the GGA exchange (vdW-DF-cx0[39,40] and vdW-DF2-B86R0) predict PT barriers with a MAD of 0.067 and 0.047 eV, respectively. Finally, we note that the empirical B3LYP functional,[15] which uses 20% Fock exchange and a reduced GGA correlation (0.81 LYP[66]) provides slightly more accurate PT barriers with a MAD of 0.040 eV.

Figure 4 shows the individual correlation components for eight different functionals for the PT barrier of the formic acid dimer. It shows how the non-local correlation contribution of vdW-DF reduces the PT barrier less than the GGA correlation, thus making vdW-DF and vdW-DF2 the most accurate functionals for this PT barrier. As noted before, the comparison is most clear-cut when comparing revPBE and vdW-DF as the exchange is kept fixed. The D3 correction in PBE-D3 and the rVV10 non-local correlation contribution in SCAN-rVV10 are barely visible.

## IV. ANALYSIS OF ENERGETIC CONTRIBUTIONS OF VDW-DF

The dramatically improved performance of vdW-DF and vdW-DF2 compared to the GGAs, and the good performance of hybrid vdW-DF-cx and vdW-DF2-B86R prompted us to perform an analysis of the mechanisms involved in the improved PT barriers. We retain the double-PT formic acid dimer (system 2 in Fig. 1) as a case study.

### A. Exchange contribution

The degree of underestimation with GGAs as well as the performance of individual vdW-DF variants depends on the specific exchange functional used. Jenkins *et al.*[68] recently highlighted how the *s*-resolved gradient component of the exchange energy can be a useful tool to analyze why the choice of exchange enhancement

**TABLE I.** PT energy barriers, mean absolute deviations (MAD), mean deviations (MD), mean absolute relative deviation (MARD), and mean relative deviations (MRD) for the PT14 benchmarking set for different density functionals. The units are in electron volts (eV).

| Systems | Ref. | PBE | PBE-D3 | PBE-TS | revPBE | PBE0 | SCAN | SCAN-rVV10 | rVV10 | B3LYP | B3LYP-D3 | PBEsol |
|---|---|---|---|---|---|---|---|---|---|---|---|---|
| 1 | 0.168 | 0.008 | 0.015 | 0.009 | 0.049 | 0.073 | 0.038 | 0.036 | 0.073 | 0.130 | 0.144 | −0.079 |
| 2 | 0.343 | 0.127 | 0.130 | 0.130 | 0.211 | 0.207 | 0.160 | 0.155 | 0.208 | 0.289 | 0.289 | −0.029 |
| 3 | 2.028 | 1.814 | 1.818 | 1.813 | 1.865 | 1.999 | 1.950 | 1.948 | 1.925 | 2.080 | 2.087 | 1.692 |
| 4 | 0.828 | 0.655 | 0.657 | 0.650 | 0.762 | 0.755 | 0.707 | 0.699 | 0.780 | 0.885 | 0.886 | 0.451 |
| 5 | 1.650 | 1.328 | 1.326 | 1.324 | 1.369 | 1.540 | 1.472 | 1.471 | 1.406 | 1.589 | 1.587 | 1.228 |
| 6 | 1.594 | 1.347 | 1.352 | 1.348 | 1.391 | 1.536 | 1.446 | 1.445 | 1.434 | 1.597 | 1.606 | 1.242 |
| 7 | 1.570 | 1.271 | 1.272 | 1.271 | 1.319 | 1.467 | 1.408 | 1.406 | 1.348 | 1.520 | 1.521 | 1.163 |
| 8 | 2.643 | 2.254 | 2.255 | 2.254 | 2.287 | 2.495 | 2.408 | 2.406 | 2.351 | 2.559 | 2.562 | 2.152 |
| 9 | 2.061 | 1.778 | 1.778 | 1.776 | 1.832 | 1.973 | 1.925 | 1.923 | 1.881 | 2.046 | 2.045 | 1.654 |
| 10 | 2.848 | 2.509 | 2.510 | 2.508 | 2.544 | 2.741 | 2.673 | 2.670 | 2.625 | 2.818 | 2.820 | 2.403 |
| 11 | 3.523 | 3.144 | 3.144 | 3.147 | 3.174 | 3.472 | 3.370 | 3.368 | 3.224 | 3.524 | 3.523 | 3.060 |
| 12 | 1.388 | 1.171 | 1.178 | 1.172 | 1.237 | 1.338 | 1.265 | 1.262 | 1.270 | 1.435 | 1.448 | 1.037 |
| 13 | 1.256 | 0.987 | 0.991 | 0.986 | 1.052 | 1.158 | 1.089 | 1.087 | 1.078 | 1.248 | 1.254 | 0.854 |
| 14 | 2.55 | 2.150 | 2.156 | 2.152 | 2.200 | 2.387 | 2.298 | 2.295 | 2.251 | 2.487 | 2.498 | 2.025 |
| MD | ⋯ | −0.279 | −0.276 | −0.279 | −0.225 | −0.094 | −0.160 | −0.163 | −0.185 | −0.017 | −0.013 | −0.399 |
| MAD | ⋯ | 0.279 | 0.276 | 0.279 | 0.225 | 0.094 | 0.160 | 0.163 | 0.185 | 0.040 | 0.040 | 0.399 |
| MRD (%) | ⋯ | −24.8 | −24.3 | −24.8 | −18.3 | −11.2 | −16.9 | −17.3 | −15.4 | −2.8 | −2.0 | −38.3 |
| MARD (%) | ⋯ | 24.8 | 24.3 | 24.8 | 18.3 | 11.2 | 16.9 | 17.3 | 15.4 | 4.7 | 4.2 | 38.3 |

| Systems | Ref. | DF | DF2 | DF-cx | DF-cx0 | DF-cx0-20 | DF2-B86R | DF2-B86R0 | DF2-B86R0-20 | DF-optB88 | DF-optPBE | DF3-opt1 | DF3-opt2 |
|---|---|---|---|---|---|---|---|---|---|---|---|---|---|
| 1 | 0.168 | 0.131 | 0.188 | −0.014 | 0.076 | 0.058 | 0.016 | 0.101 | 0.084 | 0.042 | 0.068 | −0.028 | 0.005 |
| 2 | 0.343 | 0.336 | 0.409 | 0.091 | 0.212 | 0.188 | 0.135 | 0.252 | 0.229 | 0.173 | 0.225 | 0.054 | 0.114 |
| 3 | 2.028 | 2.003 | 2.088 | 1.803 | 2.028 | 1.983 | 1.850 | 2.064 | 2.022 | 1.893 | 1.918 | 1.787 | 1.833 |
| 4 | 0.828 | 0.930 | 1.032 | 0.614 | 0.768 | 0.737 | 0.686 | 0.832 | 0.803 | 0.723 | 0.788 | 0.574 | 0.657 |
| 5 | 1.650 | 1.501 | 1.571 | 1.328 | 1.573 | 1.526 | 1.354 | 1.590 | 1.544 | 1.406 | 1.427 | 1.305 | 1.344 |
| 6 | 1.594 | 1.514 | 1.588 | 1.337 | 1.561 | 1.517 | 1.371 | 1.584 | 1.110 | 1.418 | 1.438 | 1.317 | 1.358 |
| 7 | 1.570 | 1.446 | 1.517 | 1.261 | 1.494 | 1.449 | 1.283 | 1.508 | 1.464 | 1.344 | 1.366 | 1.232 | 1.270 |
| 8 | 2.643 | 2.425 | 2.523 | 2.244 | 2.525 | 2.470 | 2.282 | 2.552 | 2.500 | 2.345 | 2.351 | 2.232 | 2.268 |
| 9 | 2.061 | 1.973 | 2.057 | 1.766 | 2.002 | 1.956 | 1.803 | 2.031 | 1.987 | 1.860 | 1.885 | 1.744 | 1.787 |
| 10 | 2.848 | 2.679 | 2.782 | 2.495 | 2.768 | 2.715 | 2.547 | 2.808 | 2.757 | 2.599 | 2.605 | 2.495 | 2.531 |
| 11 | 3.523 | 3.301 | 3.382 | 3.145 | 3.508 | 3.436 | 3.183 | 3.549 | 3.477 | 3.237 | 3.237 | 3.147 | 3.172 |
| 12 | 1.388 | 1.391 | 1.476 | 1.164 | 1.374 | 1.332 | 1.201 | 1.404 | 1.364 | 1.261 | 1.289 | 1.132 | 1.181 |
| 13 | 1.256 | 1.209 | 1.297 | 0.980 | 1.195 | 1.153 | 1.006 | 1.217 | 1.175 | 1.079 | 1.108 | 0.941 | 0.988 |
| 14 | 2.55 | 2.361 | 2.471 | 2.140 | 2.425 | 2.368 | 2.173 | 2.462 | 2.406 | 2.253 | 2.268 | 2.110 | 2.154 |
| MD | ⋯ | −0.089 | −0.005 | −0.292 | −0.067 | −0.111 | −0.254 | −0.035 | −0.078 | −0.201 | −0.177 | −0.315 | −0.271 |
| MAD | ⋯ | 0.104 | 0.073 | 0.292 | 0.067 | 0.111 | 0.254 | 0.047 | 0.078 | 0.201 | 0.177 | 0.315 | 0.271 |
| MRD (%) | ⋯ | −5.0 | 3.3 | −27.2 | −9.5 | −12.9 | −23.0 | −5.9 | −9.3 | −18.3 | −14.7 | −29.8 | −24.8 |
| MARD (%) | ⋯ | 6.8 | 6.5 | 27.2 | 9.5 | 12.9 | 23.0 | 6.6 | 9.3 | 18.3 | 14.7 | 29.8 | 24.8 |

factor $F_x(s)$ causes the performance of different vdW-DFs to differ for different types of systems. The GGA exchange itself is expressed as modulation of the LDA exchange, as follows:

$$E_x^{\mathrm{GGA}}[n] = \int d^3r\, n(\mathbf{r})\, \epsilon_x^{\mathrm{LDA}}(n(\mathbf{r}))\, F_x(s), \tag{2}$$

with the reduced density gradient given by $s(\mathbf{r}) = |\nabla n(\mathbf{r})|/2(3\pi^2)^{1/3} n(\mathbf{r})^{4/3}$. In turn, the $s$-resolved gradient component of the exchange energy is given by

$$e_x(s) = \int d^3r\, n(\mathbf{r})\, \epsilon_x^{\mathrm{LDA}}(n(\mathbf{r}))\, [F_x(s) - 1]\, \delta(s - s(\mathbf{r})). \tag{3}$$

The contribution to the PT energy is given by the difference between the transition state (ts) and ground state (gs) as follows:

$$\Delta e_x(s) = e_x^{\mathrm{ts}}(s) - e_x^{\mathrm{gs}}(s). \tag{4}$$

The $s$-integrated exchange energy density is given by

$$\Delta E_x(s) = \int_0^s \Delta e_x(s')\, ds'. \tag{5}$$

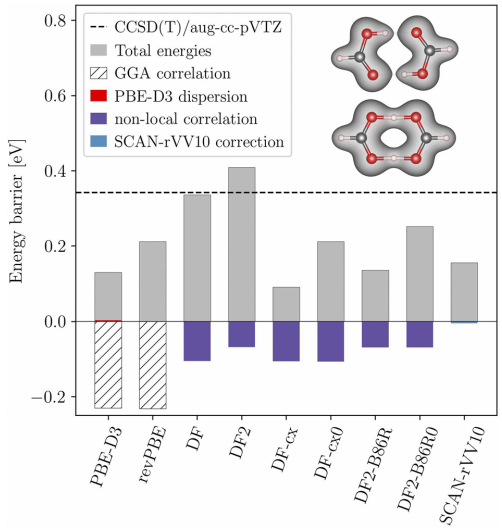


**FIG. 4.** PT barrier energies of different functionals and their correlation components for the formic acid dimer. The quantum chemical reference indicated with the dashed line.[10] The inset shows the density isosurfaces in the ground and transition state. The contributions of GGA correlation, non-local correlation with rVV10 and vdW-DF, and D3 corrections are indicated. The visualization in the inset and elsewhere is generated with VESTA.[67]

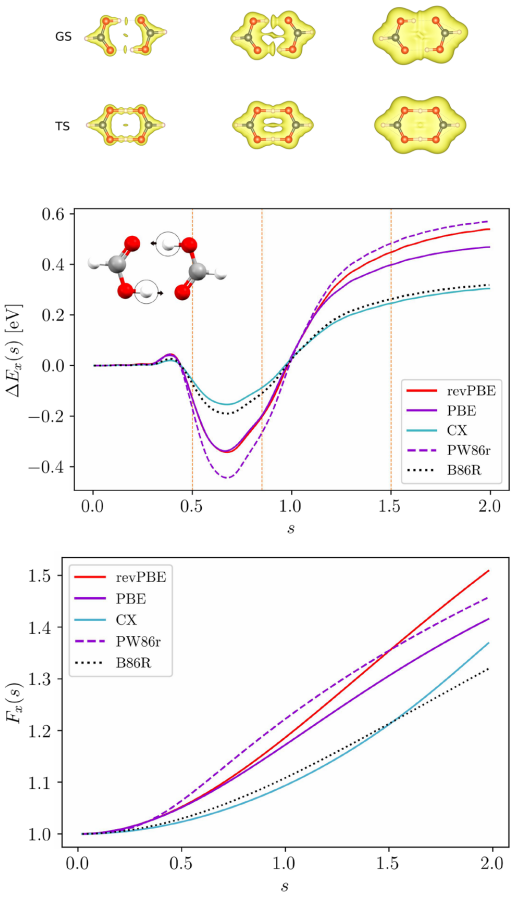


**FIG. 5.** $s$-isosurfaces for three different s values are shown for the ground state (gs) and transition state (ts) in the upper panel and marked with yellow vertical lines in the middle panel. $s$-integrated exchange barrier [$\Delta E_x(s)$] of the formic acid dimer for different selected exchange functionals (middle panel) and corresponding enhancement factors (lower panel) are plotted as a function of s.

Numerically, we computed Eq. (5) using the Savitzky–Golay[69] filter fitted with a third-degree polynomial to remove the noise effects due to grid-point integration and then take the derivative to obtain Eq. (4).

The result is shown in Fig. 5. The upper panel shows plotted $s$-isosurfaces for the transition and ground states for the three different s values. The middle panel shows the $s$-integrated exchange energy barriers [Eq. (5)] for selected exchange functionals. The vertical dashed lines indicate the displayed isosurfaces in the upper panel. The lower panel shows corresponding exchange enhancement factors, $F_x(s)$. We can roughly discriminate two main s regions: $0.4 < s < 0.75$, which reduces the PT barrier, and $s > 0.75$, which increases the barrier. Considering that exchange energies are always negative, the s regime with negative exchange contribution to the PT barrier correlates with larger s isosurface areas at the transition state. In the regions beyond $s \approx 0.6$, the situation is reversed, and exchange energies are contributing positively to the barrier. This can be linked to the larger isosurface areas of the ground state. The $s = 0.85$ isosurfaces exemplifies this: the two isosurfaces of the individual dimers have completely merged for the transition state causing smaller surface areas, while the ground state is in the process of merging, corresponding to large surface areas. At $s \approx 1.5$, both isosurfaces enclose the full molecular dimer systems, which can be related to the flattening out of the positive exchange contribution curve, as the isosurfaces effectively cancel out each other as they become more similar. Moreover, there is also a reduction in the total exchange contribution due to the lower electronic density in the large s regions. Note that this analysis only takes the explicit non self-consistent energetic contributions of Eq. (3) into account, and small corrections would arise at the self-consistent level.

The effect of the role of the enhancement factors $F_x(s)$ can be understood by considering $F_x(s) - 1$ as modulations of the exchange contribution curves. Comparing revPBE to PBE exchange, we can trace the larger PT barrier of the former to the increasing difference between the values of $F_x(s)$ as s increases, and that most of the difference comes from regions with $s > 1.0$. It is also interesting that vdW-DF and vdW-DF2 end up with quite similar energies,

even though the exchange functionals, revPBE and PW86r, differ considerably in shape. This result is related to a partial cancellation of positive and negative exchange contributions to the PT barrier. Comparing $F_x(s)$ with $\Delta E_x(s)$ reveals that the larger value of the PW86r $F_x(s)$ coincides with a larger slope of $\Delta E_x(s)$ in most of the negatively and positively-contributing s regions (top panel). The final difference also partially cancels with the small difference in non-local correlation contributions. With a MAD of 0.254 eV, vdW-DF2-B86R performs more accurately than vdW-DF-cx with a MAD of 0.292 eV. This result can be related both to the slightly smaller exchange contribution to the PT energy barrier (Fig. 5) and larger negative non-local correlation contribution of vdW-DF-cx comparing to vdW-DF2-B86R (Fig. 4).

Table I shows that, while several vdW-DFs perform better than GGAs, not all vdW-DFs are equally accurate. For instance, PBE performs better than the recently developed vdW-DF3 variants and vdW-DF-cx. However this is not due to the non-local correlation, but rather their "soft" exchange functionals, i.e., the $F_x(s)$ shape has overall lower values. In fact, truly "soft" GGAs such as PBEsol[70] are even less accurate with a MAD of 0.4 eV. The "soft" form in the small-to-medium $s$-regime is crucial for making vdW-DF accurate for broad classes of systems, including solids and layered systems.[29,32,35,71] Thus, even though this study shows that vdW-DF and vdW-DF2 are accurate for PT systems, the original vdW-DF notoriously overestimates binding separations for all kinds of systems. While vdW-DF2 can be quite accurate for molecular dimers and molecular crystals and has a broader range of applicability, it severely overestimates lattice constants of solids and layered systems, as well as adsorption on coinage metals.[29]

### B. Analysis of the role of non-local correlation

For analyzing the non-local correlation of vdW-DF, the local responsivity $q_0(\mathbf{r})$ is the most natural variable as it enters into the non-local correlation kernel $\phi(\mathbf{r}_1, \mathbf{r}_2) = \phi(D, \delta)$ through dimensionless parameters $\delta$ and $D$. In Sec. IV C, we will also project non-local correlation density onto $s(\mathbf{r})$, for sake of comparison with GGA exchange and correlation. The parameter $\delta$ is the relative difference in responsivity $q_0(\mathbf{r})$ (inverse length scale) of two density regions

$$\delta = \frac{|q_0(\mathbf{r}_1) - q_0(\mathbf{r}_2)|}{q_0(\mathbf{r}_1) + q_0(\mathbf{r}_2)}, \tag{6}$$

and the effective dimensionless separation $D$ is given by

$$D = \frac{1}{2}(q_0(\mathbf{r}_1) + q_0(\mathbf{r}_2))|\mathbf{r}_1 - \mathbf{r}_2|. \tag{7}$$

The parameter $q_0(\mathbf{r})$ is, within vdW-DF, given by

$$q_0(\mathbf{r}) = \left(\frac{\epsilon_c^{\mathrm{LDA}}}{\epsilon_x^{\mathrm{LDA}}} + 1 - \frac{Z_{\mathrm{ab}}}{9} s(\mathbf{r})^2\right) k_{\mathrm{F}}(\mathbf{r}), \tag{8}$$

where $k_{\mathrm{F}}(\mathbf{r})$ is the local Fermi vector. $Z_{\mathrm{ab}}$ is equal to −0.849 for vdW-DF1 and vdW-DF3-opt1 and −1.887 for vdW-DF2 and vdW-DF3-opt2. The spatial non-local correlation density is given by

$$e_c^{\mathrm{nl}}(\mathbf{r}) = \frac{n(\mathbf{r})}{2} \int d^3\mathbf{r}'\, n(\mathbf{r}')\, \phi(\mathbf{r}, \mathbf{r}'), \tag{9}$$

and, subsequently, the $q_0$-resolved non-local correlation can be defined as

$$e_c^{\mathrm{nl}}(q_0) = \int d^3 r\, e_c^{\mathrm{nl}}(\mathbf{r})\, \delta(q_0 - q_0(\mathbf{r})). \tag{10}$$

The $q_0$-resolved non-local correlation contribution to the PT barrier is then given as

$$\Delta e_c^{\mathrm{nl}}(q_0) = e_c^{\mathrm{nl,\,ts}}(q_0) - e_c^{\mathrm{nl,\,gs}}(q_0), \tag{11}$$

and the corresponding $q_0$-integrated non-local correlation barrier is

$$\Delta E_c^{\mathrm{nl}}(q_0) = \int_0^{q_0} \Delta e_c^{\mathrm{nl}}(q_0')\, dq_0'. \tag{12}$$

For the analysis of the non-local correlation contributions to PT barriers, Fig. 6 shows four interlinked panels. Panel (a) shows three selected $q_0$ isosurfaces for the ground state (gs) and transition state (ts). The overlaid contours indicate the non-local correlation density as given by Eq. (9). The three isosurfaces ($q_0 \approx 1.2$, 1.8, and 2.2) were selected based on the curves for $q_0$-resolved non-local correlation [as given by Eq. (10)] of the ground and transition states provided in panel (c), with the difference provided in panel (d). The rulers indicate the $D = 3$ separation, as well the real-space distance $|\mathbf{r}_1 - \mathbf{r}_2|$ of 2 a.u. bohrs. Panel (b) shows the vdW-DF kernel. The upper left isosurface of panel (a) for $q_0 \approx 1.2$ coincides with fairly low density regions, except for the regions directly between hydrogens and its oxygen neighbor in the adjacent molecule. Thus, this positive contribution to the non-local correlation of the ground state causes a lowering of the PT barrier. The larger blue isosurfaces around the void in between the two molecules for the transition state also contribute somewhat to lowering the PT barrier. This contribution can be viewed as a long-range dispersion effect as the distance from one to the other end of the void coincides with $D \approx 3$, i.e., the minimum of the kernel (b). The isosurfaces corresponding to $q_0 \approx 1.8$ [mid panels (a)] show additional lobes around the hydrogen atoms in the transition state, while the ground state isosurface has been disconnected. These isosurface differences explain the increase in the positive non-local correlation energy of the transition state increasing the magnitude of the PT barrier. Finally, the upper right isosurface corresponds to $q_0 = 2.2$ in which the isosurface lobes around the hydrogen in the transition state has vanished, but the isosurfaces around the hydrogen in the ground state cause a significant reduction of the PT barrier. At this value of $q_0$, the effective separation $D$ has contracted significantly causing intra-molecular correlation to be dominating contribution.

### C. Reduced-gradient resolved correlation comparison

Subsection IV B highlighted the utility of analyzing vdW-DF in terms of the spatial distribution of $q_0(\mathbf{r})$ which enters into the kernel $\phi(D, \delta)$ of vdW-DF. In GGA correlation,[46] a key variable is the reduced gradient $t = |\nabla n(\mathbf{r})|/2k_s(\mathbf{r})n(\mathbf{r})$, which is defined using the Thomas-Fermi screening length $k_s = \sqrt{4k_{\mathrm{F}}/\pi}$. In terms of $t$, the total PBE correlation energy can be expressed as

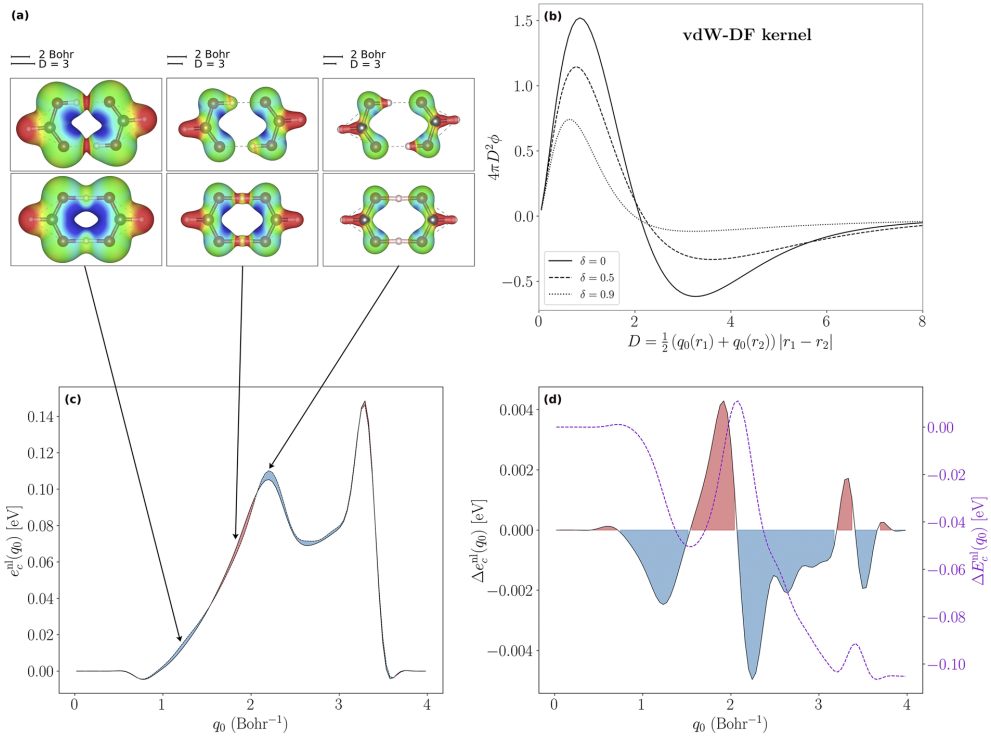


**FIG. 6.** Non-local correlation contributions to the double PT transfer energy in formic acid: (a) $q_0$-isosurfaces with $q_0 \approx 1.2$, 1.8, and 2.2 a.u. overlaid by non-local correlation density $e_c^{nl}(\mathbf{r})$ [Eq. (9)]. Red indicates negative contributions and blue positive. The upper rulers indicate real-space distances of 2 bohrs (i.e., 2 a.u.) 2 bohrs ≈ 1.06 Å, and the lower unit-less scaled lengths of $D = 3$ entering into the vdW-DF kernel,[25] depicted for reference in panel (b). Panel (c) shows the total non-local correlation [Eq. (10)] of the ground and the transition state. Blue shading indicates negative net contributions to the PT barrier and red indicates net positive contributions. Panel (d) shows the corresponding $q_0$-resolved contributions to the PT barrier while the dashed curve shows the integrated contributions.

$$E_c^{\mathrm{PBE}} = \int d^3r\, n(\mathbf{r})\,[\epsilon_c^{\mathrm{LDA}}(\mathbf{r}) + H(n(\mathbf{r}), t(\mathbf{r}))], \tag{13}$$

where $H$ is the gradient contribution function. In order to analyze the effect of correlation and exchange on an equal footing, whether at the GGA or vdW-DF level, we benefit from resolving these quantities onto the same variable. We here choose the reduced gradient s which was used for exchange in Fig. 5. The corresponding $s$-resolved gradient component of PBE correlation energy is given by

$$e_c^{\mathrm{PBE}}(s) = \int d^3r\, n(\mathbf{r})\, H(r, t(s))\, \delta(s - s(\mathbf{r})), \tag{14}$$

with the corresponding integrated quantity given by

$$\Delta E_c^{\mathrm{PBE}}(s) = \int_0^s \Delta e_c^{\mathrm{PBE}}(s')\, ds'. \tag{15}$$

The projection of vdW-DF onto s is similar to Eq. (10).

Figure 7 shows the PT energy barrier contributions of $\Delta E_c^{\mathrm{PBE}}(s)$ and non-local correlations. Vertical dashed lines correspond to the isosurfaces in the upper panel of Fig. 5. Comparing the curves with those of the exchange contributions in Fig. 5 shows that the curves bear some resemblance, but they have opposite prefactor and earlier onset of correlation contribution than exchange with increasing $s$. Comparing GGA and the vdW-DF and vdW-DF2 correlations shows that while the shapes are similar, the former has much larger positive and negative contributions beyond $s \approx 0.4$. Comparing with the $s$-isosurfaces reveals that this s value corresponds to the onset of connected isosurfaces for the transition state geometry. Thus, the smaller vdW-DF correlation coincides with a transition from purely intra-molecular correlation to inter–molecular correlation contributions. In the regions below $s \approx 0.6$, the differential PBE and non-local correlations are contributing positively to the barrier $[\Delta e_c(s) > 0]$, which can be traced to the larger s surface area at the transition state. This situation is reversed for the regions beyond $s \approx 0.6$. We also

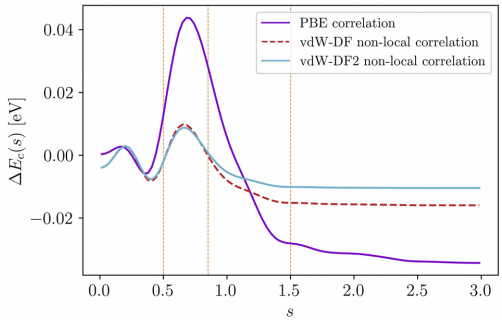


**FIG. 7.** *s*-resolved gradient component of the PBE correlation, vdW-DF non-local correlation and vdW-DF2 non-local correlation contributions to the PT barrier are plotted as a function of s for formic acid dimer.

found that for $s > 1$ values corresponds to isosurfaces that enclose the entire dimer systems, similar to the low $q_0$ values. Moreover, beyond $s \approx 1.5$, vdW-DF correlation flattens, while the magnitude of GGA correlation continues to grow. In these regions, the two isosurfaces have merged, resulting in similar isosurface shapes for both the transition and ground states. Finally, we note that the earlier flattening of the vdW-DF2 compared to vdW-DF1 curves can be related to the larger $Z_{ab}$ value of vdW-DF2[35] which causes a larger $q_0$ values in the low-density large s regime.[72]

## V. CONCLUSIONS AND OUTLOOK

We have compared and analyzed the performance of different functionals for proton-transfer energy barriers and found that replacing GGA correlation with vdW-DF non-local correlation causes a non-intuitive increase of the energy barriers. This increase typically improves accuracy compared to GGA, which tends to underestimate energy barriers. Use of hybrid exchange also improves barriers, and good performance was found for hybrid versions of two van der Waals density functionals vdW-DF-cx0 and vdW-DF2-B86R0, though B3LYP and B3LYP-D3 were slightly more accurate.

The improved PT transfer barriers of vdW-DF are highly encouraging because these functionals can also account for the dispersion forces that are important for the cohesion of many proton-transfer systems. Beyond this, our study points to the possibility that the usage of a non-local kernel reflects a true geometry-sensitive repulsive short-range correlation contribution. In this context, we emphasize that while vdW-DF was designed with dispersion forces in mind, the theory is rooted in exact constraints and many-body theory and, therefore, is not limited to long range dispersion forces as such. vdW-DF is a true non-local correlation functional with contributions both at short and long ranges. At the same time, the performance of approximate exchange-correlation functionals are generally contingent on the various simplifications and parameterizations used in their construction. The improved performance may also be a mostly "fortuitous" effect arising due to typically smaller semi-local correlation-type effects in vdW-DF. Exploring this question merits further theoretical and computational investigations and may pave the way for more accurate methods using non-local functionals for improving chemical reaction energies.

## ACKNOWLEDGMENTS

The computations of this work were carried out on UNINETT Sigma2 high performance computing resources (Grant No. NN9650K). This work was supported by the Research Council of Norway as a part of the Young Research Talent project FOX (Grant No. 302362). We thank Rasmus Tranås and Elin Dypvik Sødahl for comments. K.B. acknowledges discussions with T. Jenkins and T. Thonhauser on visualization.

## AUTHOR DECLARATIONS

### Conflict of Interest

The authors have no conflicts to disclose.

### Author Contributions

**S. Seyedraoufi:** Investigation (equal); Software (equal); Visualization (equal); Writing-original-draft (equal); Writing-review-editing (equal). **Kristian Berland:** Conceptualization (equal); Formal analysis (equal); Funding acquisition (equal); Investigation (equal); Project administration (equal); Supervision (equal); Visualization (equal); Writing-original-draft (equal); Writing-review-editing (equal).

## DATA AVAILABILITY

The data that support the findings of this study are available within the article and from the corresponding author upon reasonable request.

## REFERENCES

[1] S. Y. Reece and D. G. Nocera, "Proton-coupled electron transfer in biology: Results from synergistic studies in natural and model systems," Annu. Rev. Biochem. **78**, 673–699 (2009).

[2] D. Jacquemin, J. Zúñiga, A. Requena, and J. P. Céron-Carrasco, "Assessing the importance of proton transfer reactions in DNA," Acc. Chem. Res. **47**, 2467–2474 (2014).

[3] J. S. Stevens, S. J. Byard, C. C. Seaton, G. Sadiq, R. J. Davey, and S. L. M. Schroeder, "Proton transfer and hydrogen bonding in the organic solid state: A combined XRD/XPS/ssNMR study of 17 organic acid–base complexes," Phys. Chem. Chem. Phys. **16**, 1150–1160 (2014).

[4] S. Horiuchi, S. Ishibashi, and Y. Tokura, "3 - hydrogen-bonded organic molecular ferroelectrics/antiferroelectrics," in *Organic Ferroelectric Materials and Applications, Woodhead Publishing Series in Electronic and Optical Materials*, edited by K. Asadi (Woodhead Publishing, 2022), pp. 47–84.

[5] S. Horiuchi, Y. Tokunaga, G. Giovannetti, S. Picozzi, H. Itoh, R. Shimano, R. Kumai, and Y. Tokura, "Above-room-temperature ferroelectricity in a single-component molecular crystal," Nature **463**, 789–792 (2010).

[6]S. Horiuchi, K. Kobayashi, R. Kumai, and S. Ishibashi, "Proton tautomerism for strong polarization switching," Nat. Commun. **8**, 14426 (2017).
[7]W. Kohn and L. J. Sham, "Self-consistent equations including exchange and correlation effects," Phys. Rev. **140**, A1133–A1138 (1965).
[8]J. P. Perdew, "Density-functional approximation for the correlation energy of the inhomogeneous electron gas," Phys. Rev. B **33**, 8822–8824 (1986).
[9]A. D. Becke, "Density-functional exchange-energy approximation with correct asymptotic behavior," Phys. Rev. A **38**, 3098–3100 (1988).
[10]G. F. Mangiatordi, E. Brémond, and C. Adamo, "DFT and proton transfer reactions: A benchmark study on structure and kinetics," J. Chem. Theory Comput. **8**, 3082–3088 (2012).
[11]V. Barone, L. Orlandini, and C. Adamo, "Proton transfer in model hydrogen-bonded systems by a density functional approach," Chem. Phys. Lett. **231**, 295–300 (1994).
[12]A. D. Becke, "A new mixing of Hartree–Fock and local density-functional theories," J. Chem. Phys. **98**, 1372–1377 (1993).
[13]A. Pribram-Jones, D. A. Gross, and K. Burke, "DFT: A theory full of holes?," Annu. Rev. Phys. Chem. **66**, 283–304 (2015).
[14]C. Adamo and V. Barone, "Toward reliable density functional methods without adjustable parameters: The PBE0 model," J. Chem. Phys. **110**, 6158–6170 (1999).
[15]A. D. Becke, "Density-functional thermochemistry. III. The role of exact exchange," J. Chem. Phys. **98**, 5648–5652 (1993).
[16]J. L. Bao, L. Gagliardi, and D. G. Truhlar, "Self-interaction error in density functional theory: An appraisal," J. Phys. Chem. Lett. **9**, 2353–2358 (2018).
[17]S. Patchkovskii and T. Ziegler, "Improving "difficult" reaction barriers with self-interaction corrected density functional theory," J. Chem. Phys. **116**, 7806–7813 (2002).
[18]T. Tsuneda and K. Hirao, "Self-interaction corrections in density functional theory," J. Chem. Phys. **140**, 18A513 (2014).
[19]A. Tkatchenko and M. Scheffler, "Accurate molecular van der Waals interactions from ground-state electron density and free-atom reference data," Phys. Rev. Lett. **102**, 073005 (2009).
[20]S. Grimme, "Accurate description of van der Waals complexes by density functional theory including empirical corrections," J. Comput. Chem. **25**, 1463–1473 (2004).
[21]S. Grimme, "Semiempirical GGA-type density functional constructed with a long-range dispersion correction," J. Comput. Chem. **27**, 1787–1799 (2006).
[22]S. Grimme, J. Antony, S. Ehrlich, and H. Krieg, "A consistent and accurate *ab initio* parametrization of density functional dispersion correction (DFT-D) for the 94 elements H-Pu," J. Chem. Phys. **132**, 154104 (2010).
[23]S. Grimme, "Density functional theory with London dispersion corrections," Wiley Interdiscip. Rev.: Comput. Mol. Sci. **1**, 211–228 (2011).
[24]M. Stöhr, T. Van Voorhis, and A. Tkatchenko, "Theory and practice of modeling van der Waals interactions in electronic-structure calculations," Chem. Soc. Rev. **48**, 4118–4154 (2019).
[25]M. Dion, H. Rydberg, E. Schröder, D. C. Langreth, and B. I. Lundqvist, "van der Waals density functional for general geometries," Phys. Rev. Lett. **92**, 246401 (2004).
[26]K. Lee, É. D. Murray, L. Kong, B. I. Lundqvist, and D. C. Langreth, "Higher-accuracy van der Waals density functional," Phys. Rev. B **82**, 081101 (2010).
[27]I. Hamada, "van der Waals density functional made accurate," Phys. Rev. B **89**, 121103(R) (2014).
[28]K. Berland and P. Hyldgaard, "Exchange functional that tests the robustness of the plasmon description of the van der Waals density functional," Phys. Rev. B **89**, 035412 (2014).
[29]K. Berland, C. A. Arter, V. R. Cooper, K. Lee, B. I. Lundqvist, E. Schröder, T. Thonhauser, and P. Hyldgaard, "van der Waals density functionals built upon the electron-gas tradition: Facing the challenge of competing interactions," J. Chem. Phys. **140**, 18A539 (2014).
[30]J. Klimeš, D. R. Bowler, and A. Michaelides, "Chemical accuracy for the van der Waals density functional," J. Phys.: Condens. Matter. **22**, 022201 (2009).
[31]J. Klimeš, D. R. Bowler, and A. Michaelides, "Van der Waals density functionals applied to solids," Phys. Rev. B **83**, 195131 (2011).
[32]D. Chakraborty, K. Berland, and T. Thonhauser, "Next-generation nonlocal van der Waals density functional," J. Chem. Theory Comput. **16**, 5893–5911 (2020).
[33]T. Thonhauser, V. R. Cooper, L. Shen, A. Puzder, P. Hyldgaard, and D. C. Langreth, "Van der Waals density functional: Self-consistent potential and the nature of the van der Waals bond," Phys. Rev. B **76**, 125112 (2007).
[34]E. Schröder, V. R. Cooper, K. Berland, B. I. Lundqvist, P. Hyldgaard, and T. Thonhauser, "The vdW-DF family of nonlocal exchange-correlation functionals," in *Non-Covalent Interactions in Quantum Chemistry and Physics* (Elsevier, 2017), pp. 241–274.
[35]K. Berland, V. R. Cooper, K. Lee, E. Schröder, T. Thonhauser, P. Hyldgaard, and B. I. Lundqvist, "van der Waals forces in density functional theory: A review of the vdW-DF method," Rep. Prog. Phys. **78**, 066501 (2015).
[36]P. Hyldgaard, Y. Jiao, and V. Shukla, "Screening nature of the van der Waals density functional method: A review and analysis of the many-body physics foundation," J. Phys.: Condens. Matter. **32**, 393001 (2020).
[37]P. Hyldgaard, K. Berland, and E. Schröder, "Interpretation of van der Waals density functionals," Phys. Rev. B **90**, 075148 (2014).
[38]K. Berland, D. Chakraborty, and T. Thonhauser, "van der Waals density functional with corrected $C_6$ coefficients," Phys. Rev. B **99**, 195418 (2019).
[39]K. Berland, Y. Jiao, J.-H. Lee, T. Rangel, J. B. Neaton, and P. Hyldgaard, "Assessment of two hybrid van der Waals density functionals for covalent and non-covalent binding of molecules," J. Chem. Phys. **146**, 234106 (2017).
[40]Y. Jiao, E. Schröder, and P. Hyldgaard, "Extent of Fock-exchange mixing for a hybrid van der Waals density functional?," J. Chem. Phys. **148**, 194115 (2018).
[41]O. A. Vydrov and T. Van Voorhis, "Nonlocal van der Waals density functional: The simpler the better," J. Chem. Phys. **133**, 244103 (2010).
[42]R. Sabatini, T. Gorni, and S. de Gironcoli, "Nonlocal van der Waals density functional made simple and efficient," Phys. Rev. B **87**, 041108 (2013).
[43]O. D. Lindroth and P. Erhart, "Thermal transport in van der Waals solids from first-principles calculations," Phys. Rev. B **94**, 115205 (2016).
[44]I. Hamada, Y. Hamamoto, and Y. Morikawa, "Image potential states from the van der Waals density functional," J. Chem. Phys. **147**, 044708 (2017).
[45]A. Karton, R. J. O'Reilly, and L. Radom, "Assessment of theoretical procedures for calculating barrier heights for a diverse set of water-catalyzed proton-transfer reactions," J. Phys. Chem. A **116**, 4211–4221 (2012).
[46]J. P. Perdew, K. Burke, and M. Ernzerhof, "Generalized gradient approximation made simple," Phys. Rev. Lett. **77**, 3865–3868 (1996).
[47]Y. Zhang and W. Yang, "Comment on "generalized gradient approximation made simple"," Phys. Rev. Lett. **80**, 890 (1998).
[48]J. Sun, A. Ruzsinszky, and J. P. Perdew, "Strongly constrained and appropriately normed semilocal density functional," Phys. Rev. Lett. **115**, 036402 (2015).
[49]H. Peng, Z.-H. Yang, J. P. Perdew, and J. Sun, "Versatile van der Waals density functional based on a meta-generalized gradient approximation," Phys. Rev. X **6**, 041005 (2016).
[50]G. Kresse and J. Hafner, "*Ab initio* molecular dynamics for liquid metals," Phys. Rev. B **47**, 558–561 (1993).
[51]G. Kresse and J. Furthmüller, "Efficiency of ab-initio total energy calculations for metals and semiconductors using a plane-wave basis set," Comput. Mater. Sci. **6**, 15–50 (1996).
[52]G. Kresse and J. Furthmüller, "Efficient iterative schemes for *ab initio* total-energy calculations using a plane-wave basis set," Phys. Rev. B **54**, 11169–11186 (1996).
[53]P. Giannozzi *et al.*, "Advanced capabilities for materials modelling with Quantum ESPRESSO," J. Phys.: Condens. Matter. **29**, 465901 (2017).
[54]J. Neugebauer and M. Scheffler, "Adsorbate-substrate and adsorbate-adsorbate interactions of Na and K adlayers on Al(111)," Phys. Rev. B **46**, 16067–16080 (1992).
[55]D. R. Hamann, "Optimized norm-conserving Vanderbilt pseudopotentials," Phys. Rev. B **88**, 085117 (2013).
[56]M. Schlipf and F. Gygi, "Optimization algorithm for the generation of ONCV pseudopotentials," Comput. Phys. Commun. **196**, 36–44 (2015).

[57]P. Scherpelz, M. Govoni, I. Hamada, and G. Galli, "Implementation and validation of fully relativistic GW calculations: Spin–orbit coupling in molecules, nanocrystals, and solids," J. Chem. Theory Comput. **12**, 3523–3544 (2016).
[58]J. Yang, E. Schröder, and P. Hyldgaard, "Signatures of van der Waals binding: A coupling-constant scaling analysis," Phys. Rev. B **97**, 085115 (2018).
[59]A. M. Rappe, K. M. Rabe, E. Kaxiras, and J. D. Joannopoulos, "Optimized pseudopotentials," Phys. Rev. B **41**, 1227–1230 (1990).
[60]A. Dal Corso, "Pseudopotentials periodic table: From H to Pu," Comput. Mater. Sci. **95**, 337–350 (2014).
[61]S. Goedecker, M. Teter, and J. Hutter, "Separable dual-space Gaussian pseudopotentials," Phys. Rev. B **54**, 1703–1710 (1996).
[62]P. E. Blöchl, "Projector augmented-wave method," Phys. Rev. B **50**, 17953–17979 (1994).
[63]G. Kresse and D. Joubert, "From ultrasoft pseudopotentials to the projector augmented-wave method," Phys. Rev. B **59**, 1758–1775 (1999).
[64]M. Frisch *et al.*, Gaussian 09 Revision a02 (Gaussian, Inc., Wallingford, CT, 2009).
[65]M. Verstraete and X. Gonze, "First-principles calculation of the electronic, dielectric, and dynamical properties of $CaF_2$," Phys. Rev. B **68**, 195123 (2003).
[66]C. Lee, W. Yang, and R. G. Parr, "Development of the Colle-Salvetti correlation-energy formula into a functional of the electron density," Phys. Rev. B **37**, 785–789 (1988).
[67]K. Momma and F. Izumi, "*VESTA* 3 for three-dimensional visualization of crystal, volumetric and morphology data," J. Appl. Crystallogr. **44**, 1272–1276 (2011).
[68]T. Jenkins, K. Berland, and T. Thonhauser, "Reduced-gradient analysis of van der Waals complexes," Electron. Struct. **3**, 034009 (2021).
[69]A. Savitzky and M. J. E. Golay, "Smoothing and differentiation of data by simplified least squares procedures," Anal. Chem. **36**, 1627–1639 (1964).
[70]G. I. Csonka *et al.*, "Assessing the performance of recent density functionals for bulk solids," Phys. Rev. B **79**, 155107 (2009).
[71]F. Tran, L. Kalantari, B. Traoré, X. Rocquefelte, and P. Blaha, "Nonlocal van der Waals functionals for solids: Choosing an appropriate one," Phys. Rev. Mater. **3**, 063602 (2019).
[72]K. Berland and P. Hyldgaard, "Analysis of van der Waals density functional components: Binding and corrugation of benzene and $C_{60}$ on boron nitride and graphene," Phys. Rev. B **87**, 205421 (2013).

Paper II

# Database mining and first-principles assessment of organic proton-transfer ferroelectrics

**Seyedmojtaba Seyedraoufi, Elin Dypvik Sødahl, Carl Henrik Görbitz, Kristian Berland**

Submitted for publication

II

# Database mining and first-principles assessment of organic proton-transfer ferroelectrics

Seyedmojtaba Seyedraoufi,[1] Elin Dypvik Sødahl,[1] Carl Henrik Görbitz,[2] and Kristian Berland[1]

[1]*Department of Mechanical Engineering and Technology Management, Norwegian University of Life Sciences, 1432 Ås, Norway.*
[2]*Department of Chemistry, University of Oslo, 0371 Oslo, Norway.*

(Dated: January 19, 2024)

In organic proton-transfer ferroelectrics (OPTFe), molecules are linked to form hydrogen-bonded networks, and proton transfer (PT) between molecules is the dominant mechanism of ferroelectric switching. The fast-switching frequencies of OPTFes make them attractive alternatives to conventional ceramic ferroelectrics, which contain rare and/or toxic elements and require high processing temperatures. In this study, we mined the Cambridge Structural Database (CSD) for potential OPTFes, uncovering most of the previously reported materials, both tautomeric compounds and acid-base salts, in addition to seven new potential OPTFes. Five of these were tautomeric salts, opening up a new avenue for engineering novel OPTFes. The CSD mining was based on identifying polar crystal structures with pseudo-inversion symmetry and viable PT paths. The spontaneous polarization, $\boldsymbol{P}_\mathrm{s}$, and the PT barriers, $U_\mathrm{PT}$, were calculated using density functional theory.

## I. INTRODUCTION

Organic ferroelectrics have several potential advantages over traditional ceramic ferroelectrics, including biocompatibility, printability, low weight, and flexibility.[1–4] These properties make organic ferroelectrics a promising class of materials for applications in wearable electronics.[5] Among these materials, organic ferroelectric polymers, such as polyvinylidene fluoride (PVDF), find use in various industries, including energy harvesting.[6] However, a key limitation of polymers is their high coercive fields ($E_\mathrm{c}$)[1], the minimum electric field to switch the direction of $\boldsymbol{P}_\mathrm{s}$, which limits their applicability in low-voltage electronics.[7] Organic proton-transfer ferroelectrics (OPTFe), on the other hand, are characterized by low $E_\mathrm{c}$ (on average $\sim 10\,\mathrm{kV/cm}$)[2] and fast ferroelectric switching.[8,9] Several mechanisms can give rise to ferroelectricity in molecular crystals, including those incorporating hydrogen bonds. Ferroelectrics are thus generally divided into two groups, depending on whether switching is caused by a reorientation of static dipoles (order-disorder) or through a displacement of atomic species (displacive).[10] For instance, in molecular plastic crystals, the polarization direction generally switches with a rotational reorientation of the molecular species and the ferroelectric-to-paraelectric phase transition involves molecular rotational disorder.[11]

In OPTFes, the polarization reversal is largely due to proton transfer (PT) between molecular neighbors in infinite hydrogen-bonded networks. In some cases, the switching also involves a reorientation of molecules, such as for the ionic molecular crystals of diazabicyclo[2.2.2]octane cations and tetrahedral inorganic anions.[8,10,12] So far, the largest reported $|\boldsymbol{P}_\mathrm{s}|$ among the OPTFes stands at $\sim 30\ \mu\mathrm{C/cm}^2$ for croconic acid.[1,9] In comparison, PVDF has a measured value of $\sim 7\ \mu\mathrm{C/cm}^2$.[13] Croconic acid is, however, corrosive, which can be problematic for device applications. Susceptibility to oxidation in the air is another liability for some tautomeric ferroelectrics with $\mathrm{OH}\cdots\mathrm{O}$ hydrogen bonds.[14] Thus, it is important to identify broader types of OPTFes, for instance, tautomeric ferroelectrics with imidazole or pyrazole rings are not corrosive and are less prone to oxidation.[14,15] Acid-base salts constitute another type of OPTFes and typically have lower $E_\mathrm{c}$ and $\boldsymbol{P}_\mathrm{s}$ than the tautomeric ones.[10] While there have been a number of experimental investigations, computational studies of OPTFes are scarce. Lee et al. used density functional theory (DFT) to study PT barriers ($U_\mathrm{PT}$) of the phenazine-chloranilic acid salt.[16] More recently, Ishibashi et al.[17] showed that the vdW-DF method[18,19] can successfully predict lattice parameters and $\boldsymbol{P}_\mathrm{s}$ for a set of tautomeric OPTFes. In this paper, we present a systematic mining and screening study of all entries in the Cambridge Structural Database[20] (CSD) to identify new potential OPTFes. An important part of the screening procedure relies on identifying structures characterized by pseudo-inversion symmetry. Pseudosymmetry refers to the concept where a structure can be viewed as a higher symmetry structure that has undergone minor asymmetric distortions. The idea of finding ferroelectric materials through pseudosymmetry detection has been proposed and explored in previous studies: Capillas et al.[21] suggested a procedure to detect pseudosymmetry by searching through the minimal supergroups of the material's space group. This method was applied to approximately 300 entries deposited in the Inorganic Crystal Structure Database in search of ferroelectrics with displacive mechanism[22]. Abrahams[23] exploited the same idea to detect new inorganic ferroelectrics. However, these studies have only examined a limited number of structures, fewer than 400. To our knowledge, no extensive screening of the CSD database has been conducted to identify potential OPTFe structures. Since PT transfer is the key mechanism of ferroelectric switching in OPTFe, demanding pseudo-inversion symmetry is an effective screening criterion; however, the criteria can miss compounds that experience significant distor-

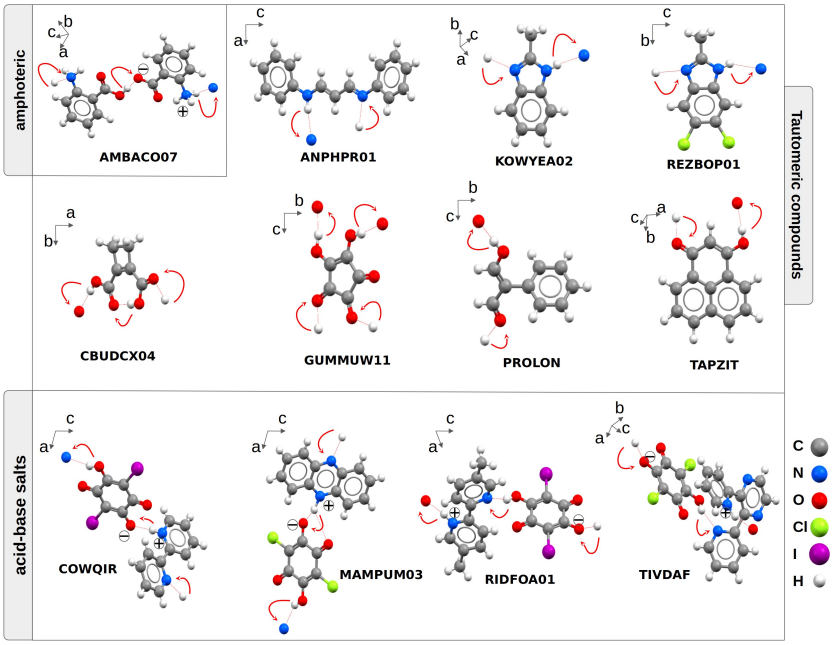


FIG. 1: OPTFes structures used in this study. Curved arrows indicate the direction of site-to-site PT. COWRAK (not shown) has a structure similar to RIDFOA01, but Br is replaced by I. Likewise, TIVFEL (not shown) is similar to TIVDAF, but with Br replaced by Cl.

tion during the PT switching. For the systems identified in our screening, $\boldsymbol{P}_\mathrm{s}$ and $U_\mathrm{PT}$ were computed using DFT. In addition, we computed these properties for a benchmark set of 14 compounds that were previously reported as OPTFes. This served to determine which DFT functionals accurately predict lattice constants and to establish a linear correlation between measured $E_\mathrm{c}$ and computed $U_\mathrm{PT}$, in order to obtain a rough estimate of the $E_\mathrm{c}$ of the identified compounds.

## II. METHODS

### A. CSD Searching approach

In our screening study, we only included structures with a polar space group, which is a prerequisite for ferroelectricity,[24] and limited our investigation to organic non-polymeric structures with less than 1000 atoms in the unit cell. We also demanded atomic coordinates and the absence of structural disorder. To ensure the reliability of atomic positions in structures, entries with an R-factor $\leq 0.075$ were included, indicating a good agreement between the refined and observed X-ray data. The criteria were implemented using the CSD 2023.2 database and CSD Python API 3.0.16[25]. To identify the approximate pseudo-inversion symmetry, the PT paths, and to set up structures for computing the $\boldsymbol{P}_\mathrm{s}$, we extended the functionality of MOLCRYS Python package,[26] which is based on the Atomic Simulation Environment (ASE)[27] and NETWORKX.[28] These steps involve making an inverted image of the crystal structure, followed by a translation to overlay the original and inverted image to minimize the mean absolute deviation of the atomic separations between equivalent atoms. For pseudosymmetric molecular crystals supporting PT, this procedure yields a nearly identical structure, except for the protons involved in the PT, which end up as "isolated protons" in the middle of hydrogen bonds. To filter out structures that do not support PT, we used a mean-distance threshold of 0.25 Å between the original image and the inverted one; thus accommodating some degree of distortion, yet allowing a straightforward superposition of atomic positions of the structure and its inverse. Once structures with pseudo-inversion symmetry with isolated protons had been identified, we inspected the individual crystal structures to identify a clear sequence of PT pathways that generate infinite chains, as opposed to intramolecular PT or intermolecular PT within unconnected supramolecular complexes.

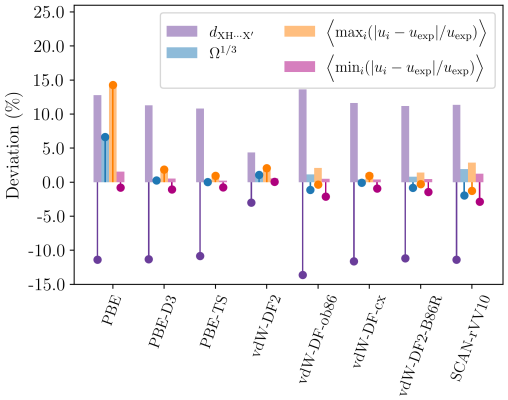


FIG. 2: Mean absolute relative deviation of hydrogen-bond distances $d_{\mathrm{XH\cdots X'}}$, third root of the volumes $\Omega^{1/3}$, and mean of the largest and smallest absolute relative deviation of lattice constants ($u_i$) are depicted in light-color bars. The dark-color bars represent corresponding relative (not absolute) deviations.

### B. Density functional theory calculations

The DFT calculations were performed with the projector augmented wave (PAW) method implemented in the VASP software package[29–31] using hard PAW pseudopotentials. The plane-wave cutoff was set to 1200 eV, based on our earlier work on $U_{\mathrm{PT}}$ of molecular dimers.[32] A high cut-off and hard pseudopotentials were also necessary to converge the lattice parameters for the OPTFes systems. The self-consistent loop was iterated until the energy change was $< 10^{-8}$ eV. The Brillouin zone was sampled with a Γ-centered Monkhorst-Pack grid with a minimum spacing of $(1/25)$ Å$^{-1}$. This converged the lattice constants of croconic acid, which has the smallest unit cell volume in the OPTFe dataset, to within 0.01 Å. Lattice parameters and atomic positions were relaxed until the norm of all atomic forces was $< 0.01$ eV/Å. The $\boldsymbol{P}_{\mathrm{s}}$ values were computed using the Berry-phase method.[33–35] The climbing image nudged elastic band method[36] was used to identify the intermolecular PT transition states in the acid-base salts. For tautomeric compounds, however, the molecular states with both protons transferred onto one molecule were in general unstable. The single PT barrier ($U_{\mathrm{PT}}^{\mathrm{sgl}}$) for these compounds was consequently not computed. For the collective PT barrier ($U_{\mathrm{PT}}^{\mathrm{col}}$), the transition state was approximated using the same interpolated image used to identify the pseudo-inversion symmetry, followed by a single-point DFT evaluation.

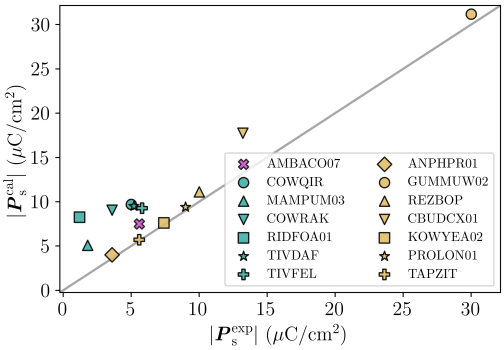


FIG. 3: Computed versus experimental $\boldsymbol{P}_{\mathrm{s}}$ for the OPTFes dataset.

## III. RESULTS AND DISCUSSION

### A. Benchmarking of lattice constants

A total of 7 low-temperature, previously reported OPTFe structures in the CSD, including 4 tautomers and 3 acid-base salts, were selected to define a benchmark dataset for the comparison of experimental and computed values. In this paper, we identify individual CSD entries by their refcodes. The structures used in this benchmark set are GUMMUW11, REZBOP01, CBUDCX04, PROLON, COWQIR, MAMPUM03, COWRAK, and are shown in Fig. 1. The corresponding chemical abbreviations are listed in Tab. I and Tab. II. For each compound, lattice parameters and hydrogen bond distances were computed using several exchange-correlation functionals. Lattice parameters can be sensitive to the choice of exchange-correlation functional, in particular for vdW-bonded systems.[37–39] Fig. 2 shows the deviation in lattice parameters for different functionals compared to the experimentally reported values of the benchmark set. Among the vdW-DF density functionals, vdW-DF-cx[40] has the best agreement with the experimental lattice constants, as also found in the study of Ishibashi et al,[17] and Sødahl et al.[41] The rest of vdW-DF, including vdW-DF2[42] also provide accurate lattice parameters. In contrast, PBE[43] overestimates and SCAN-rVV10[44] significantly underestimates lattice constants. PBE-D3[45] and PBE-TS[46], which use atom-centered dispersion correction, both provide accurate lattice parameters. In an earlier study, we found that the use of non-local correlation at the vdW-DF level greatly improved $U_{\mathrm{PT}}$ values for a set of molecular dimers and that vdW-DF2, in particular, provided accurate $U_{\mathrm{PT}}$ values.[32] Thus, we adopted vdW-DF2. In addition to the lattice vectors, we have also computed the three distances associated with hydrogen bonds: XH $\cdots$ X′, X-H, and X $\cdots$ X′ for the OPTFe

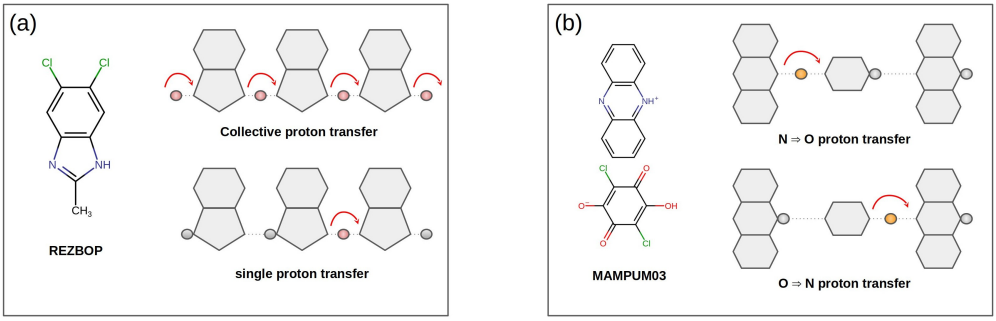


FIG. 4: (a) A schematic illustration of collective PT versus single PT shown for tautomeric compounds. The example system is DC-MBI (REZBOP). (b) Two possible single PTs are illustrated for acid-base salts. The example system is Phz-H2ca (MAMPUM03).

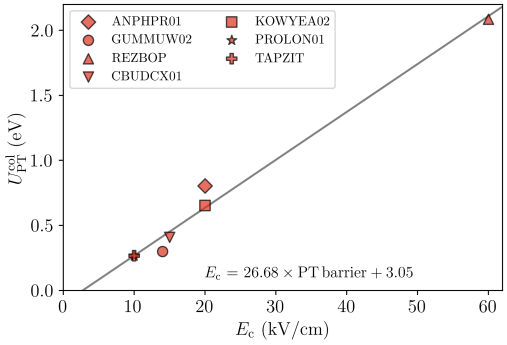


FIG. 5: $U_{\mathrm{PT}}^{\mathrm{col}}$ is plotted against the $E_c$ for the tautomeric OPTFes.

dataset. The mean absolute deviation (MAD) and mean deviation (MD) of XH $\cdots$ X′, which is averaged across all systems in the dataset, is illustrated in Fig. 2. The results show that vdW-DF2-computed distances agree well with the experimentally reported distances. However, the independent atom model,[47] a commonly used method to refine crystal structures from X-ray diffraction data, tends to underestimate the X-H bond lengths. Thus, it is hard to make a definite assessment of the XH $\cdots$ X′ bond lengths.[48] One could also expect this underestimation to be smaller in the case of bonds that host PT. Nonetheless, we decided to include a comparison of these bond lengths computed with different methods to stimulate further investigations in this direction.

### B. Computed spontaneous polarizations and PT barriers

$\boldsymbol{P}_{\mathrm{s}}$ and $U_{\mathrm{PT}}$ were computed for a set of 14 OPTFe compounds in the CSD, comprising seven tautomers (ANPHPR01, GUMMUW02, REZBOP, CBUDCX01, KOWYEA02, PROLON01, TAPZIT), one amphoteric compound (AMBACO07), and six acid-base salts (COWQIR, MAMPUM03, COWRAK, RIDFOA01, TIVDAF, and TIVFEL). The structures are shown in Fig. 1. In the amphoteric compound AMBACO07, the hydrogen-bonded one-dimensional network of zwitterionic and neutral anthranilic acid molecules enables ferroelectric switching.[49] Among the tautomeric structures, PT occurs between different moieties, as shown in Fig. 1. In the ANPHPR01, KOWYEA02, and REZBOP crystals, the PT involves imine-enamine tautomerism. In CBUDCX01, the transfer occurs between carboxylic acid groups (HO-C=O), and PROLON01 and TAPZIT have HO-C=C-C=O moieties. Croconic acid (GUMMUW02) has a similar moiety, but double PT occurs through a three-dimensional hydrogen-bonded network.[1,9,14,50] The acid-base salts are all composed of halogenated anilic acid derivatives combined with either bipyridine (COWQIR), phenazine (MAMPUM03), dimethyl-bipyridine (RIDFOA01) or pyridine-pyrazine (TIVDAF) derivatives.[51–54] Fig. 3 plots the computed against the reported experimental $\boldsymbol{P}_{\mathrm{s}}$ values, which are also listed in Tab. I and Tab. II. For tautomeric compounds, the computed values agree within a range of 10% with the experimental values. However, for salts, the computed values on average overestimate the experimental values by a factor of three. Kagawa et al.[55] reported that domains can be strongly pinned in OPTFe acid-base salts, causing a discrepancy between computed and experimental values. In their case, with additional thermal annealing, the $|\boldsymbol{P}_{\mathrm{s}}|$ of 6,6′-dimethyl-2,2′-bipyridinium chloranilate, an OPTFe salt, increased from 1.3 $\mu$C/cm$^2$ to 7 $\mu$C/cm$^2$.

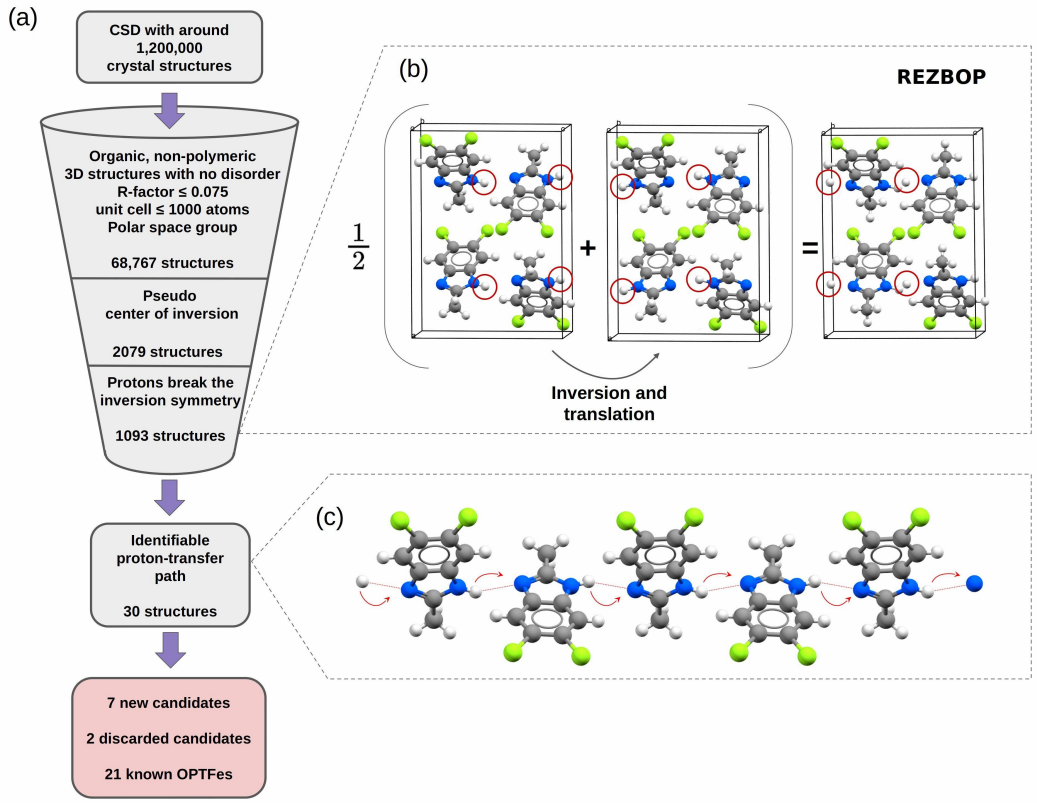


FIG. 6: (a) The workflow of the CSD mining. (b) Schematic illustration of combing a crystal structure with its inverted image for the case of DC-MBI (CSD refcode: REZBOP), which is an OPTFe. The transferrable protons are marked with red circles. (c) The PT (hydrogen bond) paths are marked with red arrows.

TABLE I: PT energy barriers, and ferroelectric properties of reported acid-base salt OPTFes: $|\boldsymbol{P}_{\rm s}^{\rm exp}|$ and $|\boldsymbol{P}_{\rm s}^{\rm cal}|$ are the magnitudes of the experimental and computed $\boldsymbol{P}_{\rm s}$ ($\mu$C/cm$^2$), respectively. $T_{\rm C}$ is the Curie temperature. $U_{\rm PT}^{\rm col}$ is collective PT per proton and $U_{\rm PT}^{\rm sgl}$ is single PT energies.

| CSD refcode | $T_{\rm C}$ (K) | $\lvert\boldsymbol{P}_{\rm s}^{\rm exp}\rvert$ | $\lvert\boldsymbol{P}_{\rm s}^{\rm cal}\rvert$ | $U_{\rm PT,O\to N}^{\rm sgl}$ (eV) | $U_{\rm PT,N\to O}^{\rm sgl}$ (eV) | $U_{\rm PT}^{\rm col}$ (eV) | Space group | Chemical abbreviation |
|---|---|---|---|---|---|---|---|---|
| COWQIR | 158 | 5.0 | 9.71 | 0.19 | 0.33 | 0.40 | $P1$ | H22bpy-Hia[51] |
| MAMPUM03 | 253 | 1.8 | 5.09 | 0.44 | 0.19 | 0.55 | $P2_1$ | Phz-H2ca[52] |
| COWRAK | 259 | 3.6 | 9.06 | 0.07 | 0.21 | 0.40 | $P1$ | H55dmbp-Hba[51] |
| RIDFOA01 | 268 | 1.2 | 8.26 | 0.14 | 0.34 | 0.32 | $P1$ | H55dmbp-Hia[53] |
| TIVDAF | 402 | 5.2 | 9.50 | 0.16 | 0.30 | 0.52 | $Cc$ | Hdppz-Hca[54] |
| TIVFEL | 420 | 5.8 | 9.26 | 0.17 | 0.31 | 0.48 | $Cc$ | Hdppz-Hba[54] |

The difference between the single and collective PT is schematically illustrated in Fig. 4**(a)** for the tautomeric compound REZBOP. The values of $U_{\rm PT}^{\rm col}$ are given per proton, but the full collective PT would scale with the number of protons involved. Nonetheless, a significantly lower $U_{\rm PT}^{\rm col}$ than $U_{\rm PT}^{\rm sgl}$ indicates that the PT has some degree of collectivity. For the acid-base salts, there are two types of molecules, and, as a result, a single PT can occur in two distinct ways: either from nitrogen to oxygen or from oxygen to nitrogen, as depicted in

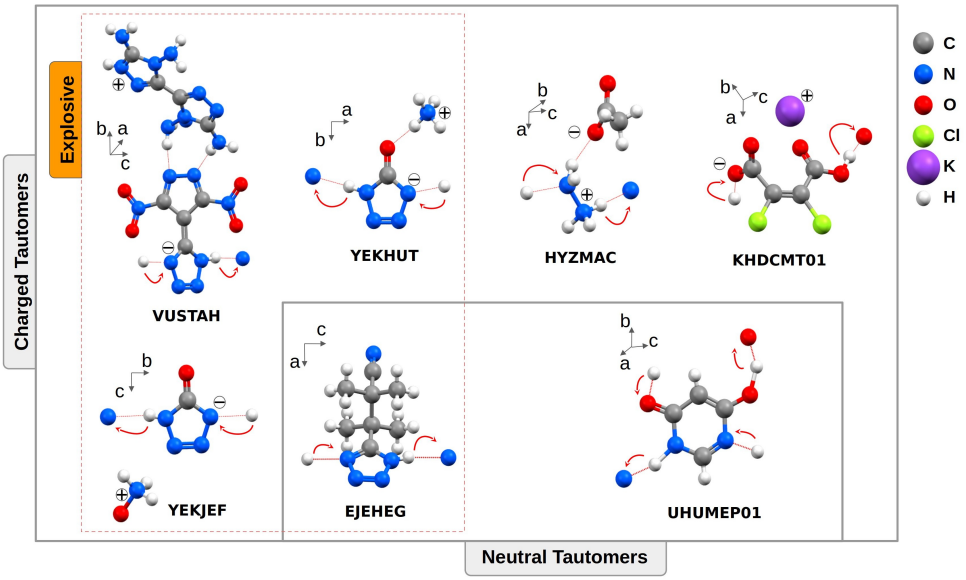


FIG. 7: Structures of the identified OPTFes candidates. The red arrows indicate the PT switching path. The orange box indicates explosive materials.

TABLE II: PT energy barriers and ferroelectric properties of reported and potential tautomeric OPTFes identified here. (∗) indicates that the $E_c$ is estimated from $U_{PT}^{col}$.

| | CSD refcode | $T_C$ (K) | $E_c$ | $\lvert \boldsymbol{P}_s^{exp} \rvert$ | $\lvert \boldsymbol{P}_s^{cal} \rvert$ | $U_{PT}^{col}$ (eV) | Space group | Chemical abbreviation |
|---|---|---|---|---|---|---|---|---|
| | AMBACO07 | 357 | 15.0 | 5.6 | 7.50 | 0.38 | $Pna2_1$ | Anthranilic acid[49] |
| Tautomers | ANPHPR01 | 348 | 20.0 | 3.6 | 4.03 | 0.80 | $Iba2$ | ALAA[1] |
| | GUMMUW02 | 380 | 14.0 | 30.0 | 31.20 | 0.30 | $Pca2_1$ | Croconic acid[9] |
| | REZBOP | 399 | 60.0 | 10.0 | 11.14 | 2.08 | $Pca2_1$ | DC-MBI[14] |
| | CBUDCX01 | 400 | 15.0 | 13.2 | 17.75 | 0.41 | $Cc$ | CBDC[50] |
| | KOWYEA02 | 449 | 20.0 | 7.4 | 7.61 | 0.65 | $Pc$ | MBI[9] |
| | PROLON01 | 363 | 10.0 | 9.0 | 9.42 | 0.26 | $Pna2_1$ | PhMDA[50] |
| | TAPZIT | 510 | 10.0 | 5.6 | 5.71 | 0.27 | $Pc$ | 3HPLN[50] |
| | Identified PT ferroelectric candidates | | | | | | | |
| Tautomers | HYZMAC | – | 20.41 * | – | 14.90 | 0.65 | $Cc$ | HAA[56] |
| | EJEHEG | – | 15.32 * | – | 7.38 | 0.46 | $Pca2_1$ | 3MTB[57] |
| | KHDCMT01 | – | 6.40 * | – | 6.71 | 0.12 | $P1$ | PHDCM[58] |
| | UHUMEP01 | – | 13.20 * | – | 4.41 | 0.38 | $Cc$ | 6HP[59] |
| | VUSTAH | – | 14.50 * | – | 0.33 | 0.43 | $Pna2_1$ | DADT-DNPT[60] |
| | YEKHUT | – | 21.79 * | – | 8.39 | 0.70 | $Fdd2$ | A5OT[61] |
| | YEKJEF | – | 17.93 * | – | 27.16 | 0.56 | $P2_1$ | HODA[61] |

Fig. 4**(b)**. In this case, the single PT with the lowest energy $U_{PT}^{sgl}$ can be considered as the rate-limiting step for polarization switching that creates a defect in the monovalent crystal.

The correlation analysis for the tautomeric compounds is shown in Fig. 5, demonstrating an almost linear relationship between $E_c$ and $U_{PT}^{col}$. For the $E_c$ values used in the correlation, we employed the reported experimental values measured using an electric field with the same frequency of about 5 Hz. Since the $T_C$ of tau-

tomeric compounds is significantly above room temperature, we neglected the measured temperature effect on the $E_c$ values.

In the acid-base salts, $U_{\rm PT}^{\rm sgl}$ are on average 70 % lower than the collective ones.

The lower single barriers suggest that ferroelectric switching has a single PT nature in the acid-base salts, in contrast, to a degree of collectively in the polarization switching of tautomeric compounds. In acid-base salts, nitrogen-to-oxygen single PT barriers ($U_{\rm PT,N\to O}^{\rm sgl}$) are in most cases much larger than oxygen-to-nitrogen barriers ($U_{\rm PT,O\to N}^{\rm sgl}$), thus, PT involves defects consisting of pairs of neutral acid-base molecules. An exception is MAMPUM03, for which $U_{\rm PT,O\to N}^{\rm sgl}$ is nearly twice that of $U_{\rm PT,N\to O}^{\rm sgl}$, which corresponds to a doubly charged local defect.

### C. Mining of CSD

In Figure 6, panel (a) depicts the workflow for CSD mining. The initial filter, which removes all but organic, non-polymeric, and non-disordered structures with an R-factor of $\leq$ 0.075, significantly reduced the dataset to approximately 69,000 crystal structures. In the subsequent set, the pseudo-inversion symmetry criterion, as described in Sec. II, resulted in 2079 structures, effectively filtering out nearly 97 % of these structures. Among these, 1093 structures, about half, were identified with "isolated protons" during this process. In the final step of verifying the presence of a connected PT path within the crystal, only 30 structures displayed a connected hydrogen-bonded network capable of mediating PT. Panel **(c)** illustrates a case of a connected nitrogen-to-nitrogen PT path.

The pseudo-symmetry-based searching method effectively found most of the earlier reported OPTFes deposited in the CSD. However, a few structures failed to meet the search criteria. One example is KIPMUT[62], a tautomeric OPTFe featuring an imidazole ring, which was reported in the CSD with a disordered structure. YONVOP,[63] another OPTFe, was not identified due to the distortion associated with the PT, which was significantly larger than the pseudosymmetry threshold. In addition to the earlier reported OPTFes, nine systems passed all criteria. Upon inspection of the structures, two of them, VURYEN and FAVFEP, were excluded from further DFT analysis due to their large unit cell size and likely low $\boldsymbol{P}_{\rm s}$ resulting from their anti-parallel alignment of molecular dipoles. For these systems, molecular distortion due to PT switching is quite significant. In VURYEN[64], which is a salt of 1-ammonionaphthalene and hydrogenoxalate, the displacement of 1-ammonionaphthalene reduces the degree of inversion symmetry. While, for FAVFEP[65], displacement of the 3,5-dihydroxybenzoate ions reduces the inversion symmetry as a result of protons being transferred between imidazole moieties.

Fig. 7 displays seven of the new OPTFe candidates discovered during the screening process, two of which are neutral tautomers, while five are ionic. All but hydrazinium acetate (HYZMAC), one of the ionic systems, exhibit proton tautomerism. In this case, the rearrangement of $\pi$ orbitals is missing, and a potentially switchable PT path is formed through $\rm NH_3^+\cdots NH_2$ hydrogen bond, with acetate anions serving as shielding spectators. The neutral system, UHUMEP01 is an analog of the RNA nucleobase uracil. In this case, the molecules can participate in a lactam-lactim tautomerism with two-interconnected and -intersecting PT paths in the *bc*-plane with $\rm NH\cdots N$ and $\rm OH\cdots O$ hydrogen bonds, respectively.[59] The other neutral system is EJEHEG, which has tetrazole-based backbone, in a one-dimensional hydrogen bond network with $\rm NH\cdots N$ interactions running along the *c*-axis. Additionally, three of the ionic OPTFes also have the tetrazole-based backbone. One of them, YEKHUT, is an ammonium 5-oxotetrazolate salt and is potentially explosive due to its high nitrogen content.[61] It forms crystals with orthorhombic symmetry, 16 ion pairs in the unit cell, and 3D hydrogen bonding. PT could occur in two sets of $\rm NH\cdots N$ chains parallel to the *ac* plane. The second is VUSTAH,[60] which has extensive hydrogen bonding, where PT may only occur along simple $\rm NH\cdots N$ chains parallel to the 4.88 Å unit cell axis. The final salt with a tetrazole backbone is YEKJEF,[61] another salt of 5-oxotetrazolate. In this case, the inversion symmetry was disrupted not only due to the locations of the protons but also because of the displacement of hydroxylammonium ions. Finally, KHDCMT01 is a hydrogen dichloromaleate potassium salt with zigzag $\rm COO^-\cdots COOH$ PT chains running along the *ac*-diagonals.

#### 1. *Spontaneous polarizations and PT barriers of identified compounds*

In the lower panel of Tab. II, we have listed $|\boldsymbol{P}_{\rm s}^{\rm cal}|$ and $U_{\rm PT}$ for the OPTFe candidates identified here. The values show a large variation, ranging from 0.3 $\mu$C/cm$^2$ of VUSTAH to 27.2 $\mu$C/cm$^2$ of YEKJEF. The large $|\boldsymbol{P}_{\rm s}^{\rm cal}|$ of YEKJEF can be related to the large density of molecular dipoles per area of the intersecting plane perpendicular to the polarization vector $\sim 0.1$ Å$^{-2}$, compared with $\sim 0.01$ Å$^{-2}$ of VUSTAH.

$U_{\rm PT}^{\rm col}$ were also computed for the identified candidates. Fig. 8 plots $|\boldsymbol{P}_{\rm s}^{\rm cal}|$ against $U_{\rm PT}^{\rm col}$ for identified candidates and, for comparison, the earlier reported candidates. All compounds except REZBOP have $U_{\rm PT}$ values less than 1.0 eV, and except for croconic acid and YEKJEF, all $|\boldsymbol{P}_{\rm s}^{\rm cal}|$ are less than 20 $\mu$C/cm$^2$. When comparing the $U_{\rm PT}^{\rm col}$ of ionic and neutral tautomeric compounds, the values fall within the same range, and there is no systematic increase or decrease in the barriers based on this classification. Because most of our identified ferroelec-

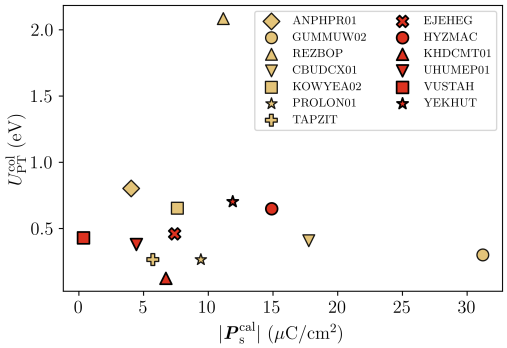


FIG. 8: $U_{\rm PT}^{\rm col}$ plotted against $|\boldsymbol{P}_{\rm s}^{\rm cal}|$ for tautomeric systems and identified candidates.

tric candidates exhibit tautomerism, we used the linear correlation line established for existing compounds with proton tautomerism to predict the $E_{\rm c}$ for the new ones. The predicted values fall within the range of 6 to 22 kV/cm, as listed in Tab. II.

## IV. SUMMARY AND CONCLUSION

By mining the CSD, we identified seven OPTFes candidates, in addition to 21 earlier reported compounds. 5 out of the 7 compounds are ionic, while all previously reported tautomeric OPTFes were neutral single-component tautomers. This identification could trigger the development of new ionic OPTFe tautomeric compounds, by combining charged tautomeric motifs with different anions. Their $|\boldsymbol{P}_{\rm s}^{\rm cal}|$ values range from 0.3 to 27.16 $\mu$C/cm$^2$. For reported compounds, we found that the experimental $E_{\rm c}$ correlate with the computed PT barrier, $U_{\rm PT}$, and we used such linear fits to estimate the $E_{\rm c}$ of the identified compounds, indicating values in the 6.4 to 22.0 kV/cm range. The DFT calculations and the correlation analysis suggested that tautomeric OPTFes have some degree of collectivity in their PT-switching. Our comparisons of compounds are in line with the intuitive notion that increasing the density of the PT-hydrogen bond can be used to increase $\boldsymbol{P}_{\rm s}$.

## DATA AVAILABILITY

The underlying DFT calculation and structures studied here study can be accessed at the NOMAD database at `https://dx.doi.org/10.17172/NOMAD/2023.06.01-1`. The supporting information provides a complete list of computed lattice vectors and hydrogen bond distances for the studied crystals. All other data is available upon reasonable request.

## ACKNOWLEDGMENTS

The computations of this work were carried out on UNINETT Sigma2 high-performance computing resources (grant NN9650K). This work is supported by the Research Council of Norway as a part of the Young Research Talent project FOX (302362).

[1] S. Horiuchi, K. Kobayashi, R. Kumai, and S. Ishibashi, Proton tautomerism for strong polarization switching, Nat. Commun. **8**, 14426 (2017).
[2] S. Horiuchi and Y. Tokura, Organic ferroelectrics, Nat. Mater. **7**, 357 (2008).
[3] M. Owczarek et. al., Flexible ferroelectric organic crystals, Nat. Commun. **7**, 13108 (2016).
[4] O. V. Gradov, M. A. Gradova, and V. V. Kochervinskii, 17 - biomimetic biocompatible ferroelectric polymer materials with an active response for implantology and regenerative medicine, in *Organic Ferroelectric Materials and Applications*, Woodhead Publishing Series in Electronic and Optical Materials, edited by K. Asadi (Woodhead Publishing, 2022) pp. 571–619.
[5] Z. Han and Q. Wang, 15 - ferroelectric polymers for energy harvesting, in *Organic Ferroelectric Materials and Applications*, Woodhead Publishing Series in Electronic and Optical Materials, edited by K. Asadi (Woodhead Publishing, 2022) pp. 503–533.
[6] M. Bozorg, A. Altomare, and K. Loos, 4 - synthesis of polyvinylidene fluoride and its copolymers, in *Organic Ferroelectric Materials and Applications*, Woodhead Publishing Series in Electronic and Optical Materials, edited by K. Asadi (Woodhead Publishing, 2022) pp. 85–112.
[7] H. S. Choi et. al., Tailoring the coercive field in ferroelectric metal-free perovskites by hydrogen bonding, Nat. Commun. **13**, 794 (2022).
[8] X.-J. Song et. al., Bistable state of protons for low-voltage memories, J. Am. Chem. Soc. **142**, 9000 (2020).
[9] S. Horiuchi et. al., Above-room-temperature ferroelectricity in a single-component molecular crystal, Nature **463**, 789 (2010).
[10] S. Horiuchi, S. Ishibashi, and Y. Tokura, 3-hydrogen-bonded organic molecular ferroelectrics/antiferroelectrics, in *Organic Ferroelectric Materials and Applications*, Woodhead Publishing Series in Electronic and Optical Materials, edited by K. Asadi (Woodhead Publishing, 2022) pp. 47–84.
[11] E. Dypvik Sødahl, S. Seyedraoufi, C. H. Görbitz, and K. Berland, Ferroelectric crystals of globular molecules: Cambridge structural database mining and computational assessment, Cryst. Growth Des. **23**, 8607 (2023).
[12] M. Szafrański and A. Katrusiak, Thermodynamic behavior of bistable NH+–N hydrogen bonds in monosalts of 1,4-diazabicyclo[2.2.2]octane, Chem. Phys. Lett. **318**, 427 (2000).
[13] M. Li, I. Katsouras, K. Asadi, P. W. M. Blom, and D. M. de Leeuw, Low voltage extrinsic switching of ferroelec-

tric $\delta$-pvdf ultra-thin films, Appl. Phys. Lett. **103**, 072903 (2013).
[14] S. Horiuchi et. al., Above-room-temperature ferroelectricity and antiferroelectricity in benzimidazoles, Nat. Commun. **3**, 1308 (2012).
[15] M. Sikora and A. Katrusiak, Pressure-controlled neutral–ionic transition and disordering of nh···n hydrogen bonds in pyrazole, J. Phys. Chem. C **117**, 10661 (2013).
[16] K. Lee, B. Kolb, T. Thonhauser, D. Vanderbilt, and D. C. Langreth, Structure and energetics of a ferroelectric organic crystal of phenazine and chloranilic acid, Phys. Rev. B **86**, 104 (2012).
[17] S. Ishibashi, S. Horiuchi, and R. Kumai, Hydrogen-bonded single-component organic ferroelectrics revisited by van der waals density-functional theory calculations, Phys. Rev. Mater. **5**, 094409 (2021).
[18] M. Dion, H. Rydberg, E. Schröder, D. C. Langreth, and B. I. Lundqvist, "Van der waals density functional for general geometries", Phys. Rev. Lett. **92**, 246401 (2004).
[19] K. Berland, V. R. Cooper, K. Lee, E. Schröder, T. Thonhauser, P. Hyldgaard, and B. I. Lundqvist, "Van der waals forces in density functional theory: a review of the vdW-DF method", Rep. Prog. Phys. **78**, 066501 (2015).
[20] C. R. Groom, I. J. Bruno, M. P. Lightfoot, and S. C. Ward, The Cambridge Structural Database, Acta. Crystallogr. B. **72**, 171 (2016).
[21] C. Capillas, E. S. Tasci, G. de la Flor, D. Orobengoa, J. M. Perez-Mato, and M. I. Aroyo, A new computer tool at the bilbao crystallographic server to detect and characterize pseudosymmetry, Z. Kristallogr. Cryst. Mater. **226**, 186 (2011).
[22] M. I. A. C. Capillas and J. M. Perez-Mato, Search for new pna21 ferroelectrics, Ferroelectrics **301**, 203 (2004).
[23] S. C. Abrahams, Systematic prediction of new inorganic ferroelectrics in point group 4, Acta. Crystallogr. B. **55**, 494 (1999).
[24] P.-P. Shi et. al., Symmetry breaking in molecular ferroelectrics, Chem. Soc. Rev. **45**, 3811 (2016).
[25] F. H. Allen, The cambridge structural database: a quarter of a million crystal structures and rising, Acta. Crystallogr. B. **58**, 380 (2002).
[26] K. Berland, E. D. Sødahl, and S. Seyedraoufi, Molcrys, `https://gitlab.com/m7582/molcrys/` (2023), [Online; accessed 01-May-2023].
[27] A. H. Larsen et. al., The atomic simulation environment—a python library for working with atoms, J. Condens. Matter. Phys. **29**, 273002 (2017).
[28] A. Hagberg, P. Swart, and D. S Chult, Exploring network structure, dynamics, and function using networkx (2008).
[29] G. Kresse and J. Hafner, Ab initio molecular dynamics for liquid metals, Phys. Rev. B **47**, 558 (1993).
[30] G. Kresse and J. Furthmüller, Efficiency of ab-initio total energy calculations for metals and semiconductors using a plane-wave basis set, Comput. Mater. Sci. **6**, 15 (1996).
[31] G. Kresse and J. Furthmüller, Efficient iterative schemes for ab initio total-energy calculations using a plane-wave basis set, Phys. Rev. B **54**, 11169 (1996).
[32] S. Seyedraoufi and K. Berland, Improved proton-transfer barriers with van der waals density functionals: Role of repulsive non-local correlation, J. Chem. Phys. **156**, 244106 (2022).
[33] R. D. King-Smith and D. Vanderbilt, Theory of polarization of crystalline solids, Phys. Rev. B **47**, 1651 (1993).
[34] R. Resta, Theory of the electric polarization in crystals, Ferroelectr. **136**, 51 (1992).
[35] R. Resta, Macroscopic polarization in crystalline dielectrics: the geometric phase approach, Rev. Mod. Phys. **66**, 899 (1994).
[36] G. Henkelman, B. P. Uberuaga, and H. Jónsson, A climbing image nudged elastic band method for finding saddle points and minimum energy paths, J. Chem. Phys. **113**, 9901 (2000).
[37] D. Chakraborty, K. Berland, and T. Thonhauser, Next-generation nonlocal van der waals density functional, J. Chem. Theory Comput. **16**, 5893 (2020).
[38] Kristian Berland et. al., van der Waals density functionals built upon the electron-gas tradition: Facing the challenge of competing interactions, J. Chem. Phys. **140**, 10.1063/1.4871731 (2014).
[39] T. Jenkins, K. Berland, and T. Thonhauser, "Reduced-gradient analysis of van der waals complexes", Electron. Struct. **3**, 034009 (2021).
[40] K. Berland and P. Hyldgaard, Exchange functional that tests the robustness of the plasmon description of the van der waals density functional, Phys. Rev. B **89**, 035412 (2014).
[41] E. D. Sødahl, J. Walker, and K. Berland, Piezoelectric response of plastic ionic molecular crystals: Role of molecular rotation, Cryst. Growth Des. **23**, 729 (2023).
[42] K. Lee, E. D. Murray, L. Kong, B. I. Lundqvist, and D. C. Langreth, Higher-accuracy van der waals density functional, Phys. Rev. B **82**, 081101 (2010).
[43] J. P. Perdew, K. Burke, and M. Ernzerhof, Generalized gradient approximation made simple, Phys. Rev. Lett. **77**, 3865 (1996).
[44] H. Peng, Z.-H. Yang, J. P. Perdew, and J. Sun, Versatile van der waals density functional based on a meta-generalized gradient approximation, Phys. Rev. X **6**, 041005 (2016).
[45] S. Grimme, J. Antony, S. Ehrlich, and H. Krieg, A consistent and accurate ab initio parametrization of density functional dispersion correction (DFT-D) for the 94 elements H-Pu, J. Chem. Phys. **132**, 154104 (2010).
[46] A. Tkatchenko and M. Scheffler, Accurate molecular van der waals interactions from ground-state electron density and free-atom reference data, Phys. Rev. Lett. **102**, 073005 (2009).
[47] A. H. Compton, The distribution of the electrons in atoms, Nature **95**, 343 (1915).
[48] M. Woińska, S. Grabowsky, P. M. Dominiak, K. Woźniak, and D. Jayatilaka, Hydrogen atoms can be located accurately and precisely by x-ray crystallography, Sci. Adv. **2**, e1600192 (2016).
[49] S. Horiuchi, Y. Noda, T. Hasegawa, F. Kagawa, and S. Ishibashi, Correlated proton transfer and ferroelectricity along alternating zwitterionic and nonzwitterionic anthranilic acid molecules, Chem. Mater. **27**, 6193 (2015).
[50] S. Horiuchi, R. Kumai, and Y. Tokura, Hydrogen-bonding molecular chains for high-temperature ferroelectricity, Adv. Mater. **23**, 2098 (2011).
[51] S. Horiuchi, S. Ishibashi, K. Kobayashi, and R. Kumai, Coexistence of normal and inverse deuterium isotope effects in a phase-transition sequence of organic ferroelectrics, RSC Adv. **9**, 39662 (2019).
[52] R. Kumai et. al., Structural assignment of polarization in hydrogen-bonded supramolecular ferroelectrics, J. Am. Chem. Soc. **129**, 12920 (2007).

[53] S. Horiuchi, R. Kumai, and Y. Tokura, A supramolecular ferroelectric realized by collective proton transfer, Angew. Chem. Int. Ed. **46**, 3497 (2007).

[54] S. Horiuchi, R. Kumai, and Y. Tokura, High-temperature and pressure-induced ferroelectricity in hydrogen-bonded supramolecular crystals of anilic acids and 2,3-di(2-pyridinyl)pyrazine, J. Am. Chem. Soc. **135**, 4492 (2013).

[55] F. Kagawa et. al., Polarization switching ability dependent on multidomain topology in a uniaxial organic ferroelectric, Nano Lett. **14**, 239 (2014).

[56] S. A. Hady, I. Nahringbauer, I. Olovsson, D. Heinegård, A. T. Balaban, and J. C. Craig, Hydrogen bond studies. 38. the crystal structure of hydrazinium acetate, Acta Chem. Scand. **23**, 2764 (1969).

[57] A. S. Lyakhov, S. V. Voitekhovich, P. N. Gaponik, and L. S. Ivashkevich, Non-linear optical crystals of 2,2,3-trimethyl-3-(1*H*-1,2,3,4-tetrazol-5-yl)butanenitrile, Acta Crystallogr. C **59**, o388 (2003).

[58] I. Olovsson, H. Ptasiewicz-Bak, T. Gustafsson, and I. Majerz, Asymmetric hydrogen bonds in centrosymmetric environment: neutron study of very short hydrogen bonds in potassium hydrogen dichloromaleate, Acta Crystallogr. C **57**, 311 (2001).

[59] A. Katrusiak and A. Katrusiak, Ionic disparity of identical molecules in polymorphs, Org. Lett. **5**, 1903 (2003).

[60] M. Benz, T. M. Klapötke, and J. Stierstorfer, Combining performance with thermal stability: Synthesis and characterization of 5-(3,5-dinitro-1h-pyrazol-4-yl)-1h-tetrazole and its energetic derivatives, Z. Anorg. Allg. Chem. **646**, 1380 (2020).

[61] D. Fischer, T. M. Klapötke, and J. Stierstorfer, Salts of tetrazolone – synthesis and properties of insensitive energetic materials, Propellants Explos. Pyrotech. **37**, 156 (2012).

[62] C. J. Serpell and P. D. Beer, Intermolecular interactions in bromo-, methyl-, and cyanoimidazole derivatives, Cryst. Growth Des **13**, 2866 (2013).

[63] Sanjay Dutta et. al., Record-high thermal stability achieved in a novel single-component all-organic ferroelectric crystal exhibiting polymorphism, Chem. Commun. **55**, 9610 (2019).

[64] H. Thakuria, B. M. Borah, A. Pramanik, and G. Das, Solid state synthesis and hierarchical supramolecular self-assembly of organic salt cocrystals, J. Chem. Crystallogr. **37**, 807 (2007).

[65] S. Jin, M. Guo, D. Wang, S. Wei, Y. Zhou, Y. Zhou, X. Cao, and Z. Yu, Five 3d supramolecular frameworks assembled from classical directional hydrogen-bonds and ch...o associations between carboxylic acids and bis-imidazoles, J. Mol. Struct. **1020**, 70 (2012).

Paper III

# Ferroelectric crystals of globular molecules: Cambridge Structural Database mining and computational assessment

**Elin Dypvik Sødahl, Seyedmojtaba Seyedraoufi, Carl Henrik Görbitz, Kristian Berland**

Published in *Crystal Growth & Design*, 14 November 2023. DOI: 10.1021/acs.cgd.3c00713

III

CRYSTAL GROWTH & DESIGN

pubs.acs.org/crystal

Article



# Ferroelectric Crystals of Globular Molecules: Cambridge Structural Database Mining and Computational Assessment

Elin Dypvik Sødahl,* Seyedmojtaba Seyedraoufi, Carl Henrik Görbitz, and Kristian Berland*

Cite This: *Cryst. Growth Des.* 2023, 23, 8607−8619

Read Online

ACCESS | Metrics & More | Article Recommendations | Supporting Information

**ABSTRACT:** Hybrid or organic molecular ferroelectrics hold the potential to serve as lead-free alternatives to conventional inorganic ferroelectrics. In particular, the variants composed of globular, often cage-like molecules can host attractive properties such as multiaxial ferroelectricity, Curie temperatures above room temperature, and orientationally disordered plastic mesophases, in addition to supporting low-temperature synthesis. Here, we present the results of a screening study of the Cambridge Structural Database (CSD) leading to the discovery of 54 candidate ferroelectrics, including molecular crystals and molecular salts, many of which are likely to host plastic mesophases, along with 16 previously reported ferroelectrics. With over 1.2 million entries in the CSD, the screening procedure involved many steps, including considerations of molecular geometry and size, space group, and hydrogen bonding pattern. Out of the candidate systems, many of them were identified to be likely to also host plastic mesophases due to their resemblance to highly symmetric close-packed crystal structures. The spontaneous polarization and electronic band gaps were predicted by using density functional theory. Among the candidate ferroelectrics, 17 exhibited a spontaneous polarization greater than 10 $\mu C/cm^2$, with five of them being reported at room temperature.

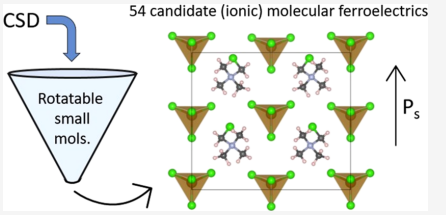




## 1. INTRODUCTION

Ferroelectric molecular crystals are potential alternatives to conventional inorganic ferroelectrics.[1−4] These materials can be synthesized with low-cost and low-energy methods such as coprecipitation, slow evaporation, spin coating, and 3D printing.[5−11] Furthermore, the abundance of available molecular species allows for tailoring of the properties of molecular crystals while eliminating the need for scarce or toxic elements. The ferroelectric molecular crystals can be formed solely through van der Waals and/or hydrogen bonding, and such systems are referred to as *molecular* crystals. Alternatively, they can also contain an additional ionic component originating from charged molecular species, which are termed *ionic molecular* crystals.

Of particular interest are (ionic) molecular crystals consisting of globular molecules. Their globular shape reduces the steric hindrance of rotational motion, making polarization switching through rotation possible. In some materials, rotational switching can also occur in combination with displacive mechanisms.[12] These materials can show rapid switching with frequencies of up to 263 kHz.[13−15] Moreover, molecular rotations in response to an applied electric field or mechanical force can result in large shear piezoelectric responses.[16] These types of molecular crystals can also crystallize in pseudo high-symmetry structures, thus allowing multiaxial polarization, with as many as 24 equivalent axes.[17−28] Multiaxial polarization allows the spontaneous polarization to be aligned in a desired direction in polycrystalline materials and could allow for multibit storage in single crystals.[29]

Ferroelectric (ionic) molecular crystals, in particular those of globular molecules, can also host orientationally disordered mesophases.[5,28,30−34] These phases can be highly ductile, or "plastic", which can arise from reduced intermolecular interactions, and increased symmetry yielding many facile slip planes.[34] This subgroup of molecular crystals is called plastic crystals, and the materials can be molded and fused, in contrast to the rigidity and brittleness observed for most molecular crystals and inorganic ceramics.[35]

Ferroelectric plastic crystals can exhibit a rich phase diagram,[36,37] with multiple competing crystalline phases and the existence of plastic ferroelectric mesophases. This is exemplified by quinuclidinium perrhenate, which displays a ferroelectric phase with partial orientational disorder.[5] A key advantage of these materials is that they can exhibit low coercive fields. For instance, values in the 2−5 kV/cm range have been reported for compounds such as 1-azabicyclo[2.2.1]heptanium perrhenate and quinuclidinium perrhenate.[5,38] These values are comparable to that of $BaTiO_3$, a well-known inorganic ferroelectric material.[39] Plastic crystals can also exhibit high Curie temperatures, which are

Received: June 12, 2023
Revised: October 28, 2023
Accepted: October 30, 2023
Published: November 14, 2023

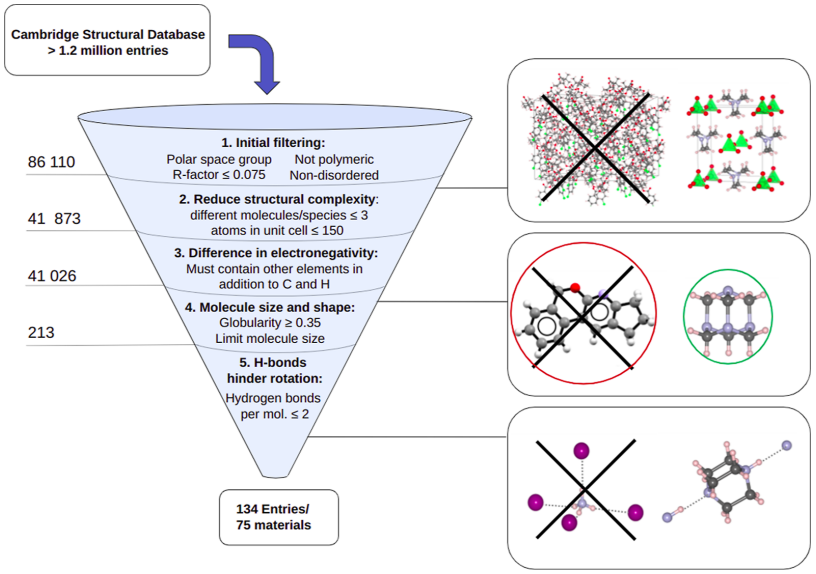


**Figure 1.** Overview of the screening procedure to identify ferroelectric plastic crystals in the CSD. The numbers on the left indicate the number of structures remaining after each filtering step.

essential for technological applications such as FeRAM and piezoelectric sensing. An example of this is 4-fluoro-1-azabicyclo[2.2.2]octan-1-ium perrhenate which has a Curie temperature of 466 K.[40,41]

In 2020, Horiuchi and Ishibashi compiled a catalog of approximately 80 reported ferroelectric crystals composed of small molecules.[11] This number is very small compared to the collection of approximately 1.2 million organic structures in the Cambridge Structural Database (CSD),[42] which potentially conceals numerous undiscovered ferroelectrics composed of small globular molecules, including plastic crystals. We recently screened this database, leading to the identification of six new candidates for organic proton-transfer ferroelectric materials.[43] In this paper, we provide a comprehensive account of our screening process for molecular ferroelectrics of globular molecules including an assessment of the potential to have plastic mesophases. For all of the systems uncovered, we used density functional theory (DFT) computations for geometry optimization and to predict the spontaneous polarization and the electronic band gaps. These newly identified systems are not only of interest in themselves but also serve as template structures for further crystal engineering, e.g., by substituting molecular species or halides to fine-tune functional properties.

## 2. METHODS

**2.1. Mining the CSD for Ferroelectric Plastic Crystals.** To identify candidate ferroelectrics composed in part or fully by small globular molecules, which also could be candidate plastic crystals in the CSD, we employed a systematic filtering process involving five distinct steps, as illustrated in Figure 1.[44] To execute this procedure, we utilized the CSD Python API 3.0.12[42] and the Molcrys[45] package developed by us, based on the Atomic Simulation Environment[46] and Networkx.[47]

**Step 1** excluded structures that were nonpolar, polymeric, or disordered, as well as less accurate structures with an *R*-factor ≥0.075.

**Step 2** excluded structures with unit cells containing more than 150 atoms. Thus, we avoided time-consuming DFT computations associated with complex and large structures.

**Step 3** excluded all material systems composed solely of C and H. This choice was based on the premise that polar covalent bonds or charge transfer between species is needed for high polarization, requiring electronegativity differences.

**Step 4** considered the shape of the molecules, removing all structures except those that contained 10 or fewer non-hydrogen atoms, consisted of extended linear segments, or did not contain at least one molecule with a globular or semiglobular geometry. These criteria were motivated by the fact that steric hindrance for molecular rotations should be small in the final structures. The criteria for identifying extended linear segments, such as an aliphatic side group, are detailed in the Supporting Information along with the criteria for globularity.

**Step 5** excluded structures where the globular molecules were connected by more than two hydrogen bonds as three directional intermolecular bonds would most likely hinder molecular rotations in all directions.

Following the application of filters, the initial pool of structures was reduced to 75. For each of these, we computed the spontaneous polarization and electronic band gaps using DFT. Note that while we identified a diverse range of systems, the screening criteria have caused some candidates to be omitted. For instance, limiting the number of atoms in the unit cell led to the exclusion of the ferroelectric metal-free plastic perovskite $[NH_3\text{-dabco}]NH_4I_3$ which has 198 atoms in its unit cell. Furthermore, the molecular size constraint excluded some known plastic crystals, including derivatives of adamantane, the $C_{60}$ fullerene,[48−50] and plastic colloidal crystals.[20] However, our primary goal was not to identify all molecular and plastic ferroelectrics but rather to pinpoint several systems of technological interest. Notably, molecular ferroelectrics comprising small molecules typically exhibit a larger density of dipoles, stemming both from individual molecules and intermolecular charge transfer.

**2.2. Additional Criteria to Identify Plastic Crystals.** While the screening procedure did uncover known plastic crystals, it is likely that many of the candidate systems also have plastic properties. Still, many of the systems would require further investigation to indicate the


https://doi.org/10.1021/acs.cgd.3c00713
Cryst. Growth Des. 2023, 23, 8607−8619

**Table 1. Overview of Earlier Reported Plastic Ferroelectrics That Were Discovered in the CSD Screening, Including Curie and Melting Temperatures, $T_c$ and $T_{melt.}$ [K], Coercive Field $E_c$ [kV/cm], Experimental and Computed Spontaneous Polarization, $P_{exp.}$ and $P_{calc.}$ [$\mu$C/cm$^2$], Computed Electronic Bandgap $E_g$ [eV], Crystallographic Space Group, Alignment of Dipoles, and Chemical Composition[a]**

| CSD refcode | $T_c$ | $T_{melt.}$ | $E_c$ | $P_{exp.}$ | $P_{calc.}$ | $E_g$ | Spg. | alignment (deg) | chem. comp. |
|---|---|---|---|---|---|---|---|---|---|
| | | | | Trimethyl-X-Y | | | | | |
| DIRKEU01[61] | 295[61] | | 67[61] | 2.0[61] | 5.5 | 0.3 | *Pma2* | | $(CH_3)_4N^+$, $FeCl_4^-$ |
| | | | | Cyclic Organic Molecules | | | | | |
| RUJBAC[62] | 454[62] | | | 1.1[62] | 1.7 | 1.9 | $P2_1$ | 66, 114; 36 | $2C_6H_{12}F_2N^+$, $PbI_4^{2-}$ |
| BUJQIJ[40] | 470[40] | | 10.8[40] | 0.48[40] | 2.7 | 4.6 | $P2_1$ | 76; − | $C_6H_{13}FN^+$, $I^-$ |
| BUJQOP[40] | 470[40] | | 9.4[40] | 0.40[40] | 2.8 | 4.6 | $P2_1$ | 76; − | $C_6H_{13}FN^+$, $I^-$ |
| | | | | Dabco-Based | | | | | |
| SIWKEP[63] | 374[63] | | 30[63] | 9.0[63] | 8.0[16] | 3.6 | *Cm* | | $C_6H_{13}N_2^+$, $ReO_4^-$ |
| TEDAPC28[64] | 378[37] | | | 4[64] | 5.9 | 5.2 | $Pm2_1n$ | | $C_6H_{13}N_2^+$, $ClO_4^-$ |
| WOLYUR08[65] | 374[65] | | | 5[65] | 6.2 | 5.3 | $Pm2_1n$ | | $C_6H_{13}N_2^+$, $BF_4^-$ |
| BILNES[66] | 390[66] | | | | 15.9 | 4.5 | *R3r* | 52; − | $C_7H_{16}N_2^{2+}$, $NH_4^+$, $3Br^-$ |
| BILNOC[66] | 446[66] | | 6−12[66] | 22[66] | 22.4 | 4.0 | *R3r* | 52; − | $C_7H_{16}N_2^{2+}$, $NH_4^+$, $3I^-$ |
| | | | | Quinuclidinium-Based | | | | | |
| LOLHIG02[41] | 466[41] | | | 11.4[41] | 12.7[16] | 4.4 | *Pn* | 3; − | $C_7H_{13}FN^+$, $ReO_4^-$ |
| OROWAV[5] | 367[5] | | 340[5] | 5.2[5] | 7.3[16] | 4.5 | $Pmn2_1$ | 5; − | $C_7H_{14}N^+$, $ReO_4^-$ |
| YASKIP[17] | 322[17] | | 255[17] | 6.7[17] | 6.5[16] | 2.9 | $Pmn2_1$ | 6; − | $C_7H_{14}N^+$, $IO_4^-$ |
| SIYWUT[67,68] | | | 1000[68] | 1.7[68] | 5.6[16] | 5.3 | $P4_1$ | 113; − | $C_7H_{14}NO^+$, $Cl^-$ |
| ABIQOU[68] | | | | | 5.2[16] | 5.0 | $P4_1$ | 113; − | $C_7H_{14}NO^+$, $Br^-$ |
| MIHTEE[69] | 400[69] | 492 | | 6.96[69] | 10.2 | 4.6 | $P6_1$ | 85 | (*R*)-$C_7H_{13}NO$ |
| QIVQIY[69] | 400[69] | | | 6.72[69] | 10.2 | 4.5 | $P6_5$ | 85 | (*S*)-$C_7H_{13}NO$ |
| | | | | Other Dielectric/Piezoelectric Properties Characterized | | | | | |
| ZZZVPE02[70] | | 367[34] | | | 17.2 | 6.4 | *R3m* | 0 | $(CH_3)_3BH_3N$ |
| BOXCUO[71] | | | | | | 0 | $P6_3mc$ | | $(CH_3)_4P^+$, $FeCl_4^-$ |
| QIMXER[72] | | | | | 9.1 | 4.7 | $Cmc2_1$ | | $C_6H_{13}N_2^+$, $Cl^-$ |
| BOBVIY12[73] | | | | | 6.7 | 3.8 | $Pmc2_1$ | | $C_6H_{13}N_2^+$, $I^-$ |
| BOCKEK06[74] | | | | | 12.2 | 4.8 | *P1* | | $C_6H_{13}N_2^+$, $HF_2^-$ |

[a]Melting points are retrieved from the CSD unless a reference is listed. The alignment of dipoles is expressed as the angle between molecular dipoles and the polarization axis, as explained in Section 3.3. The lowest temperature structure is listed for refcode families with more than one entry.

existence of a mesophase with plastic ductility. The presence of small globular molecules often allows for a rotational switching mechanism. However, in some systems, the switching path may not be clear-cut, necessitating more complex computations or experimental investigations for full evaluation. Second, for a material to host a plastic mesophase may require not only the existence of an orientationally disordered phase but also that this discorded phase has many facile slip planes, in particular, for the ionic systems. The transition to an orientationally disordered mesophase may involve significant repositioning of the molecules and shifts in the crystal structure, and it is not straightforward to assess the nature of the corresponding disordered phase if such a phase exists. Nonetheless, structures that pack in pseudo close-packed high-symmetry structures are more likely to host a plastic mesophase, as many slip planes would be available with the transition of a high orientational disorder. To assess the similarity to high-symmetry structures, we compared the overlap of radial distribution function (RDF) formed by the center-of-position of each molecule with those of reference structures, representing each molecule/atom as a Gaussian function, $g(r) = \exp[-(r - r_{dist.})^2/2\sigma^2]$, with a small broadening $\sigma$ to obtain a smooth radial distribution function. The RDFs were scaled so that the first peak positions were set to unity using a Gaussian broadening of $\sigma = 0.1$ for the ionic, and $\sigma = 0.07$ for the molecular crystals, i.e., in units effectively corresponding to the average center-to-center separations of the molecules. The overlap between the RDFs of the template structures and a given molecular crystal was performed with a scaled-distance cutoff of 2.3. The degree of overlap $O$ was evaluated as follows

$$M = \int_0^{r_{cut}} dr\ |\mathrm{RDF}(r) - \mathrm{RDF}^{template}(r)| \quad (1)$$

$$A = \int_0^{r_{cut}} dr\ \mathrm{RDF}(r) \quad (2)$$

$$B = \int_0^{r_{cut}} dr\ \mathrm{RDF}^{template}(r) \quad (3)$$

$$O = [1 + M^2/(M - (A + B))^2]^{-1} \quad (4)$$

For the ionic molecular crystals, the overlap was defined as the sum of the overlap for cations and anions combined and the overlap for cations and anions treated separately, i.e., $O = 0.5\ O_{anions,\ cations} + 0.25\ (O_{anions} + O_{cations})$.

In addition to this structure analysis, we also identified materials systems for which an orientationally disordered phase had been reported in the CSD. Since our initial CSD screening excluded disordered structures, all structures within each refcode family were investigated for competing disordered phases. In addition, to identify systems in which the disordered phase had been reported with a different refcode, we performed a structure search using Conquest.[51]

**2.3. Density Functional Theory Calculations.** The DFT computations were carried out using the VASP software package[52−55] with the projector augmented plane wave method (PAW) pseudopotentials.[56,57] The plane wave cutoff was set to 530 eV for all computations. A Γ-centered Monkhorst−Pack **k**-point grid with a spacing of 1/15 Å$^{-1}$ was used to sample the Brillouin zone. All structures were relaxed until the forces were reduced to below 0.01 eV/Å.



https://doi.org/10.1021/acs.cgd.3c00713
Cryst. Growth Des. 2023, 23, 8607−8619

Table 2. Overview of Candidate Ferroelectric Plastic Crystals That Were Discovered in the Screening of the CSD[a]

| | CSD refcode | $T_{struct.}$ | $T_{melt.}$ | $P_{calc.}$ | $E_g$ | Spg. | alignment (deg) | chem. comp |
|---|---|---|---|---|---|---|---|---|
| | | | | Trimethyl-X-Y | | | | |
| M(olecular) | ZZZVPQ01 | RT | | 3.0 | 5.8 | *R*3*mr* | 0 | $(CH_3)_3SO_3N$ |
| | LINZOX | RT | | 6.4 | 4.4 | *Ama*2 | 63 | $(CH_3)_3NH_3Al$ |
| | TMAMBF11 | 100 (RT) | 415[34] | 20.3 | 7.4 | *R*3*m* | 0 | $(CH_3)_3BF_3N$ |
| | CAVJOZ | 193 | | 0.04 | 2.8 | $P6_3mc$ | | $(CH_3)_3Cl_2Nb$ |
| | TBUHLB05 | 180 | 254 | 7.3 | 4.9 | $Pmn2_1$ | 19, 32, 33 | $(CH_3)_3BrC$ |
| | ETIPAY | 160 | 183 | 5.5 | 5.3 | $Pna2_1$ | 20 | $(CH_3)_3CH_2ClSi$ |
| I(onic) | WAGGAM | RT | | 11.0 | 2.7 | $P2_1$ | 6, 83; – | $2(CH_3)_3OS^+$, $Cr_2O_7^{2-}$ |
| | GEPZIK | 123 | 185 | 3.9 | 7.6 | $P6_3$ | | $(CH_3)_3HN^+$, $F^-$, 6HF |
| | ZISCUC | 300 | | 7.0 | 0.2 | *Cm* | 70; – | $(CH_3)_3CH_2ClN^+$, $FeCl_4^-$ |
| | YODGON | RT | | 3.1 | 5.0 | $Pmn2_1$ | | $(CH_3)_4N^+$, $OCN^-$ |
| | VUGNUG | RT | | 0.12 | 5.3 | $Pmn2_1$ | | $(CH_3)_4N^+$, $N_3^-$ |
| | XAKBUG | 223 | | 4.5 | 2.6 | *Abm*2 | 103; – | $(CH_3)_4N^+$, $OsFO_4^-$ |
| | MIWBEC | 293 | | 13.4 | 0.2 | $Pca2_1$ | 53; – | $(CH_3)_4N^+$, $FeCl_3NO^-$ |
| | ORUKUK | 100 | | 12.9 | 3.0 | $Pna2_1$ | | $(CH_3)_4N^+$, $Cl_3F_4^-$ |
| | ZOYGUP | RT | 484 | 3.1 | 4.1 | $P2_1$ | 68; – | $(CH_3)_4N^+$, $C_5H_7O_4^-$ |
| | SEYLAJ | 123 | 317 | 12.1 | 5.2 | $P3_1$ | | $(CH_3)_4N^+$, $OH^-$, $4H_2O$ |
| | PEVXOE | 100 | | | 0 | $Cmc2_1$ | | $(CH_3)_4P^+$, $O_2^-$, $2NH_3$ |
| | PEVXUK | 100 | | | 0 | $Cmc2_1$ | | $(CH_3)_4As^+$, $O_2^-$, $2NH_3$ |
| | XENFAZ | 295 | 493 | 8.4 | 1.7 | $P2_1$ | 17, 161; – | $2(CH_2O)_3NH_3C^+$, $HgI_4^{2-}$ |
| | | | | Dabco-Based | | | | |
| M | LOLWEO | RT | 429 | 7.6 | 3.4 | *Cc* | 18, 161; – | $C_6H_{12}N_2$, $2CH_4N_2S$ |
| | HUSRES | 150 | | 7.9 | 4.8 | $Pca2_1$ | –; 14 | $C_6H_{12}N_2$, $C_2H_5O_5P$ |
| I | USAFIG | 295 | | 0.4 | 3.4 | $Pna2_1$ | 95; – | $C_6H_{13}N_2O_2^+$, $NO_3^-$ |
| | VAGVAA01 | 150 | | 12.8 | 5.1 | $Pna2_1$ | | $C_6H_{14}N_2^{2+}$, $2Cl^-$ |
| | GASBIO | 123 | | 11.2 | 4.2 | $Pca2_1$ | | $C_6H_{14}N_2^{2+}$, $2I^-$, $H_2O$ |
| | NAKNOF03 | 150 | | 13.4 | 6.8 | *P*1 | | $C_6H_{14}N_2^{2+}$, $2BF_4^-$, $H_2O$ |
| | | | | Hexamine-Based | | | | |
| M | INEYUY/TAZPAD | 100 (RT) | | 0.9 | 3.8 | *R*3*m* | 0 | $C_6H_{12}N_3P$ |
| I | HMTAAB | RT | | 11.6 | 4.8 | $P6_3mc$ | | $C_6H_{12}N_4$, $NH_4^+$, $BF_4^-$ |
| | BOHNUH01 | 295 | | 10.6 | 4.9 | *R*3*m* | 83; – | $C_6H_{13}N_4^+$, $Br^-$ |
| | TOZTAF | 296 | | 17.3 | 4.3 | *Cc* | 138; 89 | $C_6H_{13}N_4^+$, $C_4H_5O_5^-$ |
| | | | | Boron Clusters | | | | |
| M | SASSOU | RT | 378 | 7.7 | 3.5 | *Cc* | 80 | $CH_{10}B_6S_2$ |
| | OTOLAM | 150 | | 11.5 | 5.5 | *Pnn*2 | 0 | $C_2H_{14}B_8$ |
| I | UTUZAM | 90 | | 3.2 | 4.8 | $P2_1$ | 56; – | $CH_{14}B_9^-$, $C_3H_{10}N^+$ |
| | LUWHOD | 340 | | 7.8 | 4.4 | $P4_2$ | | $B_{10}H_{10}^{2-}$, $2NH_4^+$, $NH_3$ |
| | | | | Cyclic Organic Molecules | | | | |
| I | WAQBOH | 295 | | 8.1 | 5.7 | *Pn* | | $C_4H_{11}N_2^+$, $BF_4^-$ |
| | CUWZOM | 100 | | 0.4 | 5.5 | $P2_1$ | 52; – | $C_5H_{11}FN^+$, $Cl^-$ |
| | AMINIT | 293 | | 6.8 | 4.5 | $P2_1$ | 126; 88 | $C_5H_{12}N^+$, $H_2AsO_4^-$ |
| | EVULAI | 100 | | 13.2 | 4.7 | $P2_1$ | 39 | $C_6H_{15}N_2S^+$, $Cl^-$ |
| | FENYEC | RT | 407 | 4.9 | 3.5 | *Cc* | 55; 85 | $C_7H_5O_3^-$, $C_4H_{10}N^+$ |
| | HAJXEW | 123 | | 16.5 | 5.6 | *Pn* | 16; – | $C_6H_{18}N_3^{3+}$, $ClO_4^-$, $2Cl^-$ |
| | OBEXEY | 200 | 416 | 7.6 | 4.8 | $Cmc2_1$ | | $C_9H_{20}N^+$, $N_3^-$ |
| | | | | Cage-like Organic Molecules | | | | |
| M | EQAXOL | 140 | | 9.1 | 5.4 | $Pna2_1$ | 48 | $C_5H_9O_3P$ |
| | BAPFAB | 150 | | 4.1 | 5.3 | $P2_1$ | 20, 56 | $C_6H_7FO_3$ |
| | BAPFOP | 150 | | 0.7 | 5.4 | $P2_1$ | 20 | $C_6H_7FO_3$ |
| | NOCPIE01 | 100 (RT) | | 14.9 | 4.5 | $P2_1$ | 51, 63 | $C_7H_{10}O_3$ |
| | MIRHUQ | 180 | 388 (sublim.) | 11.3 | 4.6 | $P2_1$ | 29, 31 | $C_8H_{15}PS$ |
| | XIBVIN | 180 | 443 | 1.3 | 4.2 | *C*2 | 77 | $C_8H_{15}PS$ |
| | BESWON | 130 | | 4.5 | 5.7 | $P3_1$ | 70 | $C_9H_{16}O$ |
| | FEJFAB | RT | | 7.4 | 2.1 | $Pmc2_1$ | 34; – | $C_6H_{10}N_2$, $CBr_4$ |
| I | PINRAI | 173 | | 5.3 | 5.8 | $Pna2_1$ | 60; – | $C_6H_9F_3N^+$, $Cl^-$ |
| | QAZFUV | 100 | | 11.5 | 5.2 | $Cmc2_1$ | 54; – | $C_6H_{12}N^+$, $Cl^-$ |
| | JEBVOC | 293 | >533 | 8.2 | 4.4 | $P2_1$ | 70; – | $C_9H_{14}N^+$, $Cl^-$ |
| | | | | Other | | | | |
| I | HUPTUI | 100 | | 0.4 | 3.7 | $P2_1$ | 86; – | $C_6H_{18}N_3S^+$, $TaF_6^-$ |
| | VAJKUM | RT | 513 | 1.7 | 3.2 | $P2_1$ | 85; 43 | $C_6H_{18}N_3S^+$, $SF_5O^-$ |
| | OTIJUZ | 123 | 393[75] | 2.6 | 5.1 | *Pc* | 43, 120; – | $2C_6H_{18}OPSi^+$, $S_2O_7^{2-}$ |



https://doi.org/10.1021/acs.cgd.3c00713
Cryst. Growth Des. 2023, 23, 8607−8619

**Table 2. continued**

[a]Values have been listed for the melting temperatures $T_{melt.}$ [K], computed spontaneous polarization $P_{calc.}$ [$\mu$C/cm$^2$], computed electronic bandgap $E_g$ [eV], crystallographic space group, alignment of dipoles, and chemical composition. Melting points are retrieved from the CSD unless a reference is listed. $T_{struct.}$ is the temperature at which the structure was determined (RT) and indicates that the structure is also reported at room temperature. The alignment of dipoles is expressed as the angle between molecular dipoles and the polarization axis, as explained in Section 3.3. The lowest temperature structure is listed for refcode families with more than one entry.

The spontaneous polarization was computed using the Berry phase method.[58,59] Rather than identifying nonpolar reference structures, which is the conventional procedure, we gradually increased the spacing between slabs of materials. In this case, the appropriate polarization branch can be identified by a nondiverging dipole element dipole per slab. The supercell size, i.e., the slab thickness, was converged to obtain a reliable description of the dipole moments.

For both relaxation and polarization calculations, the vdW-DF-cx functional was employed,[60] based on the accurate lattice constants determined in our earlier benchmarking study of exchange–correlation functionals for ferroelectric plastic crystals.[16]

## 3. RESULTS AND DISCUSSION

Among the 75 systems identified through the screening of the CSD, 16 have previously been reported to have ferroelectric properties.[5,17,37,40,41,61−69] Five more have been studied for their piezoelectric and/or dielectric properties but have not explicitly been reported as ferroelectric (CSD refcodes: ZZZVPE02, BOXCUO, QIMXER, BOBVIY12, and BOCKEK06).[70−74] Table 1 provides a summary of the available experimental results along with the computed values for spontaneous polarization and electronic band gaps for both the earlier reported ferroelectric and dielectric/piezoelectric materials. Table 2 lists the computed values for the other systems found in the screening. For three of these systems, the DFT computations did not yield a finite band gap. For these systems, we also computed the band gaps at the HSE06 hybrid functional level by Heyd, Scuseria, and Ernzerhof[76] which also showed an absence of a band gap.

Figure 2 shows an overview of the molecular and ionic molecular crystals among the previously reported and candidate ferroelectrics.

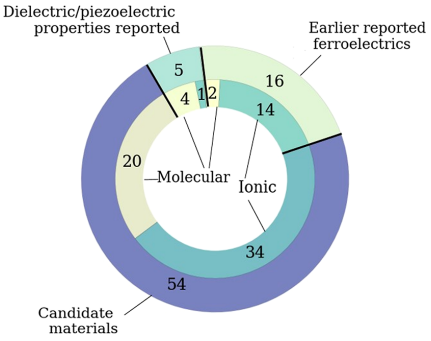


**Figure 2.** Overview of the candidate ferroelectrics, reported ferroelectrics, and materials with reported dielectric/piezoelectric properties identified in the screening. The outer circle indicates the number of structures in each of these groups, and the inner circle indicates the number of molecular and ionic molecular crystals.

Among the 16 known ferroelectrics, 14 are ionic molecular crystals. For the candidate systems, 20 are classified as molecular, while 35 are ionic molecular crystals.

Figure 3 illustrates a selection of the molecular entities found in these identified systems, which include globular molecules, neutral and charged molecules, and ions. In total, the systems encompass 30 different anionic molecules, 31 cations, and 25 neutral molecules.

Figure 4 outlines the seven distinct groups of systems identified based on the composition and geometry of the globular molecules. Three candidate systems do not fit into any of these categories and are listed as "Other" in Table 2.

Figure 5 compares the computed spontaneous polarization values with experimentally measured values for the previously reported ferroelectric molecular crystals.[5,17,40,41,61−66,68,69] While slightly larger, the computed values overall agree well with the experimental. The larger computed values can be attributed to extrinsic factors such as defects, grain orientation and boundaries, and electronic leakage which can reduce the experimental spontaneous polarization.[77,78] Additionally, atomic vibration and molecular librations may also cause spontaneous polarization to be reduced at a finite temperature. Moreover, the structures used for assessment with DFT were the ones in the CSD determined at the lowest temperature, while remaining the same polymorphs identified in the screening.

**3.1. Candidate Ferroelectric Plastic Crystals.** *3.1.1. Trimethyl-X-Y Systems.* One group of (ionic) molecular crystals identified in our screening is characterized by the presence of trimethyl-X-Y building blocks, where X denotes an atom and Y a chemical group or atom, as exemplified by the two structures in Figure 4. Among the 22 systems, only one, DIRKEU01, has previously been reported as ferroelectric. ZZZVPE02 has been reported to have a piezoelectric coefficient $d_{33}$ in the range of 10−16 pC/N and a pyroelectric coefficient of ≈25.8 $\mu$C/m$^2$ K.[70] Another compound, BOXCUO has been reported to have switchable dielectric and magnetic properties,[71] but this is one of the compounds for which DFT indicated a lack of electronic band gap.

Among the 19 remaining systems identified, seven are composed of neutral molecules, while the rest are formed from various combinations of 12 different anions and seven different cations. Tetramethylammonium is the most common cation, found in eight out of the 22 systems. The many possible combinations of molecules, and the fact that six of the systems exhibit computed spontaneous polarization values exceeding 10 $\mu$C/cm$^2$ (Table 2), indicate that the trimethyl-X-Y systems hold significant promise. The highest value is found for TMAMBF11 at 20.3 $\mu$C/cm$^2$.

*3.1.2. Dabco-Based Systems.* Crystals composed of various derivatives of 1,4-diazabicyclo[2.2.2]octane (dabco) in combinations with anions such as $ClO_4^-$ and $ReO_4^-$ have been found to have found to exhibit properties such as low coercive fields and rapid ferroelectric switching with frequencies up to 263 kHz.[13,15,24,63,79] Li et al. reported a Curie temperatures as high as 540 K for *N*-fluoroethyl-*N*-ZnI$_3$-1,4diazabicyclo[2.2.2]octonium.[80]

In our screening, we identified 13 dabco-based systems, out of which five have previously been reported as ferroelectrics.[37,63−66] Two of these, BILNES and BILNOC, can be classified as organic metal-free perovskites,[66] Figure 4. In addition to the reports of ferroelectric properties, the dielectric response of QIMXER, BOBVIY12, and BOCKEK06 have been characterized by Szafrański et al.[72−74] For the five previously identified ferroelectrics, we computed spontaneous polarization values ranging from 5.9 for TEDAPC28 to 22.4 $\mu$C/cm$^2$ for BILNOC, which can be compared to 0.4−13.4 $\mu$C/cm$^2$ for the additional systems identified. Interestingly, two of them, LOLWEO and HUSRES, are not ionic, but cocrystals of charge-neutral molecules.

*3.1.3. Quinuclidinium-Based Systems.* Several systems containing variations of the quinuclidinium molecule have been studied in recent years.[6,18,21,28,67−69,81,82] Notably, Tang et al. reported a Curie temperature of 466 K for [F-C$_7$H$_{13}$N]ReO$_4$.[41] Another material of interest is [C$_7$H$_{14}$N]IO$_4$, for which You et al. found 12 equivalent directions of polarization.[17] The reported coercive fields of these


https://doi.org/10.1021/acs.cgd.3c00713
Cryst. Growth Des. 2023, 23, 8607−8619

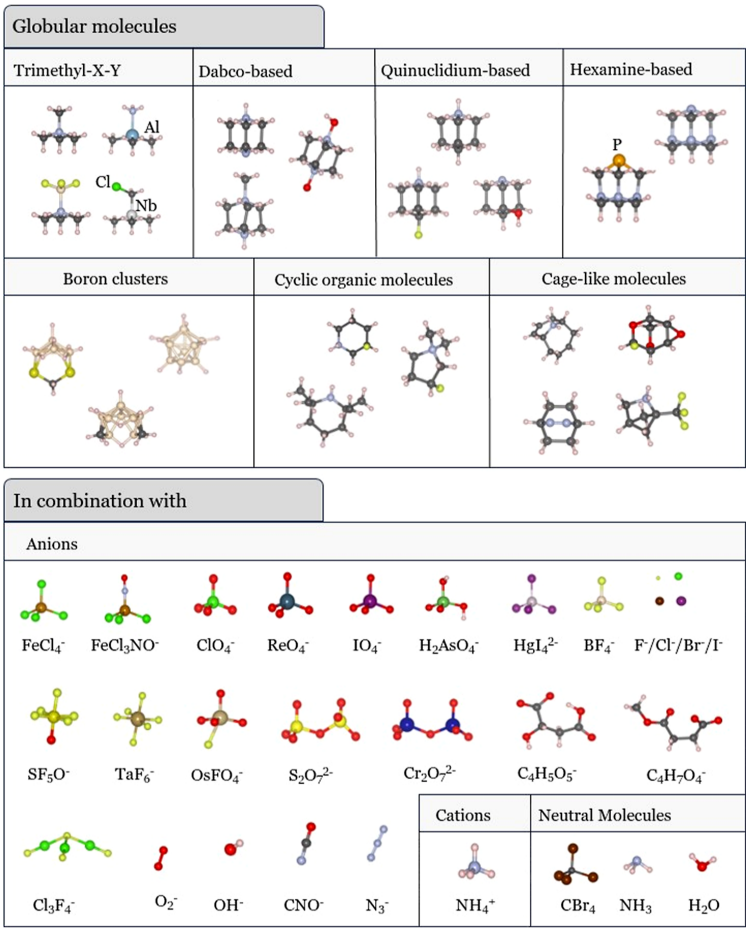


**Figure 3.** Examples of globular molecules and the anions, cations, and neutral molecules that are combined in the identified structures. In the top panel, carbon atoms are shown in gray, nitrogen in blue, oxygen in red, fluorine in yellow, boron in beige, and hydrogens as white. Other elements are labeled.

compounds are rather high, ranging from 255 to 1000 kV/cm.[68] All seven quinuclidinium-based systems found in this study have previously been reported as ferroelectrics[5,17,38,41,67−69] (Table 1). Five are plastic ionic crystals, while the two remaining are plastic molecular crystals and stereoisomers with identical compositions. The computed spontaneous polarizations of the quinuclidinium systems range from 5.2 to 12.7 $\mu$C/cm$^2$.

*3.1.4. Hexamine-Based Systems.* In our screening, we identified four hexamine-based crystal structures, none of which, to the best of our knowledge, have been reported as ferroelectrics in the past. Figure 3 shows the two variations of the hexamine molecule that we found, the regular hexamine molecule, and a derivative where a nitrogen atom has been substituted by phosphorus. Three structures are ionic molecular crystals with spontaneous polarizations ranging from 10.6 to 17.3 $\mu$C/cm$^2$ (Table 2). One of these, HMTAAB, features a perovskite-like structure; see Figure 4. The nonionic molecular crystal with a spontaneous polarization of 0.9 $\mu$C/cm$^2$ occurs with two different refcodes in the CSD; TAZPAD and INEYUY. The large spontaneous polarization values of the ionic hexamine-based systems should encourage further experimental characterization and optimization of these types of systems.

*3.1.5. Boron Cluster Systems.* While boron clusters have been extensively studied for their characteristic chemistry, biological application, and magnetic, optical, and electronic properties,[83−86] their ferroelectric characteristics have not received particular attention. Our screening study identified four systems containing boron clusters (Table 2). Two of them, SASSOU and LUWHOD, were measured at room temperature or higher and have spontaneous polarizations just below 8 $\mu$C/cm$^2$. The highest spontaneous polarization value is computed for OTOLAM, at 11.5 $\mu$C/cm$^2$. The combination of large polarization and room temperature stability renders the boron cluster-based systems interesting for further investigations.

*3.1.6. Systems Containing Cyclic Organic Molecules.* Ten of the systems identified contain cyclic organic molecules, both aromatic and nonaromatic, and we chose to group these together. All ten are ionic molecular crystals, including three earlier reported ferroelectrics[40,62] (Table 1), two of them have the same composition and are stereoisomers. The third, RUJBAC, is an organic−inorganic hybrid perovskite.[62] All three have spontaneous polarization below 3 $\mu$C/cm$^2$, coercive fields around 10 kV/cm,[40] and exhibit Curie temperatures exceeding 450 K.[40,62] Among the seven candidates


https://doi.org/10.1021/acs.cgd.3c00713
Cryst. Growth Des. 2023, 23, 8607−8619

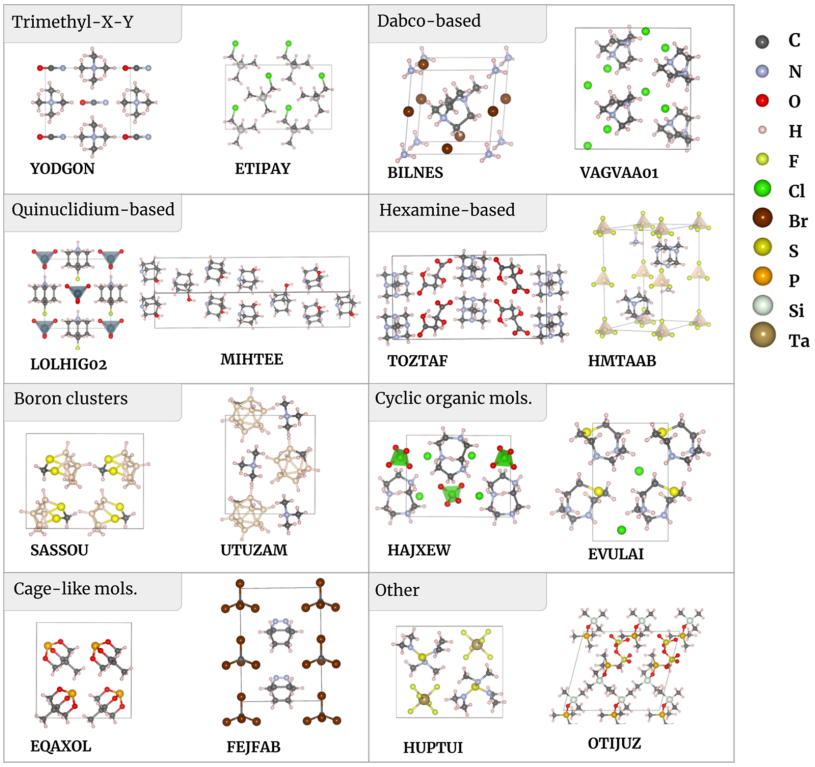


**Figure 4.** Examples of structures found in each of the eight groups of systems. ETIPAY, MIHTEE, SASSOU, EQAXOL, and FEJFAB are molecular crystals; the remaining are ionic.

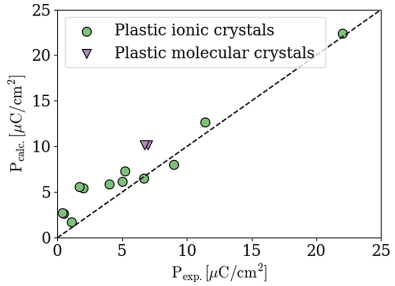


**Figure 5.** Computed spontaneous polarization compared to the experimentally measured values. Spontaneous polarization is reported for 14 out of the 16 known ferroelectrics identified in the screening.

identified here, all but one have spontaneous polarizations exceeding those of earlier reported ferroelectrics. HAJXEW has the largest value of 16.5 $\mu$C/cm$^2$ (Table 2). Three of the candidates identified, WAQBOH, AMINIT, and FENYEC have been reported as stable at room temperature, with the latter melting above 400 K.

*3.1.7. Systems Based on Organic Cage-like Molecules.* We found 11 crystal structures containing organic cage-like molecules, none of which have previously been reported as ferroelectric. Seven of these are molecular crystals, while four are ionic (Table 2). Even though there are no reported room temperature structures for MIRHUQ and XIBVIN, their reported sublimation and melting temperatures are high: 388 and 443 K, respectively. JEBVOC is reported to have a melting temperature of exceeding 533 K.

Finally, three of the candidate ferroelectrics do not fit into any of the defined groups. HUPTUI and VAJKUM have similar crystal structures and are built up of tris(dimethylamino)sulfonium molecule and an octahedral inorganic anion. For these systems, the computed spontaneous polarizations are below 3 $\mu$C/cm$^2$.

**3.2. Comparison of Candidate and Previously Reported Ferroelectrics.** The previously reported ferroelectrics frequently contain cage-like organic molecules, such as dabco and quinuclidinium derivatives, combined with halogen, $FeCl_4^-$, or $XO_4^-$ anions. The molecules in the identified candidates are by comparison generally smaller: 25 systems consist of molecules with five or fewer carbon atoms (not counting structures of boron clusters). The smaller volume of the asymmetric unit allows for larger spontaneous polarization. The lower molecular weights of the smaller molecules of the candidate systems could, however, lead to reduced melting points. Overall, the candidates display a more diverse set of anions that include entities such as $HF_2^-$, $CNO^-$, $FeCl_3NO^-$, and $SF_5O^-$.

**3.3. Polarization and Alignment of Molecules.** Molecules in plastic crystals often pack in complex arrangements, and the direction of the individual molecular dipoles does not necessarily align with the direction of the spontaneous polarization.[16] In Tables 1 and 2, the "dipolar" direction relative to the polarization direction is listed. Often, the unit cell holds several equivalent molecules that align at the same angle with the polarization axis, as given by space group symmetry. Mirror or rotational symmetries cause the polarization contributions perpendicular to the polarization axis to cancel out. For many of the molecules, their dipolar direction is thus evident from their symmetry, but not all molecules have a clear dipole direction due


https://doi.org/10.1021/acs.cgd.3c00713
Cryst. Growth Des. 2023, 23, 8607−8619

to their low symmetry, and even for symmetric molecules, the direction with respect to the high symmetry direction is not always clear-cut. For these molecules, we obtain an effective "dipole" direction from the moments of the electronegativity relative to the center of electronegativity and compute its relative angle to the overall spontaneous polarization direction.

Figure 6 illustrates the alignment of the molecular dipoles relative to the polarization axis for MIWBEC. In the cases where the molecules are symmetrical or have a negligible dipole, no alignment is listed. In these systems, interspecies charge transfer is the dominant contribution to spontaneous polarization. Examples of such systems are six of the dabco-based systems, SIWKEP, TEDAPC28, WOLYUR08, VAGVAA01, GASBIO, and NAKNOF03. Despite negligible molecular dipoles, their spontaneous polarizations are in the range 5.0−18.4 $\mu C/cm^2$. For systems where the molecular dipoles run counter to the overall polarization, an interesting prospect opens up for realignment of the dipoles by application of an electric field. This could both increase the spontaneous polarization and allow for multibit storage, assuming that the electric field required to realign the dipoles is smaller than the coercive field of the ferroelectric material.

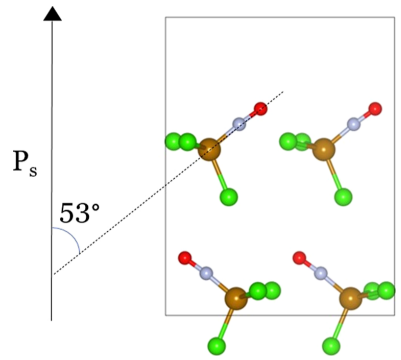


**Figure 6.** Illustration of the alignment of dipoles in MIWBEC (tetramethylamine molecules omitted for simplicity). The dipoles align along two directions, both 53°, on the polarization axis.

**3.4. Plastic Properties of the Candidate Ferroelectrics.** While the screening study can identify candidate ferroelectric plastic crystals, truly predicting whether the systems can transition to a plastic mesophase demands more involved simulations, such as molecular dynamics. This is not feasible for the large pool of candidate systems identified in this study, but out of the 16 identified known ferroelectrics, eight are reported to be plastic crystals, namely ABIQOU, SIYWUT, MIHTEE, QIVQIY, DIRKEU01, OROWAV, YASKIP, and LOLHIG02.[5,17,24,61,68,69] WOLYUR08, TEDAPC28, and SIWKEP are reported to have rotationally disordered high-temperature phases, but their mesophase ductility has not been investigated. Furthermore, the high-temperature phases of BUJQIJ and BUJQOP have not been resolved due to poor XRD data,[40] which can indicate the high degree of disorder characteristic for plastic crystals. Three candidate systems have been reported to be plastic crystals where all molecules exhibit rotational disorder, namely TMAMBF11,[34] ZZZVPE02,[34] and ZISCUC.[87] LOLWEO has a reported high-temperature phase in which one of the two molecular constituents shows an orientational disorder. Thus, the screening procedure is suited to identify systems with orientationally disordered mesophases.

High ductility is often linked to the existence of many slip systems. Thus, plastic properties are more likely in an orientationally disordered mesophase with a dense packing and high symmetry. High symmetry is particularly acute for the ionically bonded molecular crystals due to their limited number of slip planes. Thus, ionic molecular crystals that are pseudosymmetric to structures such as CsCl and NaCl are more likely to exhibit plastic behavior.

Figure 7 plots the overlap of the RDFs as defined in eqs 1−4 of systems composed of two molecular entities identified here with the structures of CsCl, NaCl, as well as zincblende. The horizontal line marks the known plastic crystal with the smallest overlap with a reference close-packed structure, namely, ZISCUC with an overlap of 0.83 with the CsCl structure. Structures with a larger overlap are likely to host plastic mesophases. In total, 17 of the systems fulfill these criteria, including all 7 of the materials with previously reported plastic properties. However, it is important to keep in mind that our assessment is quite rough and does not take into account factors such as the available space for rotation; moreover, several of the

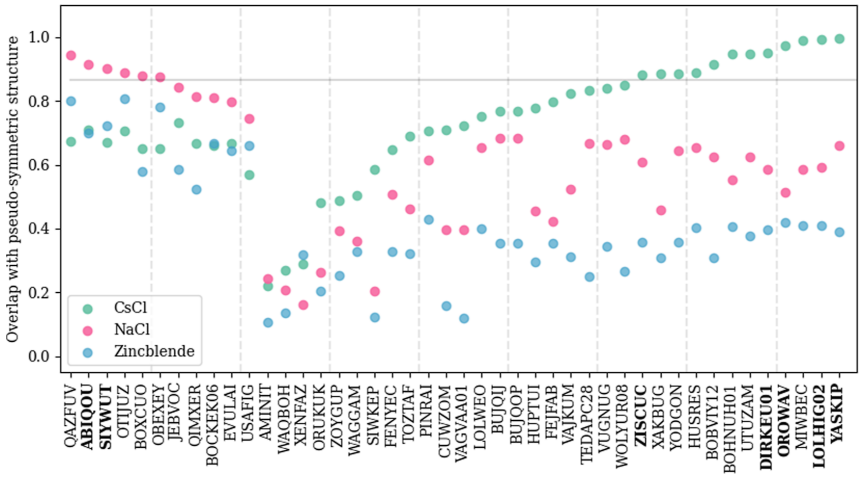


**Figure 7.** Overlap between the ionic molecular crystals identified in the screening with structure types that can allow for plastic properties. The horizontal line marks the lowest overlap calculated for the known plastic crystals identified here. Structures earlier reported as plastic crystals are marked with boldface.


https://doi.org/10.1021/acs.cgd.3c00713
Cryst. Growth Des. 2023, 23, 8607−8619

compounds not fulfilling this criterion may, for instance, exhibit a significant positional shift in the transition to an orientationally disordered mesophase.

Figure 8 plots the overlap between the molecular crystals and hexagonal close-packed (hcp), body-centered cubic (bcc), and face-centered cubic (fcc) structures. Here, the smallest overlap between a known plastic crystal and a reference structure is ZZZVPE02, which has an overlap of 0.96 with the bcc structure and 0.86 with the hcp structure. The close-packed structures built up of a single molecular species are harder to differentiate than the ones composed of two species using the overlap based on the RDF-overlap.

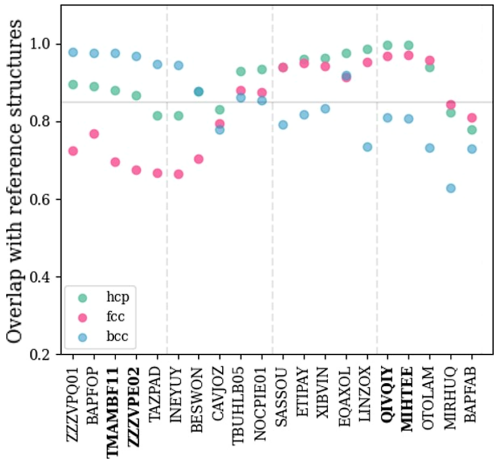


**Figure 8.** Overlap between the molecular crystals identified in the screening with structure types that can allow for plastic properties. The horizontal line marks the lowest overlap calculated for the known molecular plastic crystals identified here. Structures earlier reported as plastic crystals are marked with boldface.

This is the case for two of the crystals with reported plastic properties, TMAMBF11 and ZZZVPE02, which show large similarities to both hcp- and bcc-type packing. These two isostructural systems crystallize in the *R*3*m* space group, Figure 9, and are reported to have ductility comparable with metals in their plastic phases.[34] A large overlap with the close-packed hcp and fcc structures can indicate plasticity; 14 of the molecular crystals have an overlap larger than 0.86 with the hcp or fcc structures, indicative of plastic properties, including the four reported plastic crystals. Finally, we note that the existence of many slip planes and high symmetry might be less critical for the (nonionic) molecular crystals. Other deformation mechanisms can also be present, such as creep close to the melting temperature. Onset of configurational disorder has been associated with increased plasticity in molecular crystals.

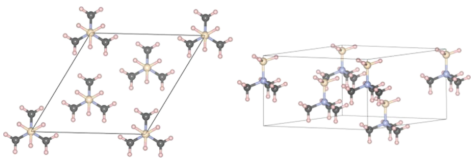

**Figure 9.** Crystal structure of the plastic molecular crystal ZZZVPE02, isostructural to TMAMBF11.

Overlap with close-packed structures was not evaluated for the 11 structures composed of three molecular entities identified in this study due to their complexity. Out of these, four have perovskite-type structures; RUJBAC, BILNES, BILNOC, and HMTAAB. While these might be less likely to host a plastic mesophase, plastic behavior has earlier been reported for hybrid perovskites.[88−90]

**3.5. Thermal Stability.** For device applications, thermal stability is an important property and operational temperatures should be significantly below melting and sublimation temperatures. The melting temperature of plastic crystals can be higher than for similar ionic and molecular crystals, due to the high entropy associated with the orientational disorder and increased freedom of movement making melting less favorable, as first reported by Timmermans.[30] The volume change at the phase transition is also small.[91]

For 45 of the 75 systems identified in this study, the crystal structure is ordered with a ferroelectric space group and obtained at ambient temperature. For the four systems, a paraelectric phase is reported at room temperature. Finally, 26 systems lack a reported crystalline room temperature phase in the CSD. The fraction of room temperature investigations is highest for ionic crystals, Figure 10, a result that is in line with the higher stability of the ionic molecular crystals, due to electrostatic interactions.

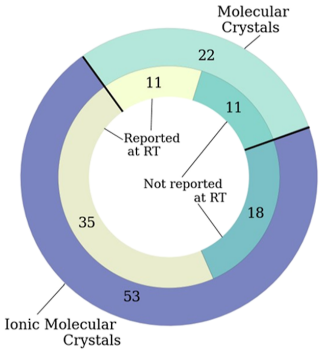


**Figure 10.** Overview of the molecular and ionic crystals identified. The outer ring indicates the number of systems, and the inner ring indicates if the potentially ferroelectric phase is reported at room temperature.

**3.6. Electronic Band Gap and Multisource Energy Harvesting.** Ferroelectric materials with band gaps in the visible range can be of particular interest, as these could be promising for application in multisource energy harvesting devices where piezo- or pyroelectric energy harvesting is combined with the harvesting of solar energy.[92,93] Therefore, we computed the band gaps for all identified systems to find those that could be suitable for such applications.

Tables 1 and 2 list the computed band gaps. Since the computations were performed using the vdW-DF-cx functional, which describes exchange at the generalized-gradient approximation level,[60] we can expect the band gaps to be underestimated. Most of the computed band gaps exceed 4 eV; however, six systems have values smaller than 2 eV. Four of these belong to the trimethyl-X-Y group, which could thus be interesting for multisource energy harvesting.

**3.7. Design Strategies for Ferroelectric Plastic Crystals.** Novel and improved ferroelectric plastic crystals can be engineered by making new combinations of molecular species. As such, the various species found in the various plastic crystal candidates can be used as building blocks for novel material design; a selection of these is displayed in Figure 3.

Of particular interest are substitutions that are likely to result in similar or isostructural crystals. For systems where this is possible, solid-solution engineering can be used to tweak the material properties. Three examples of pairs of candidates for such alterations are found among the trimethyl-X-Y systems. The compositions


https://doi.org/10.1021/acs.cgd.3c00713
Cryst. Growth Des. 2023, 23, 8607−8619

between each pair of systems are similar, only differing by the substitution of molecules with similar geometries. PEVXOE and PEVXUK are isostructural and only differ by the substitution of $(CH_3)_4P^+$ for $(CH_3)_4As^+$. For ZZZVPE02 and TMAMBF11, the substitution of $(CH_3)_3BH_3N$ to $(CH_3)_3BF_3N$ yields an isostructural material where the computed polarization is increased from 17.2 to 20.3 $\mu C/cm^2$. A similar effect is seen for YODGON and VUGNUG, where the substitution of $N_3^-$ for $OCN^-$ leads to an increase in the spontaneous polarization from 0.13 to 3.1 $\mu C/cm^2$.

Another example of substitution resulting in similar packing is the earlier reported ferroelectrics TEDAPC28 and SIWKEP, which consist of a dabco molecule and a tetrahedral inorganic ion, $ClO_4^-$ or $ReO_4^-$, respectively. This substitution somewhat changes the orientation of molecules, resulting in a different space group. Whereas, we found a spontaneous polarization of 8 $\mu C/cm^2$ for the $ReO_4^-$ system, the $ClO_4^-$ one has a value of 5.9 $\mu C/cm^2$.

In total, ten different tetrahedral inorganic anions were found in our screening study, such as $BF_4^-$, $FeCl_3ON^-$ and $IO_4^-$, but other options also exist and can be considered for the design of new ferroelectric plastic crystals. Substitutions of single atoms in the organic globular molecule can also be a route to engineer the ferroelectric properties.[94] For instance, Lin et al. substituted a hydrogen atom in tetramethylammonium for halogens I, Cl, and Br. The crystal structure was retained, while the number of ferroelectric polar axes increased from 2 for iodine to 6 for chlorine.[95]

## 4. CONCLUSIONS

Using a CSD-based workflow, we identified 54 candidate ferroelectric molecular crystals. The 17 with spontaneous polarization exceeding 10 $\mu C/cm^2$ are arguably the ones with the most potential in ferroelectric devices. Among these, five in the trimethyl-X-Y group also display a large variation in electronic band gaps that could make them useful for multisource energy harvesting. Ten likely plastic molecular crystals and ten likely plastic ionic molecular crystals were identified among the candidate systems by comparing the crystal structures of the candidate systems with close-packed crystal structures.

Our study has successfully identified a range of candidate ferroelectric molecular and molecular ionic crystals, including 16 that have been reported as ferroelectrics in the past. The screening criteria used were quite strict, and relaxing some of them, such as the size limitations on both molecules and unit cells, would have expanded the pool. The criteria were based on previously reported ferroelectric molecular and molecular ionic crystals. For this reason, crystal structures that differ significantly from the earlier reported ones could have been overlooked. Still, the identification of the boron cluster-based systems was unexpected, illustrating the potency of the CSD screening. In the design of novel ferroelectric plastic crystals, a good starting point is combining different globular molecular species, e.g., combinations of cations and anions. The various molecular species in the systems identified here and the corresponding crystal structures can serve as inspiration for such design.

In this study, we have not assessed whether the polarizations of the candidate ferroelectrics are switchable, which is a criterion for ferroelectricity. However, all of the candidate systems will necessarily have pyro- and piezoelectric properties as of their polar crystal symmetries. This study and the identified systems should stimulate further theoretical or experimental studies to assess their ferroelectric switchability and other characteristics such as the Curie temperatures and material stability.

## ■ ASSOCIATED CONTENT

### Data Availability Statement

All the relaxed crystal structures used in this study can be accessed through the NOMAD database at https://dx.doi.org/10.17172/NOMAD/2023.06.12-1. All other data are available upon reasonable request. Scripts for computing globularity and Network properties are available in the Molcrys package.

### Supporting Information

The Supporting Information is available free of charge at https://pubs.acs.org/doi/10.1021/acs.cgd.3c00713.

Description of the screening tools and criteria used for molecular geometries, including the evaluation of the globularity of molecules and the identification of extended linear segments (PDF)

## ■ AUTHOR INFORMATION


### Corresponding Authors

**Elin Dypvik Sødahl** − *Department of Mechanical Engineering and Technology Management, Norwegian University of Life Sciences, 1432 Ås, Norway;* orcid.org/0000-0001-8877-9044; Email: elin.dypvik.sodahl@nmbu.no

**Kristian Berland** − *Department of Mechanical Engineering and Technology Management, Norwegian University of Life Sciences, 1432 Ås, Norway;* orcid.org/0000-0002-4655-1233; Email: kristian.berland@nmbu.no

### Authors

**Seyedmojtaba Seyedraoufi** − *Department of Mechanical Engineering and Technology Management, Norwegian University of Life Sciences, 1432 Ås, Norway;* orcid.org/0000-0003-3800-0412

**Carl Henrik Görbitz** − *Department of Chemistry, University of Oslo, 0371 Oslo, Norway*

Complete contact information is available at: https://pubs.acs.org/10.1021/acs.cgd.3c00713


### Notes

The authors declare no competing financial interest.

## ■ ACKNOWLEDGMENTS

The computations of this work were carried out on UNINETT Sigma2 high-performance computing resources (grant NN9650K). This work is supported by the Research Council of Norway as a part of the Young Research Talent project FOX (302362).

## ■ REFERENCES


(1) Vijayakanth, T.; Liptrot, D. J.; Gazit, E.; Boomishankar, R.; Bowen, C. R. Recent Advances in Organic and Organic−Inorganic Hybrid Materials for Piezoelectric Mechanical Energy Harvesting. *Adv. Funct. Mater.* **2022**, *32*, 2109492.

(2) Pan, Q.; Xiong, Y.-A.; Sha, T.-T.; You, Y.-M. Recent progress in the piezoelectricity of molecular ferroelectrics. *Mater. Chem. Front.* **2021**, *5*, 44−59.

(3) Tayi, A. S.; Kaeser, A.; Matsumoto, M.; Aida, T.; Stupp, S. I. Supramolecular ferroelectrics. *Nat. Chem.* **2015**, *7*, 281−294.

(4) Zhang, Y.; Di, F.; Li, P.; Xiong, R. Crown Ether Host-Guest Molecular Ferroelectrics. *Chem.—Eur. J.* **2022**, *28*, No. e202102990.

(5) Harada, J.; Shimojo, T.; Oyamaguchi, H.; Hasegawa, H.; Takahashi, Y.; Satomi, K.; Suzuki, Y.; Kawamata, J.; Inabe, T. Directionally tunable and mechanically deformable ferroelectric crystals from rotating polar globular ionic molecules. *Nat. Chem.* **2016**, *8*, 946−952.

(6) Deng, S.; Li, J.; Chen, X.; Hou, Y.; Chen, L. A novel ferroelectric based on quinuclidine derivatives. *Chin. Chem. Lett.* **2020**, *31*, 1686−1689.
(7) Lan, X.; Wang, X.; Zhang, D. X.; Mu, T.; Lan, X. Z. Cation and Anion Transfer in Quinuclidinium Hexafluorophosphate Plastic Crystal: Role of Constituent Ions and the Crystalline Structure. *J. Phys. Chem. C* **2021**, *125*, 21169−21178.
(8) Owczarek, M.; Hujsak, K. A.; Ferris, D. P.; Prokofjevs, A.; Majerz, I.; Szklarz, P.; Zhang, H.; Sarjeant, A. A.; Stern, C. L.; Jakubas, R.; Hong, S.; Dravid, V. P.; Stoddart, J. F. Flexible ferroelectric organic crystals. *Nat. Commun.* **2016**, *7*, 13108.
(9) Walker, J.; Scherrer, S.; Løndal, N. S.; Grande, T.; Einarsrud, M.-A. Electric field dependent polarization switching of tetramethylammonium bromotrichloroferrate(III) ferroelectric plastic crystals. *Appl. Phys. Lett.* **2020**, *116*, 242902.
(10) Hu, Y.; Gottfried, J. L.; Pesce-Rodriguez, R.; Wu, C.-C.; Walck, S. D.; Liu, Z.; Balakrishnan, S.; Broderick, S.; Guo, Z.; Zhang, Q.; An, L.; Adlakha, R.; Nouh, M.; Zhou, C.; Chung, P. W.; Ren, S. Releasing chemical energy in spatiallyprogrammed ferroelectrics. *Nat. Commun.* **2022**, *13*, 6959.
(11) Horiuchi, S.; Ishibashi, S. Hydrogen-Bonded Small-Molecular Crystals Yielding Strong Ferroelectric and Antiferroelectric Polarizations. *J. Phys. Soc. Jpn.* **2020**, *89*, 051009.
(12) Shi, P.-P.; Tang, Y.-Y.; Li, P.-F.; Liao, W.-Q.; Wang, Z.-X.; Ye, Q.; Xiong, R.-G. Symmetry breaking in molecular ferroelectrics. *Chem. Soc. Rev.* **2016**, *45*, 3811−3827.
(13) Sun, Z.; Yi, X.; Tao, K.; Ji, C.; Liu, X.; Li, L.; Han, S.; Zheng, A.; Hong, M.; Luo, J. A Molecular Ferroelectric Showing Room-Temperature Record-Fast Switching of Spontaneous Polarization. *Angew. Chem.* **2018**, *130*, 9981−9985.
(14) Gao, K.; Gu, M.; Qiu, X.; Ying, X. N.; Ye, H.-Y.; Zhang, Y.; Sun, J.; Meng, X.; Zhang, F. M.; Wu, D.; Cai, H.-L.; Wu, X. S. Above-room-temperature molecular ferroelectric and fast switchable dielectric of diisopropylammonium perchlorate. *J. Mater. Chem. C* **2014**, *2*, 9957−9963.
(15) Tang, Y.-Y.; Zhang, W.-Y.; Li, P.-F.; Ye, H.-Y.; You, Y.-M.; Xiong, R.-G. Ultrafast Polarization Switching in a Biaxial Molecular Ferroelectric Thin Film: [Hdabco]$ClO_4$. *J. Am. Chem. Soc.* **2016**, *138*, 15784−15789.
(16) Sødahl, E. D.; Walker, J.; Berland, K. Piezoelectric Response of Plastic Ionic Molecular Crystals: Role of Molecular Rotation. *Cryst. Growth Des.* **2023**, *23*, 729−740.
(17) You, Y.-M.; Tang, Y.-Y.; Li, P.-F.; Zhang, H.-Y.; Zhang, W.-Y.; Zhang, Y.; Ye, H.-Y.; Nakamura, T.; Xiong, R.-G. Quinuclidinium salt ferroelectric thin-film with duodecuple-rotational polarization-directions. *Nat. Commun.* **2017**, *8*, 14934.
(18) Xie, Y.; Ai, Y.; Zeng, Y.-L.; He, W.-H.; Huang, X.-Q.; Fu, D.-W.; Gao, J.-X.; Chen, X.-G.; Tang, Y.-Y. The Soft Molecular Polycrystalline Ferroelectric Realized by the Fluorination Effect. *J. Am. Chem. Soc.* **2020**, *142*, 12486−12492.
(19) Wang, B.; Ma, D.; Zhao, H.; Long, L.; Zheng, L. Room Temperature Lead-Free Multiaxial Inorganic−Organic Hybrid Ferroelectric. *Inorg. Chem.* **2019**, *58*, 13953−13959.
(20) Das, S.; Mondal, A.; Reddy, C. M. Harnessing molecular rotations in plastic crystals: a holistic view for crystal engineering of adaptive soft materials. *Chem. Soc. Rev.* **2020**, *49*, 8878−8896.
(21) Yang, C.-K.; Chen, W.-N.; Ding, Y.-T.; Wang, J.; Rao, Y.; Liao, W.-Q.; Xie, Y.; Zou, W.; Xiong, R.-G. Directional Intermolecular Interactions for Precise Molecular Design of a High- $T_c$ Multiaxial Molecular Ferroelectric. *J. Am. Chem. Soc.* **2019**, *141*, 1781−1787.
(22) Harada, J. Plastic/ferroelectric molecular crystals: Ferroelectric performance in bulk polycrystalline forms. *APL Mater.* **2021**, *9*, 020901.
(23) Ai, Y.; Zeng, Y.-L.; He, W.-H.; Huang, X.-Q.; Tang, Y.-Y. Six-Fold Vertices in a Single-Component Organic Ferroelectric with Most Equivalent Polarization Directions. *J. Am. Chem. Soc.* **2020**, *142*, 13989−13995.
(24) Tang, Y.-Y.; Li, P.-F.; Zhang, W.-Y.; Ye, H.-Y.; You, Y.-M.; Xiong, R.-G. A Multiaxial Molecular Ferroelectric with Highest Curie Temperature and Fastest Polarization Switching. *J. Am. Chem. Soc.* **2017**, *139*, 13903−13908.
(25) Zhang, Y.; Song, X.-J.; Zhang, Z.-X.; Fu, D.-W.; Xiong, R.-G. Piezoelectric Energy Harvesting Based on Multiaxial Ferroelectrics by Precise Molecular Design. *Matter* **2020**, *2*, 697−710.
(26) Zafar, Z.; Zafar, A.; Guo, X.; Lin, Q.; Yu, Y. Raman evolution of order−disorder phase transition in multiaxial molecular ferroelectric thin film. *J. Raman Spectrosc.* **2019**, *50*, 1576−1583.
(27) Tang, Y.-Y.; Li, P.-F.; Liao, W.-Q.; Shi, P.-P.; You, Y.-M.; Xiong, R.-G. Multiaxial Molecular Ferroelectric Thin Films Bring Light to Practical Applications. *J. Am. Chem. Soc.* **2018**, *140*, 8051−8059.
(28) Zhang, H.-Y.; Tang, Y.-Y.; Shi, P.-P.; Xiong, R.-G. Toward the Targeted Design of Molecular Ferroelectrics: Modifying Molecular Symmetries and Homochirality. *Acc. Chem. Res.* **2019**, *52*, 1928−1938.
(29) Baudry, L.; Lukyanchuk, I.; Vinokur, V. M. Ferroelectric symmetry-protected multibit memory cell. *Sci. Rep.* **2017**, *7*, 42196.
(30) Timmermans, J. Plastic crystals: A historical review. *J. Phys. Chem. Solids* **1961**, *18*, 1−8.
(31) Ishida, H.; Iwachido, T.; Hayama, N.; Ikeda, R.; Hashimoto, M.; Nakamura, D. Structural Phase Transitions in Solid tert-Butylammonium Nitrate as Studied by Differential Thermal Analysis and $^1$H-NMR. *Z. Naturforsch. A* **1989**, *44*, 71−74.
(32) Pringle, J. M. Recent progress in the development and use of organic ionic plastic crystal electrolytes. *Phys. Chem. Chem. Phys.* **2013**, *15*, 1339−1351.
(33) Wei, Z.-H.; Jiang, Z.-T.; Zhang, X.-X.; Li, M.-L.; Tang, Y.-Y.; Chen, X.-G.; Cai, H.; Xiong, R.-G. Rational Design of Ceramic-Like Molecular Ferroelectric by Quasi-Spherical Theory. *J. Am. Chem. Soc.* **2020**, *142*, 1995−2000.
(34) Mondal, A.; Bhattacharya, B.; Das, S.; Bhunia, S.; Chowdhury, R.; Dey, S.; Reddy, C. M. Metal-like Ductility in Organic Plastic Crystals: Role of Molecular Shape and Dihydrogen Bonding Interactions in Aminoboranes. *Angew. Chem., Int. Ed.* **2020**, *59*, 10971−10980.
(35) Saha, S.; Mishra, M. K.; Reddy, C. M.; Desiraju, G. R. From Molecules to Interactions to Crystal Engineering: Mechanical Properties of Organic Solids. *Acc. Chem. Res.* **2018**, *51*, 2957−2967.
(36) Olejniczak, A.; Anioła, M.; Szafrański, M.; Budzianowski, A.; Katrusiak, A. New Polar Phases of 1,4-Diazabicyclo[2.2.2]octane Perchlorate, An $NH^+\cdots N$ Hydrogen-Bonded Ferroelectric. *Cryst. Growth Des.* **2013**, *13*, 2872−2879.
(37) Olejniczak, A.; Szafrański, M.; Katrusiak, A. Pressure−Temperature Phase Diagrams and Transition Mechanisms of Hybrid Organic−Inorganic NH··· N Bonded Ferroelectrics. *Cryst. Growth Des.* **2018**, *18*, 6488−6496.
(38) Harada, J.; Kawamura, Y.; Takahashi, Y.; Uemura, Y.; Hasegawa, T.; Taniguchi, H.; Maruyama, K. Plastic/Ferroelectric Crystals with Easily Switchable Polarization: Low-Voltage Operation, Unprecedentedly High Pyroelectric Performance, and Large Piezoelectric Effect in Polycrystalline Forms. *J. Am. Chem. Soc.* **2019**, *141*, 9349−9357.
(39) Cohen, R. E. Origin of ferroelectricity in perovskite oxides. *Nature* **1992**, *358*, 136−138.
(40) Ai, Y.; Wu, D.-J.; Yang, M.-J.; Wang, P.; He, W.-H.; Liao, W.-Q. Highest-Tc organic enantiomeric ferroelectrics obtained by F/H substitution. *Chem. Commun.* **2020**, *56*, 7033−7036.
(41) Tang, Y.-Y.; Xie, Y.; Ai, Y.; Liao, W.-Q.; Li, P.-F.; Nakamura, T.; Xiong, R.-G. Organic Ferroelectric Vortex−Antivortex Domain Structure. *J. Am. Chem. Soc.* **2020**, *142*, 21932−21937.
(42) Groom, C. R.; Bruno, I. J.; Lightfoot, M. P.; Ward, S. C. The Cambridge Structural Database. *Acta Crystallogr., Sect. B: Struct. Sci., Cryst. Eng. Mater.* **2016**, *72*, 171−179.
(43) Seyedraoufi, S.; Sødahl, E. D.; Görbitz, C. H.; Berland, K. Database mining and first-principles assessment of organic proton-transfer ferroelectrics. **2023**, arXiv:2306.00363.
(44) All structure and molecule figures are made using the software programs Mercury96 and VESTA.97

(45) Berland, K.; Sødahl, E. D.; Seyedraoufi, S. Molcrys, 2023. https://gitlab.com/m7582/molcrys/.
(46) Hjorth Larsen, A.; Jørgen Mortensen, J.; Blomqvist, J.; Castelli, I. E.; Christensen, R.; Dułak, M.; Friis, J.; Groves, M. N.; Hammer, B.; Hargus, C.; Hermes, E. D.; Jennings, P. C.; Bjerre Jensen, P.; Kermode, J.; Kitchin, J. R.; Leonhard Kolsbjerg, E.; Kubal, J.; Kaasbjerg, K.; Lysgaard, S.; Bergmann Maronsson, J.; Maxson, T.; Olsen, T.; Pastewka, L.; Peterson, A.; Rostgaard, C.; Schiøtz, J.; Schütt, O.; Strange, M.; Thygesen, K. S.; Vegge, T.; Vilhelmsen, L.; Walter, M.; Zeng, Z.; Jacobsen, K. W. The atomic simulation environment—a python library for working with atoms. *J. Condens. Matter Phys.* **2017**, *29*, 273002.
(47) Hagberg, A.; Swart, P.; Chult, D. S. *Exploring Network Structure, Dynamics, and Function Using Networkx*, 2008.
(48) André, D.; Dworkin, A.; Szwarc, H.; Céolin, R.; Agafonov, V.; Fabre, C.; Rassat, A.; Straver, L.; Bernier, P.; Zahab, A. Molecular packing of fullerene $C_{60}$ at room temperature. *Mol. Phys.* **1992**, *76*, 1311−1317.
(49) Jenkins, T. E.; Lewis, J. A Raman study of adamantane (C10H16), diamantane (C14H20) and triamantane (C18H24) between 10 K and room temperatures. *Spectrochim. Acta, Part A* **1980**, *36*, 259−264.
(50) Szewczyk, D.; Jeżowski, A.; Krivchikov, A. I.; Tamarit, J. L. Influence of thermal treatment on thermal properties of adamantane derivatives. *Low Temp. Phys.* **2015**, *41*, 469−472.
(51) Bruno, I. J.; Cole, J. C.; Edgington, P. R.; Kessler, M.; Macrae, C. F.; McCabe, P.; Pearson, J.; Taylor, R. New software for searching the Cambridge Structural Database and visualizing crystal structures. *Acta Crystallogr., Sect. B: Struct. Sci.* **2002**, *58*, 389−397.
(52) Kresse, G.; Hafner, J. Ab initio molecular-dynamics simulation of the liquid-metal−amorphous-semiconductor transition in germanium. *Phys. Rev. B: Condens. Matter Mater. Phys.* **1994**, *49*, 14251−14269.
(53) Kresse, G.; Hafner, J. Ab initio molecular dynamics for liquid metals. *Phys. Rev. B: Condens. Matter Mater. Phys.* **1993**, *47*, 558−561.
(54) Kresse, G.; Furthmüller, J. Efficiency of ab-initio total energy calculations for metals and semiconductors using a plane-wave basis set. *Comput. Mater. Sci.* **1996**, *6*, 15−50.
(55) Kresse, G.; Furthmüller, J. Efficient iterative schemes for *ab initio* total-energy calculations using a plane-wave basis set. *Phys. Rev. B: Condens. Matter Mater. Phys.* **1996**, *54*, 11169−11186.
(56) Blöchl, P. E. Projector augmented-wave method. *Phys. Rev. B: Condens. Matter Mater. Phys.* **1994**, *50*, 17953−17979.
(57) Kresse, G.; Joubert, D. From ultrasoft pseudopotentials to the projector augmented-wave method. *Phys. Rev. B: Condens. Matter Mater. Phys.* **1999**, *59*, 1758−1775.
(58) Resta, R. Macroscopic polarization in crystalline dielectrics: the geometric phase approach. *Rev. Mod. Phys.* **1994**, *66*, 899−915.
(59) Baroni, S.; Resta, R. *Ab initio* calculation of the macroscopic dielectric constant in silicon. *Phys. Rev. B: Condens. Matter Mater. Phys.* **1986**, *33*, 7017−7021.
(60) Berland, K.; Hyldgaard, P. Exchange functional that tests the robustness of the plasmon description of the van der Waals density functional. *Phys. Rev. B: Condens. Matter Mater. Phys.* **2014**, *89*, 035412.
(61) Harada, J.; Yoneyama, N.; Yokokura, S.; Takahashi, Y.; Miura, A.; Kitamura, N.; Inabe, T. Ferroelectricity and piezoelectricity in free-standing polycrystalline films of plastic crystals. *J. Am. Chem. Soc.* **2018**, *140*, 346−354.
(62) Chen, X.-G.; Song, X.-J.; Zhang, Z.-X.; Zhang, H.-Y.; Pan, Q.; Yao, J.; You, Y.-M.; Xiong, R.-G. Confinement-Driven Ferroelectricity in a Two-Dimensional Hybrid Lead Iodide Perovskite. *J. Am. Chem. Soc.* **2020**, *142*, 10212−10218.
(63) Szafrański, M.; Katrusiak, A.; McIntyre, G. J. Ferroelectric Order of Parallel Bistable Hydrogen Bonds. *Phys. Rev. Lett.* **2002**, *89*, 215507.
(64) Tang, Y.-Y.; Zhang, W.-Y.; Li, P.-F.; Ye, H.-Y.; You, Y.-M.; Xiong, R.-G. Ultrafast polarization switching in a biaxial molecular ferroelectric thin film: [Hdabco]ClO4. *J. Am. Chem. Soc.* **2016**, *138*, 15784−15789.
(65) Budzianowski, A.; Katrusiak, A. Anomalous Protonic-Glass Evolution from Ordered Phase in NH ··· N Hydrogen-Bonded DabcoHBF4 Ferroelectric. *J. Phys. Chem. B* **2008**, *112*, 16619−16625.
(66) Ye, H.-Y.; Tang, Y.-Y.; Li, P.-F.; Liao, W.-Q.; Gao, J.-X.; Hua, X.-N.; Cai, H.; Shi, P.-P.; You, Y.-M.; Xiong, R.-G. Metal-free three-dimensional perovskite ferroelectrics. *Science* **2018**, *361*, 151−155.
(67) Siczek, M.; Lis, T. (*R*)-(−)-3-Hydroxyquinuclidinium chloride. *Acta Crystallogr., Sect. E: Struct. Rep. Online* **2008**, *64*, 842.
(68) Li, P.-F.; Tang, Y.-Y.; Wang, Z.-X.; Ye, H.-Y.; You, Y.-M.; Xiong, R.-G. Anomalously rotary polarization discovered in homochiral organic ferroelectrics. *Nat. Commun.* **2016**, *7*, 13635.
(69) Li, P.-F.; Liao, W.-Q.; Tang, Y.-Y.; Qiao, W.; Zhao, D.; Ai, Y.; Yao, Y.-F.; Xiong, R.-G. Organic enantiomeric high- $T_c$ ferroelectrics. *Proc. Natl. Acad. Sci. U.S.A.* **2019**, *116*, 5878−5885.
(70) Zhang, Y.; Hopkins, M. A.; Liptrot, D. J.; Khanbareh, H.; Groen, P.; Zhou, X.; Zhang, D.; Bao, Y.; Zhou, K.; Bowen, C. R.; Carbery, D. R. Harnessing Plasticity in an Amine-Borane as a Piezoelectric and Pyroelectric Flexible Film. *Angew. Chem., Int. Ed.* **2020**, *59*, 7808−7812.
(71) Shi, P.-P.; Ye, Q.; Li, Q.; Wang, H.-T.; Fu, D.-W.; Zhang, Y.; Xiong, R.-G. Novel Phase-Transition Materials Coupled with Switchable Dielectric, Magnetic, and Optical Properties: [(CH3)4P][FeCl4] and [(CH3)4P][FeBr4]. *Chem. Mater.* **2014**, *26*, 6042−6049.
(72) Szafrański, M. Strong negative thermal expansion and relaxor ferroelectricity driven by supramolecular patterns. *J. Mater. Chem. C* **2013**, *1*, 7904.
(73) Olejniczak, A.; Katrusiak, A.; Szafrański, M. Ten polymorphs of nh+ ··· n hydrogen-bonded 1,4-diazabicyclo[2.2.2]octane complexes: Supramolecular origin of giant anisotropic dielectric response in polymorph V. *Cryst. Growth Des.* **2010**, *10*, 3537−3546.
(74) Szafrański, M. Temperature-induced displacement of the proton site in strong f−h−f hydrogen bond and mechanism of phase transition in 1,4 diazabicyclo[2.2.2]octane dihydrogen difluoride. *Chem. Phys. Lett.* **2008**, *457*, 110.
(75) Bläsing, K.; Labbow, R.; Schulz, A.; Villinger, A. Silylated sulfuric acid: Preparation of a tris(trimethylsilyl)oxosulfonium [(me3si-o)3so]+ salt. *Angew. Chem., Int. Ed.* **2021**, *60*, 13798−13802.
(76) Krukau, A. V.; Vydrov, O. A.; Izmaylov, A. F.; Scuseria, G. E. Influence of the exchange screening parameter on the performance of screened hybrid functionals. *J. Chem. Phys.* **2006**, *125*, 224106.
(77) Maglione, M.; Philippot, G.; Levasseur, D.; Payan, S.; Aymonier, C.; Elissalde, C. Defect chemistry in ferroelectric perovskites: long standing issues and recent advances. *Dalton Trans.* **2015**, *44*, 13411−13418.
(78) Damjanovic, D. Ferroelectric, dielectric and piezoelectric properties of ferroelectric thin films and ceramics. *Rep. Prog. Phys.* **1998**, *61*, 1267−1324.
(79) Fu, D.-W.; Gao, J.-X.; He, W.-H.; Huang, X.-Q.; Liu, Y.-H.; Ai, Y. High-Tc Enantiomeric Ferroelectrics Based on Homochiral Dabco-derivatives (Dabco = 1,4-Diazabicyclo[2.2.2]octane). *Angew. Chem., Int. Ed.* **2020**, *59*, 17477−17481.
(80) Li, J.-Y.; Xu, Q.-L.; Ye, S.-Y.; Tong, L.; Chen, X.; Chen, L.-Z. A multiaxial molecular ferroelectric with record high $T_c$ designed by intermolecular interaction modulation. *Chem. Commun.* **2021**, *57*, 943−946.
(81) Yoneya, M.; Harada, J. Molecular Dynamics Simulation Study of the Plastic/Ferroelectric Crystal Quinuclidinium Perrhenate. *J. Phys. Chem. C* **2020**, *124*, 2171−2177.
(82) Lee, J.; Seol, W.; Anoop, G.; Samanta, S.; Unithrattil, S.; Ahn, D.; Kim, W.; Jung, G.; Jo, J. Stabilization of Ferroelectric Phase in Highly Oriented Quinuclidinium Perrhenate (HQReO4) Thin Films. *Materials* **2021**, *14*, 2126.
(83) Li, J. L.; Yang, G. W. Iron Endohedral-Doped Boron Fullerene: A Potential Single Molecular Device with Tunable Electronic and Magnetic Properties. *J. Phys. Chem. C* **2009**, *113*, 18292−18295.

(84) Ma, L.; He, H.; Yang, B.-F.; Zhang, Q.; Yang, G.-Y. [Pb(en)0.5][B5O8(OH)]: A New Bilayered Organic−Inorganic Hybrid Lead Borate Built by B5O8(OH) Cluster Units. *J. Cluster Sci.* **2015**, *26*, 1495−1502.
(85) Zhao, D.; He, X.; Li, M.; Wang, B.; Guo, C.; Rong, C.; Chattaraj, P. K.; Liu, S. Density functional theory studies of boron clusters with exotic properties in bonding, aromaticity and reactivity. *Phys. Chem. Chem. Phys.* **2021**, *23*, 24118−24124.
(86) Barba-Bon, A.; Salluce, G.; Lostalé-Seijo, I.; Assaf, K. I.; Hennig, A.; Montenegro, J.; Nau, W. M. Boron clusters as broadband membrane carriers. *Nature* **2022**, *603*, 637−642.
(87) Li, D.; Zhao, X.-M.; Zhao, H.-X.; Long, L.-S.; Zheng, L.-S. Coexistence of Magnetic-Optic-Electric Triple Switching and Thermal Energy Storage in a Multifunctional Plastic Crystal of Trimethylchloromethyl Ammonium Tetrachloroferrate(III). *Inorg. Chem.* **2019**, *58*, 655−662.
(88) Even, J.; Carignano, M.; Katan, C. Molecular disorder and translation/rotation coupling in the plastic crystal phase of hybrid perovskites. *Nanoscale* **2016**, *8*, 6222−6236.
(89) Létoublon, A.; Paofai, S.; Rufflé, B.; Bourges, P.; Hehlen, B.; Michel, T.; Ecolivet, C.; Durand, O.; Cordier, S.; Katan, C.; Even, J. Elastic Constants, Optical Phonons, and Molecular Relaxations in the High Temperature Plastic Phase of the $CH_3NH_3PbBr_3$ Hybrid Perovskite. *J. Phys. Chem. Lett.* **2016**, *7*, 3776−3784.
(90) Shang, Y.; Sun, L.-y.; Ye, Z.-m.; Chen, S.-l.; Zhang, W.-x.; Chen, X.-m. Phase transition and thermal expansion of molecular perovskite energetic crystal (C6N2H14)(NH4)(ClO4)3 (DAP-4). *FirePhysChem* **2022**, *2*, 221−225.
(91) Staveley, L. A. K. Phase transitions in plastic crystals. *Annu. Rev. Phys. Chem.* **1962**, *13*, 351−368.
(92) Li, P.-F.; Tang, Y.-Y.; Liao, W.-Q.; Ye, H.-Y.; Zhang, Y.; Fu, D.-W.; You, Y.-M.; Xiong, R.-G. A semiconducting molecular ferroelectric with a bandgap much lower than that of BiFeO3. *NPG Asia Mater.* **2017**, *9*, No. e342.
(93) Bai, Y.; Jantunen, H.; Juuti, J. Energy Harvesting Research: The Road from Single Source to Multisource. *Adv. Mater.* **2018**, *30*, 1707271.
(94) Liu, H.-Y.; Zhang, H.-Y.; Chen, X.-G.; Xiong, R.-G. Molecular Design Principles for Ferroelectrics: Ferroelectrochemistry. *J. Am. Chem. Soc.* **2020**, *142*, 15205−15218.
(95) Lin, J.-H.; Lou, J.-R.; Ye, L.-K.; Hu, B.-L.; Zhuge, P.-C.; Fu, D.-W.; Su, C.-Y.; Zhang, Y. Halogen Engineering To Realize Regulable Multipolar Axes, Nonlinear Optical Response, and Piezoelectricity in Plastic Ferroelectrics. *Inorg. Chem.* **2023**, *62*, 2870−2876.

Paper IV

# Engineering new organic proton-transfer acid-base (anti-)ferroelectric salts using crystal structure prediction

**Seyedmojtaba Seyedraoufi, Graeme M. Day, Kristian Berland**

Manuscript.

IV

# Engineering new organic proton-transfer acid-base (anti-)ferroelectric salts using crystal structure prediction

S. Seyedraoufi,[1] Graeme M. Day,[2] and Kristian Berland[1]

[1]*Department of Mechanical Engineering and Technology Management, Norwegian University of Life Sciences, 1432 Ås, Norway.*
[2]*School of Chemistry, University of Southampton, Southampton SO17 1BJ, United Kingdom.*

(Dated: December 12, 2023)

Organic molecular ferroelectrics, including organic proton-transfer ferroelectrics (OPTFes), offer potential properties such as flexibility and biocompatibility, expanding their potential application scope. Among these, acid-base salts, a subset of OPTFes, enable the tuning of ferroelectric properties using different acid-base combinations. This study focuses on designing novel acid-based OPTFes with higher polarization than existing ones by combining smaller acid and base molecular units. 6 acid and 5 base molecules were selected with functional groups that cover a wide range of electronegativity. For each of the molecular combinations, the crystal structure prediction (CSP) method was employed to predict the packing of the crystal. In our CSP analysis, in addition to the monovalent salt, which is the desired state for showing ferroelectricity, the other competing divalent salt and neutral states were also assessed. After evaluations of CSP landscapes, three ferroelectric and two antiferroelectric candidates were identified. The calculated polarizations exceed those of previously reported acid-base OPTFes, highlighting the potential of the proposed approach in designing novel organic ferroelectrics with improved performance.

## I. INTRODUCTION

Ferroelectrics are an attractive class of materials due to their diverse technological applications, including capacitors, sensors, actuators, and memory devices.[1] The vast array of applications arises from the response of ferroelectric materials and their spontaneous polarization ($\boldsymbol{P}_s$) to changes in external stimuli, including thermal, electrical, and mechanical forces.[2] Similarly, antiferroelectrics have attracted attention due to their large energy storage properties.[3] Organic ferroelectrics, including organic proton-transfer ferroelectrics (OPTFes) are free of heavy elements and their potential to be integrated into flexible substrates and low-cost fabrication makes them attractive candidates for various future electronic and optoelectronic devices.[4–8]

One category of OPTFes is the acid-base salts, where the switchability of $\boldsymbol{P}_s$ is achieved through the transfer of protons between molecules with acid and base moieties. Compared to the tautomeric OPTFes[6], acid-base salts have lower $\boldsymbol{P}_s$ and coercive fields, which limits their applications in high-voltage electronics. However, the presence of two distinct molecular types in the unit cell allows for crystal engineering by substituting the molecules to enhance the properties. Predicting the structure of acid-base salts after molecular substitution can be challenging. This relates to the specific hydrogen-bonded synthon of the OPTFe crystals, which extends throughout the entire crystal and mediates proton transfer (PT). An example is the neutral co-crystal of bromanilic acid and pyrazine,[9] in which pyrazine and bromanilic acid are connected through a hydrogen-bonded network. Substituting pyrazine with tetramethyl pyrazine not only changed the space group but also disturbed the acid-base-connected hydrogen-bonded pattern.[10] Thus, for each new molecular combination, a step to predict the potential solid-state packing is necessary.

Crystal structure prediction (CSP) entails predicting the three-dimensional arrangement of molecules or atoms from their basic constituents.[11,12] CSP typically involves exploring the multidimensional crystal structure configurational space through efficient sampling methods that ideally encompass all local minima. Each of the local minima is a possible stable crystal structure, and a subsequent energy minimization is needed to rank the structures.[13,14] A preliminary CSP landscape can be generated by applying low-level empirical or semi-empirical force fields. For molecular crystals, higher-level ab initio methods, usually density functional theory (DFT) are employed for a limited number of low-energy structures.[12,15] A successful CSP method should re-rank "true" crystal structure and possible polymorphs in the region close to the global minimum.

This study aims to develop and apply a systematic framework for engineering novel acid-base OPTFes using CSP to predict the packing of modified structures. So far, realized compounds are the derivatives of haloanilic acid combined with derivatives of large phenazine or bipyridine rings as the proton acceptors.[2,16–18] One design target is to enhance the density of PT hydrogen bonds within crystals and, consequently, polarization strength. This can be achieved by replacing the large proton acceptors with smaller single-ring molecules. However, this replacement changes the effective protonation energy and crystal packing, necessitating a full CSP evaluation. To implement this, we systematically evaluated 30 novel combinations of acid and base molecules across multiple stages, ensuring the optimal anti/ferroelectric packing with respect to space

group symmetry, protonation state, and PT pathway. Ultimately, we calculated $\boldsymbol{P}_s$ of the predicted ferroelectric structures, using DFT.

## II. METHODS

### A. CSP

To generate crystal structures, we employed the Global Lattice Energy Explorer (GLEE) package,[19] using the Sobol quasi-random method[20] to sample the configurational space. This includes lattice parameters as well as the positions and orientations of rigid molecules. The energy minimization of the structures was carried out using the Buckingham-type atomistic potential with dispersion and repulsion terms implemented in DMACRYS.[21] The interatomic parameters are derived from a study that fitted the potential to the experimental data of a set of organic molecular crystals with chemical compositions similar to our study, referred to as the FIT potential in this study.[22] Moreover, the potential incorporates electrostatic interactions, taking into account atom-centered multipoles up to rank 4. These multipoles were generated through a distributed multipole analysis[23] of the charge density obtained at the B3LYP/6-311G** level using PSI4 program.[24] The optimization of the lattice energy considered the positions and orientations of rigid molecules within the crystal space group symmetry. During the structure generation and energy minimization steps, structures with non-physical packing, such as overlapping molecules and/or non-physical energies, were removed.

The generated crystals belong to the ten most common space groups for co-crystals, consisting of $P_1$, $P_{-1}$, $P2_1/c$, $C2/c$, $P2_1$, $P2_12_12_1$, $Pbca$, $Pna2_1$, $C2$, and $Cc$. Additionally, we considered the common space groups observed for OPTFe crystals, such as $P2/c$, $Pca2_1$, $Pnn2$, $Pccn$, $Fdd2$, $Iba2$, $P2$, $H3$, $P6_1$, and $I4_1/a$.[2,5,6,16–18,25,26] The criteria for terminating the quasi-random generation of crystal structures were either reaching 20,000 structures or observing no change in the number of generated structures after a minimum of 100,000 attempts to generate a new structure. Duplicate structures were removed from the final set of structures by evaluating the similarity of their simulated powder X-ray diffraction patterns generated with PLATON.[27]

To assess the similarity of crystal structures, we utilized the COMPACK algorithm.[28,29] This method involves comparing interatomic distance patterns that originate from a central molecule within a predefined molecular cluster. Once the best match is identified, the method aligns a cluster of molecules by minimizing interatomic distances. Here, a cluster of 30 molecules was employed, denoted as $\mathrm{COMPACK}^{30}$. While aligning the molecules, a 30 % distance tolerance and a 30° angle tolerance were allowed. The degree of similarity is quantified by the number of overlapping molecules in the cluster.

### B. Co-crystal design

The co-crystal design involves combining single-ring molecular compounds capable of forming an infinite PT hydrogen-bonded network with the potential to switch the polarization of the crystal, referred to here as the "connected PT path". To ensure the bistability of the ferroelectric compound, it is essential that both haloanilic acid molecules and nitrogen-containing heterocyclic compounds, like phenazine, possess equivalent sites on both ends for donating and accepting protons. Using the Cambridge Structural Database (CSD),[29,30] we identified all one-ring molecules with equivalent nitrogen or oxygen sites. To limit the size of the molecules, we included only compounds with methyl, flour, cyano, and hydroxyl functional groups. These criteria were implemented using ConQuest in combination with the MOLCRYS Python package[31].

Fig. 1 shows the list of acid and base molecules used in the design. The desired OPTFe structure takes the form of a monovalent salt (MS), competing with both neutral co-crystal (NC) and divalent salt (DS) configurations. Performing CSP for all the molecular combinations and their protonation states requires $6 \times 5 \times 3$ CSP calculations. To limit the number, we considered the "template packing" step, in which the three possible protonation states of a given molecular combination were assessed in only one template packing. As depicted in Fig. 1, to accommodate molecules with smaller functional groups such as DFAN, DCAN, PZ, and DFPZ, we adopted a tighter packing arrangement with the $P_1$ space group. Conversely, for larger molecules, a looser packing was employed with the $Pc$ space group. However, since different packings can also affect the protonation states of molecular crystals,[32] we only used this step to exclude molecular combinations where the MS polar template packing is unstable and does not constitute a local minimum. Such combinations in their MS state are unlikely to be the preferred structure for other packings. CSP calculations were performed for the successful molecular combinations. In the subsequent step, the 100 lowest structures from the global minima of the CSP landscape, generated by the FIT potential, were re-ranked using single-point DFT energies divided by the number of acid-base pairs in the unit cell. Molecular combinations where the low-energy region was only dominated by NC structures (energy gap $> 0.2$ eV) were excluded from further evaluation. Subsequently, full DFT relaxation is employed for the remaining combinations.

### C. Density functional theory calculations

DFT calculations were performed employing the projector augmented wave (PAW) approach, as imple-

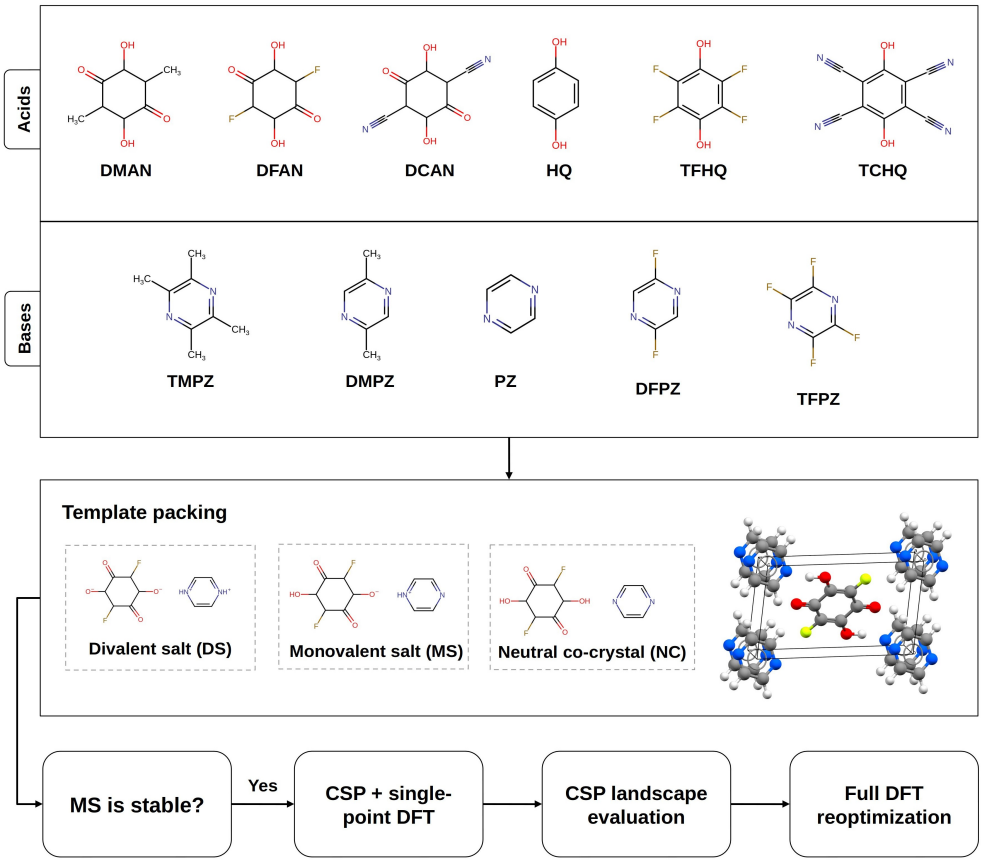


FIG. 1: The workflow of the OPTFe salts design. The acid and base molecules used in the design are: **Dim**ethyl **an**ilic acid (DMAN), **di**flouro **an**ilic acid (DFAN), **di**cyano **an**ilic acid (DCAN), **h**ydro**qu**inone (HQ), **t**etra**f**louro **h**ydro**qu**inone (TFHQ), **t**etra**c**yano **h**ydro**qu**inone (TCHQ), **t**etra**m**ethyl **p**yra**z**ine (TMPZ), **dim**ethyl **p**yra**z**ine (DMPZ), **p**yra**z**ine (PZ), **di**flouro **p**yra**z**ine (DFPZ), **t**etra**f**louro **p**yra**z**ine (TFPZ).

mented in the VASP software suite,[33–35] utilizing PAW pseudopotentials. A plane-wave energy cutoff of 530 eV was adopted, which converged the energy difference per acid-base pairs between two competing structures on the CSP within 5 meV. The second version of the van der Waals density function (vdW-DF2) was chosen since it can accurately predict lattice parameters of the OPTFes systems.[36] Sampling of the Brillouin zone was performed using a Γ-centered Monkhorst-Pack grid with a spacing of $(1/25)$ Å$^{-1}$. The self-consistency iteration loop was pursued until energy differences reached values below $10^{-8}$ eV. Simultaneously, the iterative loop for ionic relaxation was stopped when the norm of all atomic forces reached below 0.01 eV/Å. The $\boldsymbol{P}_s$ values were computed using the Berry-phase method.[37–39]

## III. RESULTS AND DISCUSSION

### A. CSP validation

To validate the ability of CSP to reliably predict the experimental crystal structure of acid-base salts, we performed two case studies for the phenazinium chloranilate (CSD refcode: MAMPUM03),[16] and 2,3,5,6-tetrafluorobenzene-1,4-diol quinoxaline (CSD refcode: QUWZIS). MAMPUM03 is a known acid-base OPTFe crystallizing in the $P2_1$ space group, with a phase transition to a paraelectric NC phase (MAMPUM04) with the $P2_1/n$ space group at 253 K.[40] The other system, QUWZIS, is a hydrogen-bonded co-crystal with the $P2_12_12_1$ space group and was selected because of its

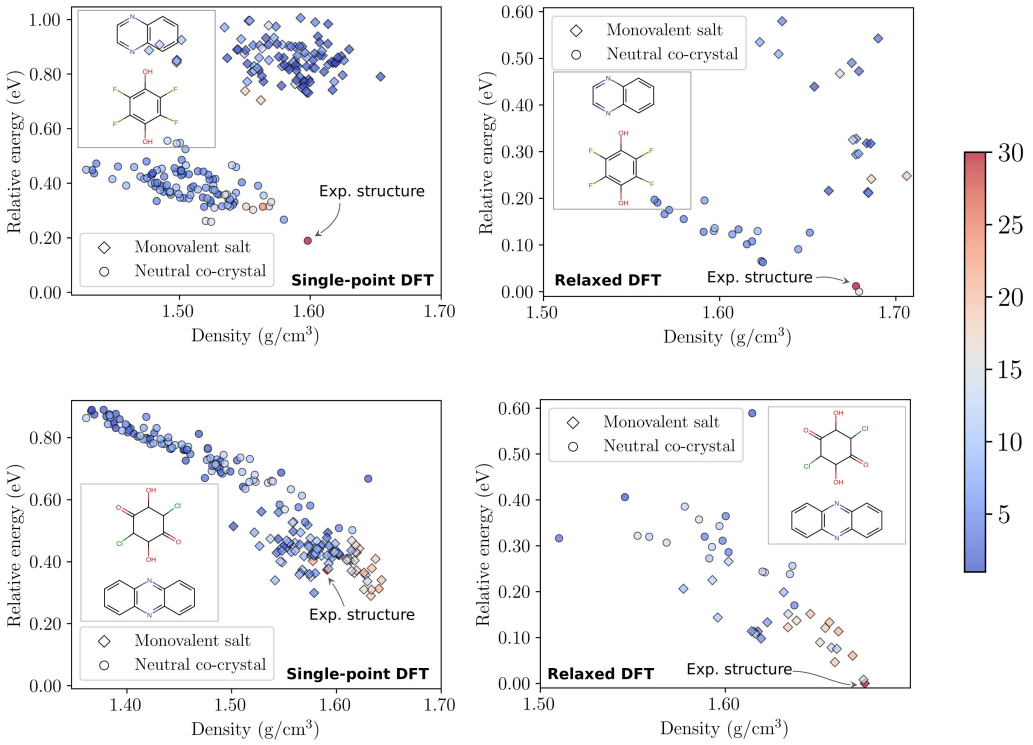


FIG. 2: The CSP landscapes for 2,3,5,6-tetrafluorobenzene-1,4-diol quinoxaline (upper panel) and phenazinium chloranilate (lower panel) are plotted using single-point DFT and relaxed DFT energies, respectively. The color map demonstrates the similarity of the structures to the experimental structure using the COMPAK$_{30}$ algorithm.

similarity to the designed co-crystals used in this study.

Fig. 2 displays the CSP landscape generated at two levels of accuracy for MAMPUM03 and QUEZIS co-crystal. Single-point DFT energy evaluation was performed for the lowest 100 structures from the global minimum of the FIT CSP landscape. As shown in the upper panel, for QUWZIS, FIT, and subsequently single-point DFT successfully identified the experimental structure as the global minimum. In the next stage, the 20 lowest-energy structures from the single-point DFT energy landscape were fully relaxed. The experimental structure is now ranked 2nd; however, the global minimum is a structure with high similarity to the experimental structure. More importantly, the lowest-energy structure also exhibits a connected PT path, a non-polar space group, and neutrality, distinguishing between anti/ferroelectric and non-anti/ferroelectric crystals. In the case of MAMPUM03, the crystal structure was ranked 20th on the single-point DFT landscape, as is evident from the lower panel. However, on the DFT landscape using relaxed DFT energies, the experimental structure is now found in the global minimum. Further, the competing structure is similar to the experimental one; both structures consist of four molecules in the asymmetric unit, forming two hydrogen-bonded supramolecular chains responsible for PT pathways. The distinction lies in the orientation of the dipole within the PT chains and a slight positional shift of these chains relative to each other.

### B. Template packing

As detailed in the Sec. II B, different protonation states of molecular combinations were evaluated at the vdW-DF2 level using template packings. The upper panel of Fig. 3 shows a two-dimensional histogram of different possible combinations of acid and base molecules, where the color mapping depicts the electronic ground state energy differences divided by the number of acid-base pairs in the unit cell between MS and NC $\Delta E_{\mathrm{DFT}}^{\mathrm{MS,NC}} = E_{\mathrm{DFT}}^{\mathrm{MS}} - E_{\mathrm{DFT}}^{\mathrm{NC}}$. The combinations with dif-

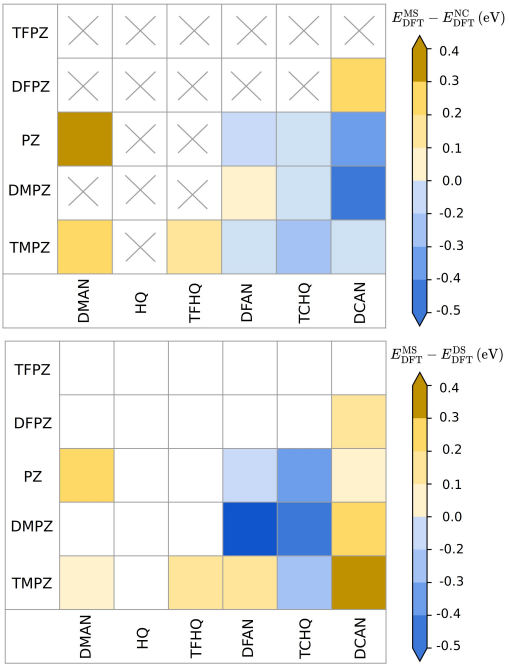


FIG. 3: In the upper panel, the energy difference of MS and NC contour is plotted for different molecular combinations. In the lower panel, the energy difference is plotted between MS and DS .

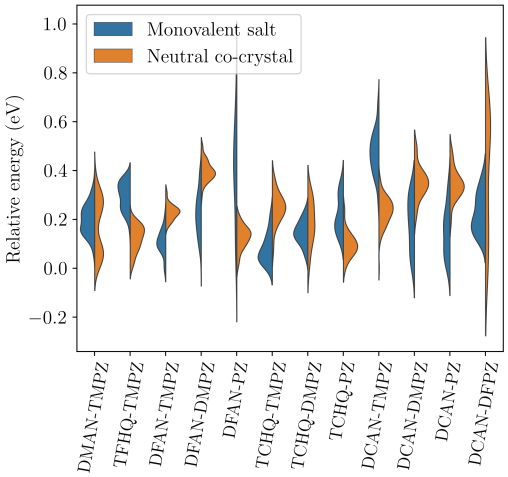


FIG. 4: Energy distribution of MS and NC structures generated by CSP using single-point DFT energies for the molecular combinations that successfully passed the template packing step.

ferent shades of blue color are the optimum ones with a more stable MS packing $\Delta E^{\mathrm{MS,NC}}_{\mathrm{DFT}} < 0$. The systems in which the MS packing is dynamically unstable are marked by the $\times$ sign. As expected, most of the blue colors appear in the lower right part of the plot. This area represents acid molecules with very electron-withdrawing substituents like the cyano group in DCAN and TCHQ, as well as bases with electron-donating groups like methyl in DMPZ and TMPZ. We also noticed that HQ and TFHQ do not exhibit the same proton-donating capabilities as anilic acid molecules like DFAN, even when four fluorine atoms are added to the hydroquinone molecule.

In the next step, the stable MS structures were compared with their DS counterparts. In the lower panel of Fig. 3, a similar plot shows the difference between MS and DS, $\Delta E^{\mathrm{MS,DS}}_{\mathrm{DFT}} = E^{\mathrm{MS}}_{\mathrm{DFT}} - E^{\mathrm{DS}}_{\mathrm{DFT}}$. It is evident that the molecular combinations associated with DCAN exhibit a tendency to donate both of their protons rather than just one. This observation is consistent with our earlier finding that anilic acid rings tend to be more acidic compared to hydroquinone rings.

As a result of the template packing evaluation, 17 out of 30 molecular combinations exhibited dynamically unstable MS packing and were excluded from proceeding to the next stage for CSP evaluation. While DMAN-PZ demonstrates stable MS packing, its neutral form is significantly more stable. Therefore, it can be safely excluded from further CSP evaluations.

### C. CSP of compounds with stable MS

#### 1. *CSP using single-point DFT energies*

Fig. 4 shows the distribution of MS and NC structures obtained from CSP calculations followed by a single-point DFT energy evaluation. In the cases of TFHQ-TMPZ, DCAN-TMPZ, and DCAN-DFPZ, most of the low-energy structures are NCs. MS structures shifted around 0.2 eV from the global minima. This energy gap is large enough to make it impossible for any MS structures to reach the global minimum during a full DFT relaxation. This conclusion is drawn from the analysis of energies in our CSP landscapes in the validation stage, indicating that the structures, on average, are displaced by 0.04 eV on the CSP landscape after relaxation compared to the single-point DFT energies. Thus, we excluded them from further investigations.

Conversely, for half of the molecular combinations, MS structures have a higher distribution density in the low-energy region compared to the NCs. This observation holds true for DFAN-TMPZ, DFAN-DMPZ, TCHQ-TMPZ, DCAN-DMPZ, DCAN-PZ, and DCAN-

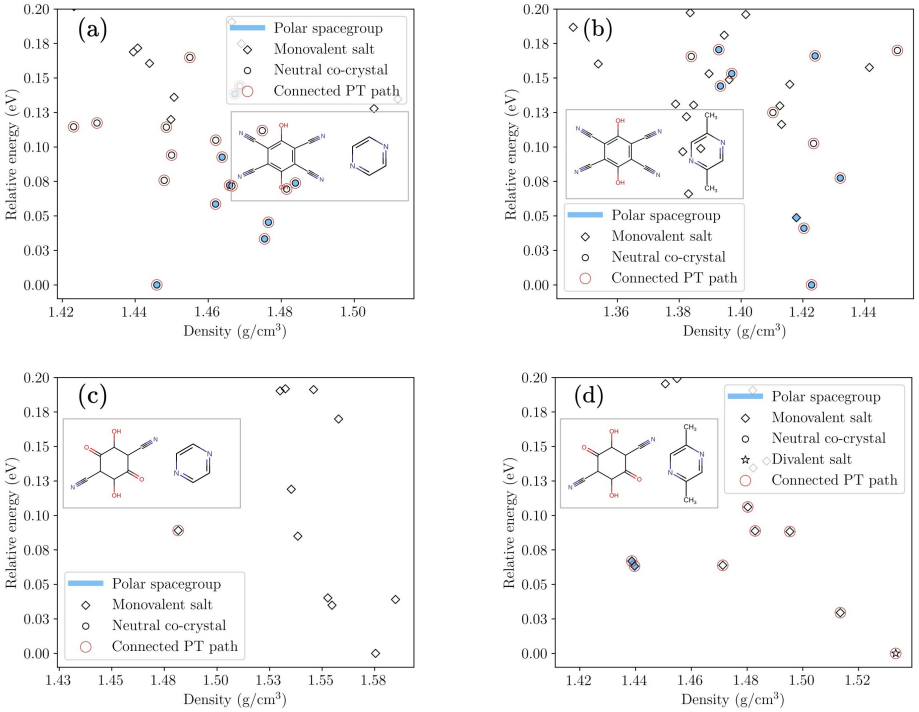


FIG. 5: The CSP landscapes for (a) TCHQ-PZ, (b) TCHQ-DMPZ, (c) DCAN-PZ, and (d) DCAN-DMPZ molecular combinations are plotted using relaxed structures DFT energies.

DFPZ. For the remaining structures, a mixture of MS and NC structures populates the low-energy regions, which, combined with the above six molecular combinations, were selected for a full DFT relaxation step.

The results in this section are consistent with $\Delta E_{\mathrm{DFT}}^{\mathrm{MS,NC}}$ energy evaluation in the template packing, except for DFAN-DMPZ and DCAN-TMPZ where NC and MS were more stable respectively.

The single-point DFT energy landscapes are also interesting from a design perspective based on chemical intuition. This implies that for the majority of our acid and base combinations, enhancing the acidity and/or basicity of the molecules caused a shift in the density of the MS structures to the lower-energy region on the CSP landscape compared to the NC structures, and vice versa. However, DCAN-TMPZ does not follow this rule, indicating that for highly acidic and basic combinations where DS is more stable, the order of stability for NC and MS might change.

### 2. *CSP using relaxed DFT energies*

Out of the nine molecular combinations selected for further investigation using relaxed DFT energies, four showed no anti/ferroelectric structure in the global minimum. Fig. 5 shows the CSP landscape of these combinations. Panel (a) displays the landscape of TCHQ-DMPZ, where an NC structure with a polar space group is in the global minimum, with more than a 0.05 eV distance from the closest MS structure. The same occurs with TCHQ-PZ, depicted in panel (b), where an NC structure with a large energy gap from MS structures resides in the global minimum. The closest MS, which is ranked 17th on the landscape, does not exhibit any connected PT path and is not packed in a polar space group. The packing arrangement in this structure involves a specific supramolecular synthon, with the negatively charged side of TCHQ forming bonds with the positively charged side of the PZ molecule, while the neutral hydroxyl (−OH) group of TCHQ forms a bond with the cyano group of another TCHQ molecule. Comparing (a) and (b), we observe that substituting pyrazine with methyl pyrazine has reduced the energy of MS struc-

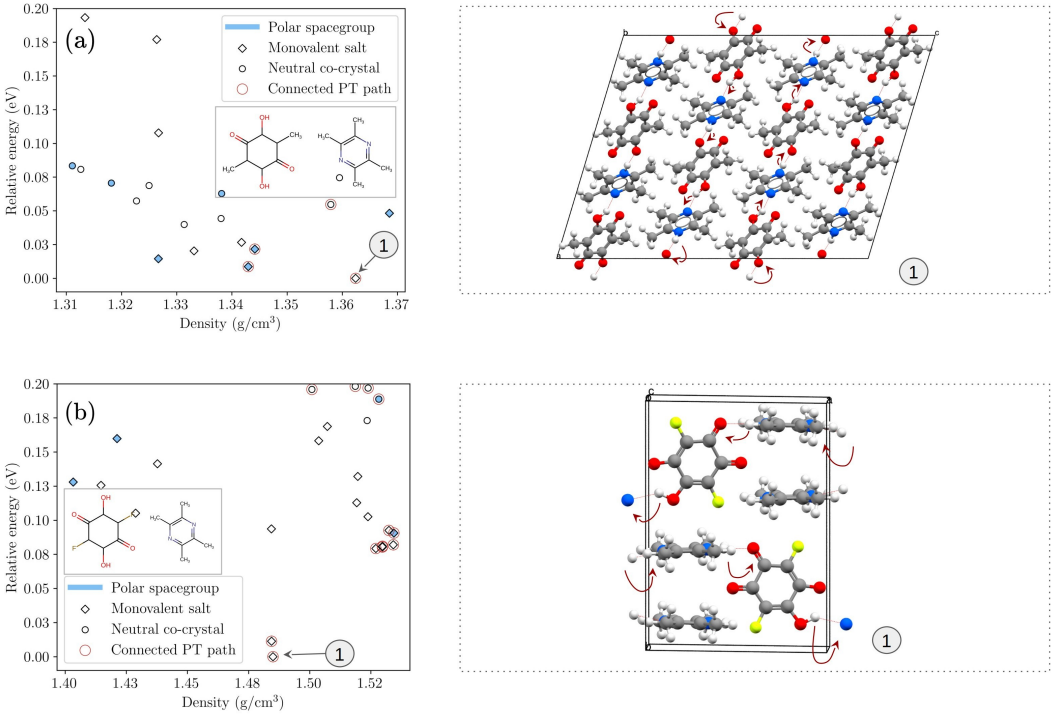


FIG. 6: The CSP landscapes for (a) DMAN-TMPZ and (b) DFAN-TMPZ molecular combinations are plotted using relaxed structures DFT energies.

tures on the energy landscape. However, none of the MS structures exhibit connected PT paths. In contrast, all the low-energy NC structures display connected PT paths, and the substitution has not altered this hydrogen bond pattern.

In the case of DCAN-DMPZ (panel (c)), an MS without any connected path was found at the global minimum. However, our template packing study (lower panel of Fig. 3) suggested that the DS form of this molecular combination could be more stable than the MS form. As a result, we added the energy of the DS form of the structure in the global minimum to the landscape, which now represents the new global minimum.

Finally, panel (d) shows the CSP landscape of DCAN-PZ, where an MS structure without any PT connected path is in the global minimum, with around a 0.10 eV energy gap from the closest MS structure with a connected PT path. Comparing (c) and (d), it is evident that replacing methyl pyrazine with pyrazine has increased the number of MS with a connected PT path, which is important from a design perspective.

Two molecular combinations exhibit an MS structure with a connected PT path and a non-polar space group in the global minimum. These structures have the potential to be antiferroelectric crystals. Panel (a) of Fig. 6 shows the CSP landscape of DMAN-TMPZ, where the antiferroelectric candidate is in the global minimum with a small energy gap distance from an MS structure with a polar space group and connected PT path. Our structural inspection indicates that this structure can also potentially be a ferroelectric structure. The crystal structure of the antiferroelectric packing with parallel PT paths is also depicted in panel (a). Panel (b) shows another molecular combination, DFAN-TMPZ, where an MS structure with a non-polar space group and a connected PT path is in the global minimum. The antiferroelectric packing is also depicted, showing the anti-parallel PT paths.

Three molecular combinations exhibit an MS structure with a connected PT path and polar space group in the global minimum. these structures can be potential ferroelectric crystals. Panel (a) of Fig. 7 presents the CSP landscape of DFAN-PZ, where a ferroelectric candidate is found in the global minima. However, most of the low-energy structures near the global minimum are NCs with connected PT paths, and the closest struc-

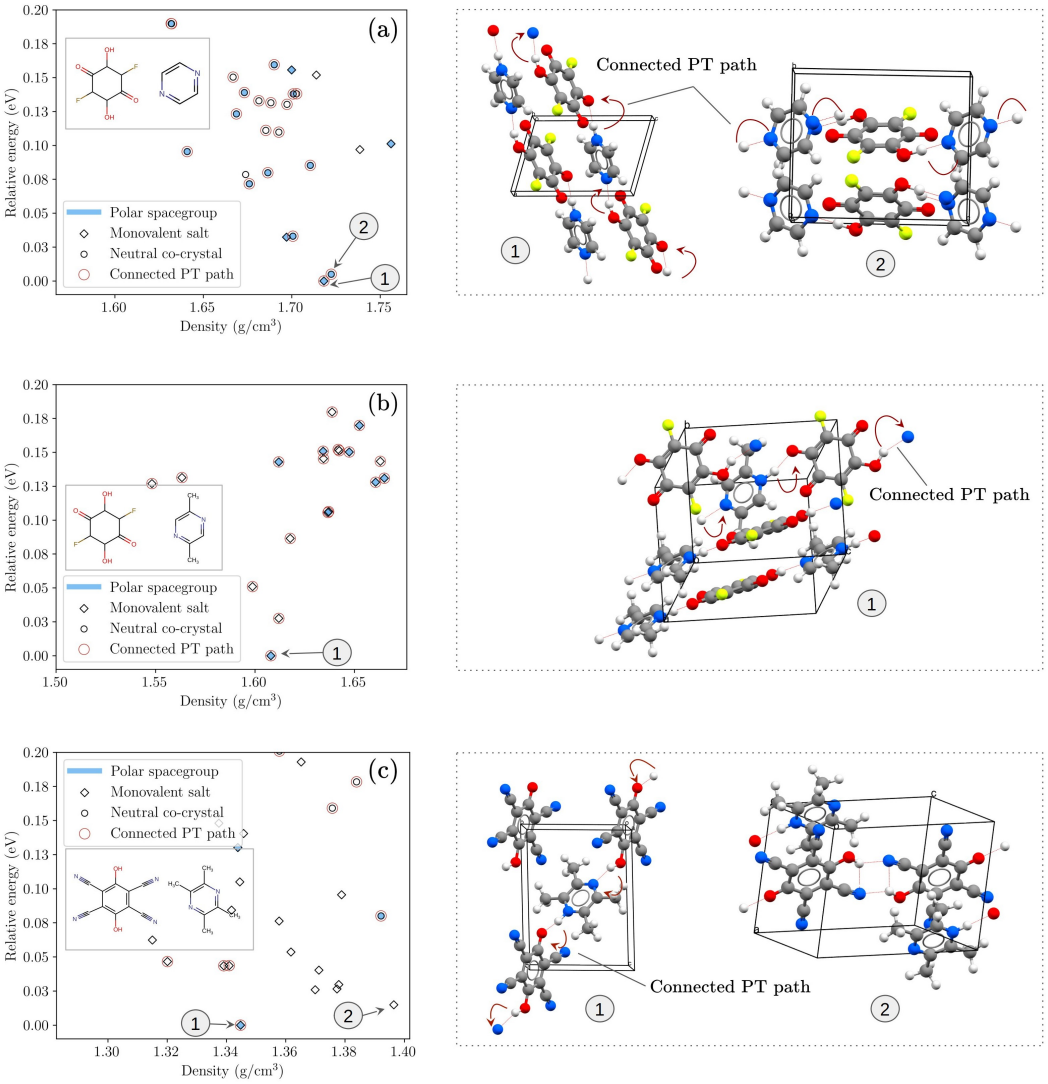


FIG. 7: The CSP landscapes for (a) DMAN-TMPZ and (b) DFAN-TMPZ molecular combinations are plotted using relaxed structures DFT energies.

ture exhibits an energy difference of approximately 0.01 eV, making it a potential competing polymorph. Therefore, experimental confirmation is necessary to determine whether the structure at the global minima is indeed a stable polymorph.

Panel (b) displays the landscape of DFAN-DMPZ where a structure with a ferroelectric packing is in the global minimum. The closest structure is a MS with a centrosymmetric space group $P2_1/c$ and connected PT path, which makes it a potential antiferroelectric crystal.

Finally, panel (c) displays the CSP landscape of TCHQ-TMPZ. In contrast to the DFAN-PZ, the low-energy region is predominantly occupied by MS structures. The global minimum features a ferroelectric packing with a polar space group and a connected PT path.

The second structure is an MS with no connected PT path. However, in comparison to TCHQ-PZ and TCHQ-DMPZ, TCHQ molecules form a homosynthon and do not engage in hydrogen bonding with TMPZ molecules. Similar to the DFAN-PZ, the energy difference between the global minimum and the second-ranked structure is approximately 0.01 eV. Due to the potential for polymorphism, experimental validation is recommended to confirm the stability of the ferroelectric packing structure.

For the ferroelectric systems, we have also computed the $\boldsymbol{P}_s$. The magnitudes are 14.9, 15.0, and 9.1 $\mu C/cm^2$ for DFAN-PZ, DFAN-DMPZ, and TCHQ-TMPZ respectively. These values are, on average, three times larger than reported $|\boldsymbol{P}_s|$ of acid-base OPTFes.

## IV. SUMMARY AND CONCLUSIONS

Using the CSP method, we assessed 30 combinations of different acid and base molecules to engineer new acid-base OPTFe salts with improved properties. In the initial stage, 17 molecular combinations were excluded due to the absence of a dynamically stable MS protonation state, which was examined in a template packing. Following CSP analysis utilizing single-point DFT and relaxed DFT energies, among the remaining combinations, four showed no anti/ferroelectric structure, two exhibited an antiferroelectric packing, and three displayed a ferroelectric packing. In the majority of the anti/ferroelectric landscape, the proximity of structures in the low-energy region suggests further experimental validation to confirm that the predicted structure is the stable crystal with the predicted properties.

From a design perspective, insights can be learned through the analysis of CSP landscapes. Firstly, the addition of more electronegative groups on acids and more electrodonating groups on bases results in an increased presence of MS structures within the low-energy range. However, increasing the acidity and basicity of the molecules can lead to a situation where DS structures tend to be more stable on the energy landscape. Secondly, most NC structures exhibit connected PT paths, and replacing different acid and base molecules does not change this synthon. Lastly, MS structures have more resistance in forming connected PT paths, and replacing methyl and dimethyl pyrazine increases the number of structures with connected PT paths in the low-energy region.

Through this approach, the study endeavors to pave the way for the rational design of organic ferroelectrics with enhanced properties, opening up new possibilities for technological applications and material advancements.

## ACKNOWLEDGMENTS

The computations of this work were carried out on UNINETT Sigma2 high-performance computing resources (grant NN9650K). This work is supported by the Research Council of Norway as a part of the Young Research Talent project FOX (302362).

[1] L. W. Martin and A. M. Rappe, Thin-film ferroelectric materials and their applications, Nat. Rev. Mater. **2**, 16078 (2016).

[2] S. Horiuchi, S. Ishibashi, K. Kobayashi, and R. Kumai, Coexistence of normal and inverse deuterium isotope effects in a phase-transition sequence of organic ferroelectrics, RSC Adv. **9**, 39662 (2019).

[3] S. Horiuchi, S. Ishibashi, and Y. Tokura, 3-hydrogen-bonded organic molecular ferroelectrics/antiferroelectrics, in *Organic Ferroelectric Materials and Applications*, Woodhead Publishing Series in Electronic and Optical Materials, edited by K. Asadi (Woodhead Publishing, 2022) pp. 47–84.

[4] G. R. Krishna, R. Devarapalli, G. Lal, and C. M. Reddy, Mechanically flexible organic crystals achieved by introducing weak interactions in structure: Supramolecular shape synthons, J. Am. Chem. Soc. **138**, 13561 (2016).

[5] S. Horiuchi et. al., Above-room-temperature ferroelectricity and antiferroelectricity in benzimidazoles, Nat. Commun. **3**, 1308 (2012).

[6] S. Horiuchi, K. Kobayashi, R. Kumai, and S. Ishibashi, Proton tautomerism for strong polarization switching, Nat. Commun. **8**, 14426 (2017).

[7] S. Horiuchi and Y. Tokura, Organic ferroelectrics, Nat. Mater. **7**, 357 (2008).

[8] M. Owczarek et. al., Flexible ferroelectric organic crystals, Nat. Commun. **7**, 13108 (2016).

[9] M. Tomura and Y. Yamashita, One-dimensional supramolecular tapes in the co-crystals of 2,5-dibromo-3,6-dihydroxy-1,4-benzoquinone (bromanilic acid) with heterocyclic compounds containing a pyrazine ring unit, CrystEngComm **2**, 92 (2000).

[10] K. Łuczyńska, K. Drużbicki, K. Lyczko, and W. Starosta, Complementary optical and neutron vibrational spectroscopy study of bromanilic acid: 2,3,5,6-tetramethylpyrazine (1:1) cocrystal, Vib. Spectrosc. **75**, 26 (2014).

[11] A. M. Reilly et. al., Report on the sixth blind test of organic crystal structure prediction methods, Acta Crystallographica Section B **72**, 439 (2016).

[12] D. H. Bowskill, I. J. Sugden, S. Konstantinopoulos, C. S. Adjiman, and C. C. Pantelides, Crystal structure prediction methods for organic molecules: State of the art, Annu. Rev. Chem. Biomol. Eng. **12**, 593 (2021).

[13] S. L. Price, Is zeroth order crystal structure prediction (csp0) coming to maturity? what should we aim for in an ideal crystal structure prediction code?, Faraday Discuss. **211**, 9 (2018).

[14] S. M. Woodley, G. M. Day, and R. Catlow, Structure prediction of crystals, surfaces and nanoparticles, Philos. Trans. R. Soc. A **378**, 20190600 (2020).

[15] G. M. Day, Crystal structure prediction, in *Supramolecular*

*Chemistry* (John Wiley Sons, Ltd, 2012).
[16] R. Kumai et. al., Structural assignment of polarization in hydrogen-bonded supramolecular ferroelectrics, J. Am. Chem. Soc. **129**, 12920 (2007).
[17] S. Horiuchi, R. Kumai, and Y. Tokura, A supramolecular ferroelectric realized by collective proton transfer, Angew. Chem. Int. Ed. **46**, 3497 (2007).
[18] S. Horiuchi, R. Kumai, and Y. Tokura, High-temperature and pressure-induced ferroelectricity in hydrogen-bonded supramolecular crystals of anilic acids and 2,3-di(2-pyridinyl)pyrazine, J. Am. Chem. Soc. **135**, 4492 (2013).
[19] D. H. Case, J. E. Campbell, P. J. Bygrave, and G. M. Day, Convergence properties of crystal structure prediction by quasi-random sampling, J. Chem. Theory Comput. **12**, 910 (2016).
[20] I. Sobol', On the distribution of points in a cube and the approximate evaluation of integrals, USSR Comput. Math. Math. Phys. **7**, 86 (1967).
[21] S. L. Price, M. Leslie, G. W. A. Welch, M. Habgood, L. S. Price, P. G. Karamertzanis, and G. M. Day, Modelling organic crystal structures using distributed multipole and polarizability-based model intermolecular potentials, Phys. Chem. Chem. Phys. **12**, 8478 (2010).
[22] D. S. Coombes, S. L. Price, D. J. Willock, and M. Leslie, Role of electrostatic interactions in determining the crystal structures of polar organic molecules. a distributed multipole study, J. Phys. Chem. **100**, 7352 (1996).
[23] A. Stone and M. Alderton, Distributed multipole analysis, Mol. Phys. **56**, 1047 (1985).
[24] Daniel G. A. Smith et al., PSI4 1.4: Open-source software for high-throughput quantum chemistry, J. Chem. Phys. **152**, 184108 (2020).
[25] S. Horiuchi, R. Kumai, and Y. Tokura, Hydrogen-bonding molecular chains for high-temperature ferroelectricity, Adv. Mater. **23**, 2098 (2011).
[26] S. Horiuchi et. al., Above-room-temperature ferroelectricity in a single-component molecular crystal, Nature **463**, 789 (2010).
[27] A. L. Spek, Single-crystal structure validation with the program $PLATON$, J. Appl. Crystallogr. **36**, 7 (2003).
[28] J. A. Chisholm and S. Motherwell, Compack: a program for identifying crystal structure similarity using distances, J. Appl. Crystallogr. **38**, 228 (2005).
[29] C. R. Groom, I. J. Bruno, M. P. Lightfoot, and S. C. Ward, The Cambridge Structural Database, Acta. Crystallogr. B. **72**, 171 (2016).
[30] F. H. Allen, The cambridge structural database: a quarter of a million crystal structures and rising, Acta. Crystallogr. B. **58**, 380 (2002).
[31] K. Berland, E. D. Sødahl, and S. Seyedraoufi, Molcrys, `https://gitlab.com/m7582/molcrys/` (2023), [Online; accessed 01-May-2023].
[32] S. L. Childs, G. P. Stahly, and A. Park, The saltcocrystal continuum: The influence of crystal structure on ionization state, Mol. Pharmaceutics **4**, 323 (2007), pMID: 17461597.
[33] G. Kresse and J. Hafner, Ab initio molecular dynamics for liquid metals, Phys. Rev. B **47**, 558 (1993).
[34] G. Kresse and J. Furthmüller, Efficiency of ab-initio total energy calculations for metals and semiconductors using a plane-wave basis set, Comput. Mater. Sci. **6**, 15 (1996).
[35] G. Kresse and J. Furthmüller, Efficient iterative schemes for ab initio total-energy calculations using a plane-wave basis set, Phys. Rev. B **54**, 11169 (1996).
[36] S. Seyedraoufi, E. D. Sødahl, C. H. Görbitz, and K. Berland, Database mining and first-principles assessment of organic proton-transfer ferroelectrics (2023), arXiv:2306.00363.
[37] R. D. King-Smith and D. Vanderbilt, Theory of polarization of crystalline solids, Phys. Rev. B **47**, 1651 (1993).
[38] R. Resta, Theory of the electric polarization in crystals, Ferroelectr. **136**, 51 (1992).
[39] R. Resta, Macroscopic polarization in crystalline dielectrics: the geometric phase approach, Rev. Mod. Phys. **66**, 899 (1994).
[40] S. Horiuchi, F. Ishii, R. Kumai, Y. Okimoto, H. Tachibana, N. Nagaosa, and Y. Tokura, Ferroelectricity near room temperature in co-crystals of nonpolar organic molecules, Nat. Mater. **4**, 163–166 (2005).

ISBN: 978-82-575-2130-1
ISSN: 1894-6402

Norwegian University
of Life Sciences

Postboks 5003
NO-1432 Ås, Norway
+47 67 23 00 00
www.nmbu.no

119458 / MEDIEHUSET-ANDVORD.NO